Investigation of laminar-specific neurovascular coupling features and pupillometry recording in a newly established awake fMRI model

Dissertation

zur Erlangung des Grades eines

Doktors der Naturwissenschaften

der Mathematisch-Naturwissenschaftlichen Fakultät

und

der Medizinischen Fakultät

der Eberhard-Karls-Universität Tübingen

vorgelegt

von

Hang Zeng

aus HuBei, China

2022

Tag der mündlichen Prüfung: 06/04/2022

Dekan der Math.-Nat. Fakultät: Prof. Dr. Thilo Stehle

Dekan der Medizinischen Fakultät: Prof. Dr. Bernd Pichler

1. Berichterstatter: Prof. Dr. Klaus Scheffler

2. Berichterstatter: Prof. Dr. Sandra Beer-Hammer

Prüfungskommission: Prof. Dr. Klaus Scheffler

Prof. Dr. Cornelius Schwarz

Prof. Dr. Sandra Beer-Hammer

Prof. Dr. Kristina Hefert

Erklärung / Declaration:

Ich erkläre, dass ich die zur Promotion eingereichte Arbeit mit dem Titel: "**Investigation of laminar-specific neurovascular coupling features and pupillometry recording in a newly established awake fMRI model**" selbständig verfasst, nur die angegebenen Quellen und Hilfsmittel benutzt und wörtlich oder inhaltlich übernommene Stellen als solche gekennzeichnet habe. Ich versichere an Eides statt, dass diese Angaben wahr sind und dass ich nichts verschwiegen habe. Mir ist bekannt, dass die falsche Abgabe einer Versicherung an Eides statt mit Freiheitsstrafe bis zu drei Jahren oder mit Geldstrafe bestraft wird.

I hereby declare that I have produced the work entitled "**Investigation of laminar-specific neurovascular coupling features and pupillometry recording in a newly established awake fMRI model**", submitted for the award of a doctorate, on my own (without external help), have used only the sources and aids indicated and have marked passages included from other works, whether verbatim or in content, as such. I swear upon oath that these statements are true and that I have not concealed anything. I am aware that making a false declaration under oath is punishable by a term of imprisonment of up to three years or by a fine.

Tübingen, den ....

Datum / Date Unterschrift /Signature

Contents

Abstract

The neuronal firing patterns across cortical layers have been extensively studied to better depict the information flow through neural network. Furthermore, the hemodynamic features have also been investigated by applying the line-scanning fMRI method on animal models. However, the underlying neural correlation to the laminar-specific fMRI signal has not been specified. Here, we established the multi-modal fMRI platform, i.e., concurrent fMRI and intracellular calcium recordings by implementing a multi-slice or bilateral slice line-scanning fMRI method with fiber-based calcium recording system on rodent models to explore the laminar-specific neurovascular coupling features across the cortical layers. Our results demonstrate the calcium leading earlier events than BOLD signals along the cortical layers under evoked and resting-state conditions. In addition, the bilateral BOLD and calcium signals showed diverse coupling features under different stimulation paradigms. These methods allow us to assess the intrinsic spatiotemporal correlation features of neural responses with the laminar-specific fMRI signals in vivo, providing the feasibility of deciphering the altered patterns of fMRI signal across different cortical layers.

Awake rodent fMRI is becoming a promising noninvasive brain imaging modules in recently years, especially combined with behavior or cognition related tasks. However, the fully ‘awake’ brain state remains challenging to interpret, as different restraint protocols and pre-interval anesthesia were, at least in some studies, applied preceding scanning. Furthermore, the motion artifacts and stress level of the awake animals highly dependent on the restraint system and anesthetic agents. Here, in the current project, we successfully established an awake mouse fMRI with pupillary measurement undergoing an intermittent restraint system without any anesthetics. Under visual stimulus, BOLD responses were found in visual-circuit related (visual cortex, dorsal lateral geniculate nuclei, superior colliculus) brain regions. Furthermore, the real-time pupil recordings provide us the stress and motion levels of animals, which severed as a good indicator for our data quality. Thus, this awake mouse fMRI platform provides the possibility for functional longitude imaging and underpins a higher power for ongoing and future translational studies in fully conscious brains.

Abbreviations

ASL – Arterial spin labeling

AFNI – Analysis of Functional NeruoImage

ANS – Autonomic nervous system

AD – Alzheimer's disease

BOLD – Blood oxygen level dependent

CC – Corpus callosum

CBF – Cerebral blood flow

CBV – Cerebral blood volume

$CMRO_2$ – Cerebral metabolic rate of oxygen

EEG – Electroencephalography

EPI – Echo planar imaging

FP-S1– forepaw somatosensory cortex

fMRI – Functional magnetic resonance imaging

FOV – Field of view

GLM – Generalized linear model

GE – gradient echo

LGd – Dorsal lateral geniculate nucleus

LFP – Local field potential

MRI – Magnetic resonance imaging

MEG– Magneto-encephalography

NMR – Nuclear magnetic resonance

NIRS – Near infrared spectroscopy

PET – Positron emission tomography

PD – Pupil data

RF – Radio frequency

SPECT Single photon emission computed tomography

SE – spin echo

SC – Superior colliculus

VASO – Vascular space occupancy

VC – Visual cortex

Investigation of laminar-specific neurovascular coupling features and pupillometry recording in a newly established awake fMRI model

1. Introduction

With years of development, functional neuroimaging is becoming an emerging tool for neuroscientists as well as for researchers for visualizing brain functions in health or diseased brain states [1]. Nowadays, a wealth of neurological techniques mapping brain functions such as functional magnetic resonance imaging (fMRI)[2, 3], positron emission tomography (PET)[4], single photon emission computed tomography (SPECT)[5] and near infrared spectroscopy (NIRS)[6], etc., have been widely used for clinical or basic research purposes. However, some of these methods have limitations. For instance, the PET/SPECT needs injection of radiopharmaceuticals for measurements, which is radiative to the living tissues. The NIRS suffers from its low spatial resolution (also depth of brain that can be imaged)[7]. Furthermore, the temporal resolution of those methods are still not enough to directly reflect the dynamic neural fluctuations [7]. Therefore, some other non-imaging techniques, such as magneto-encephalography (MEG)[8], electroencephalography (EEG)[9], which directly reflect the neuronal activities have been combined or implemented with those neuroimaging techniques to outmost the imaging performance that a single methodology can offer. Notably, the EEG/MEG has millisecond temporal resolution, which can effectively detect the neural responses. However, the EEG studies normally involve in inserting microelectrodes directly into the brain, which is invasiveness and mostly restricted to animal models. The extracranial EEG and MEG experiments are non-invasive, but it is hard to specify the causal effects of a given pattern of activity acquired from the surface of the skull. Therefore, multi-modal imaging systems are emerging as a trend for probing brain functions in the field in the last decade [10, 11].

The thesis contains two chapters, of which the chapter I involves in applying the multi-modal fMRI imaging system to investigate the laminar-specific neurovascular coupling events across the cortical layers in rat forepaw somatosensory cortex (FP-S1) under anesthetized brain state. In chapter II, a newly awake mouse fMRI with pupil recording platform was established and brain functional connectivity was explored under visual stimulations. Thus, in the following first the structure of the cerebral cortex, second

magnetic resonance imaging techniques with the focus on blood oxygen level-dependent (BOLD) signals, laminar specific fMRI and calcium recording, and third the awake mouse model will be introduced.

1.1 Structure of the cerebral cortex.

The cerebral cortex normally contains distinct layers and their functions, structures and morphological types varied across species as well as brain regions (Fig.1&2) [12-14]. For example, previous reports investigated the laminar compositions in visual cortex, showing thalamo-cortical, cortico-cortical input connections (Fig.3) [15-17]. Notably, layer 1-3 and layer 5-6 mainly receive feedback from cortico-cortical and thalamo-cortical projections [18]. While, layer 4 receives feed-forward and thalamo-cortical projections [19]. Electrophysiology studies have also reported the first synaptic activity in layer 4 and then spread to the layer 2/3 and layer 5 [20]. This further supports the layer 4, particularly in somatosensory cortex, is the main laminae that initials the neuronal activity in the cortex and may underlie the information flow as well as surrounding neural interactions horizontally or vertically in the cortex [21]. Despite our deep understanding of the cellular structures in the cerebral cortex, the full map of neurons still needs to be elucidated.

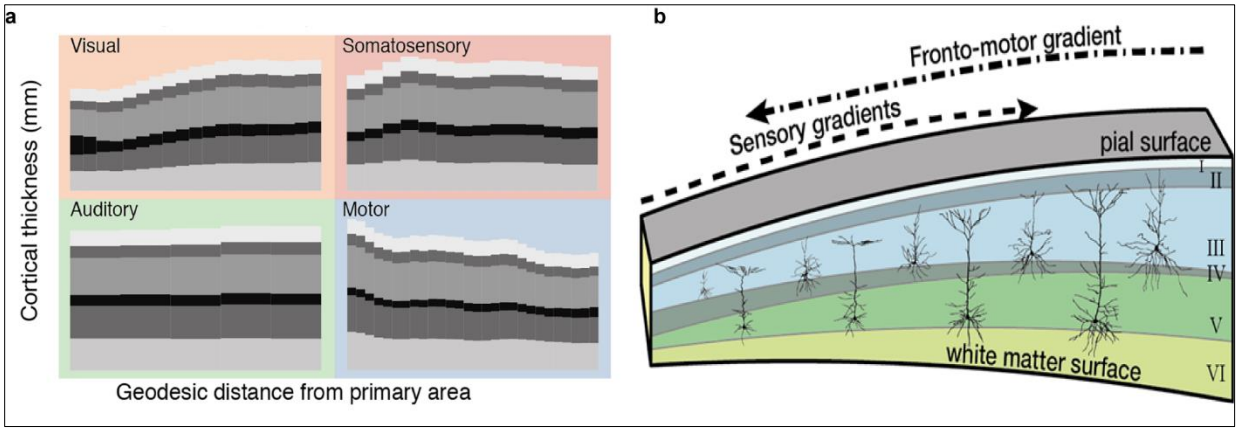

Fig.1.Cortical structures from different cortical regions. (a) Layer thicknesses averaged across vertices in a sliding window of geodesic distance values from the primary area for the visual, somatosensory, auditory, and motor systems. (b) Single-cell morphological studies of pyramidal neurons in macaque sensory processing pathways. (Modified from Wagstyl, K., *et al.* (2020)[14]).

With years of anterogradely and retrogradely technical development, it has been demonstrated that layer 2-3 mainly consists supragranular neurons and layer 5-6 contains infragranular neurons with intermixed pyramidal neurons [22, 23]. Therefore, the connectivity across the layers is multi-interconnected, e.g., the supragranular neurons project cortically and infragranular neurons project subcortically and cortically [24]. In addition, the neurons distributed within the different layers have different functions, i.e., excitation and inhibition. The layer 1 is dominated by the inhibitory neurons and the layer 2-6 are largely excitatory neurons [24]. Therefore, the microcircuits and functions within the different layers distinct with each other (Fig.2&3).

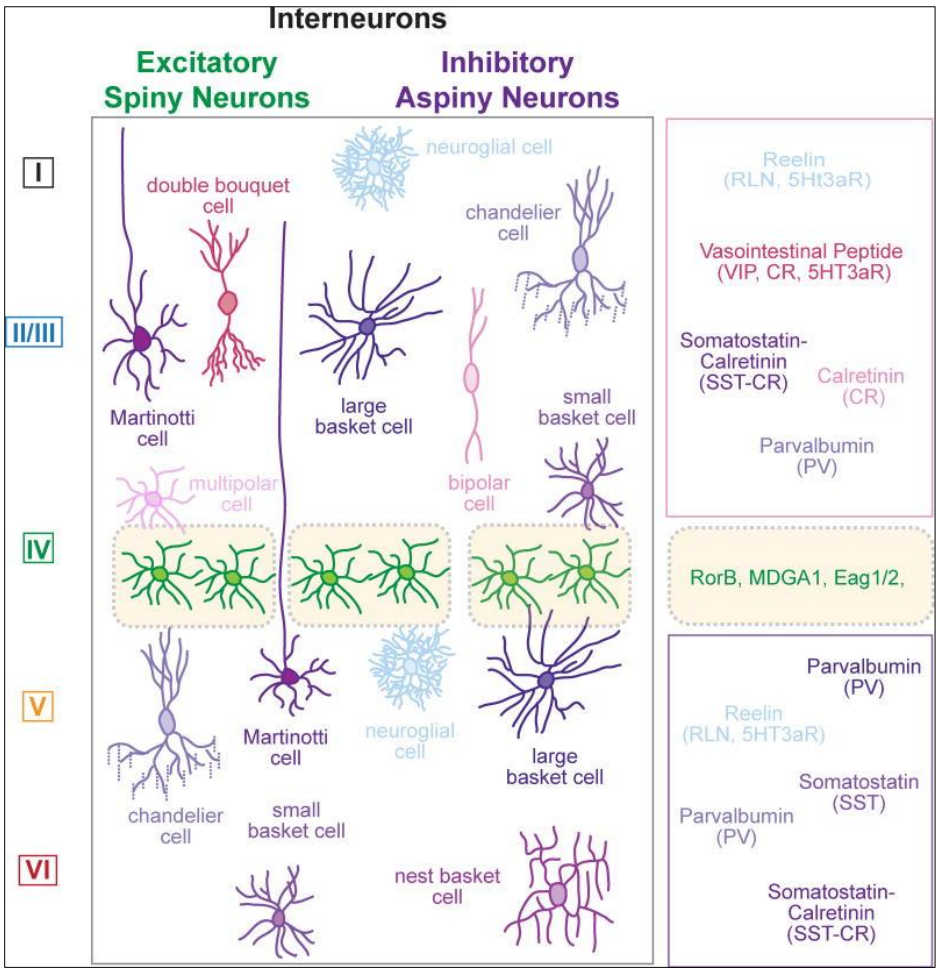

Fig.2. Neocortical excitatory and inhibitory interneurons distributed along the cortical layers. (Cited from Lodato, S., *et al.* (2015)[25]).

Furthermore, the vascular structures and distributions across different layers affect blood oxygen level-dependent (BOLD) responses. Depending on the spatial resolutions and imaging sequences, the hemodynamics can be dominated by the surrounding neural activities that were driven by the mirco-vessels [26]. In addition, the vascular size (micro or macro) and orientation can also affect the BOLD signals. It has been reported that the vascular structures in the cortex can be classified into two group, i.e., the micro-vessels (~5μm) and macro-vessels (>10μm) [27]. Furthermore, the macro-vessels were divided according to their penetration depths across the cortical depth, i.e., layer 1-2 (arteries: 10~25μm, veins: 20~30μm), layer 3-5 (arteries: 15~30μm, veins: ~45m), layer 6 (arteries: 30~40μm, veins: ~65μm), and white matter (arteries: 30~74μm, veins: 80~125μm) [27, 28]. In addition, the cortical surface consists of many pial vessels (>100μm), which collect and supply blood to the cortical layers. The vessel diameter varies accordingly with their penetrations depth along the cortical layer. Besides, the architecture of vascular system is not a randomly oriented, instead a cluster of surface vessels (parallel) and penetrating vessels (perpendicular) in the cortex surface [29-31]. In addition, the cortical orientation to the main magnetic field has significant effects on BOLD signals while imaging, particularly, in the current line-scanning fMRI methods [32, 33]. Therefore, the BOLD responses were normally stronger in the surface and decreased toward the deep layers in laminar fMRI (Fig.4) [33-36].

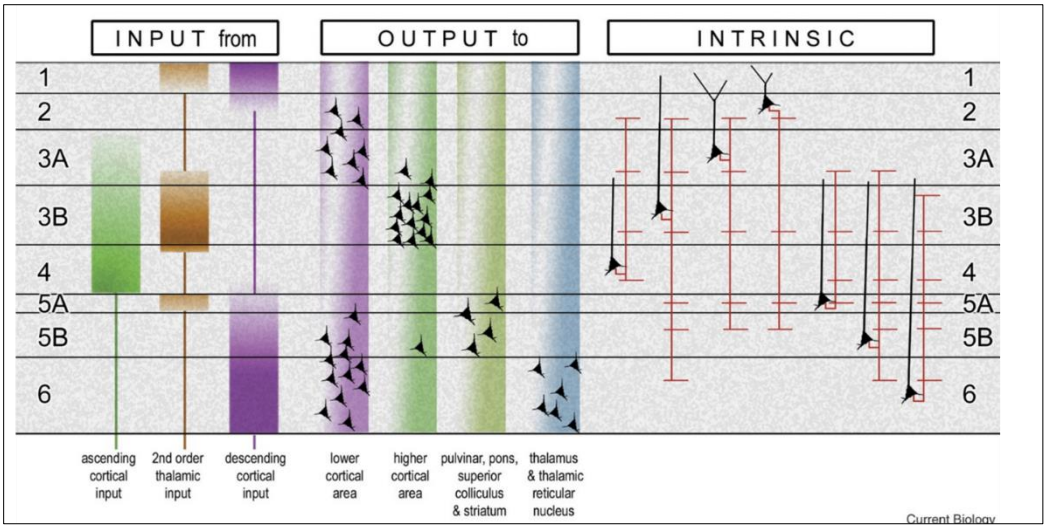

Fig.3. Summary of inputs, outputs and intrinsic excitatory connections of a generic, nonprimary visual area of primate cerebral cortex. (Cited from Shipp, S. (2007)[37]).

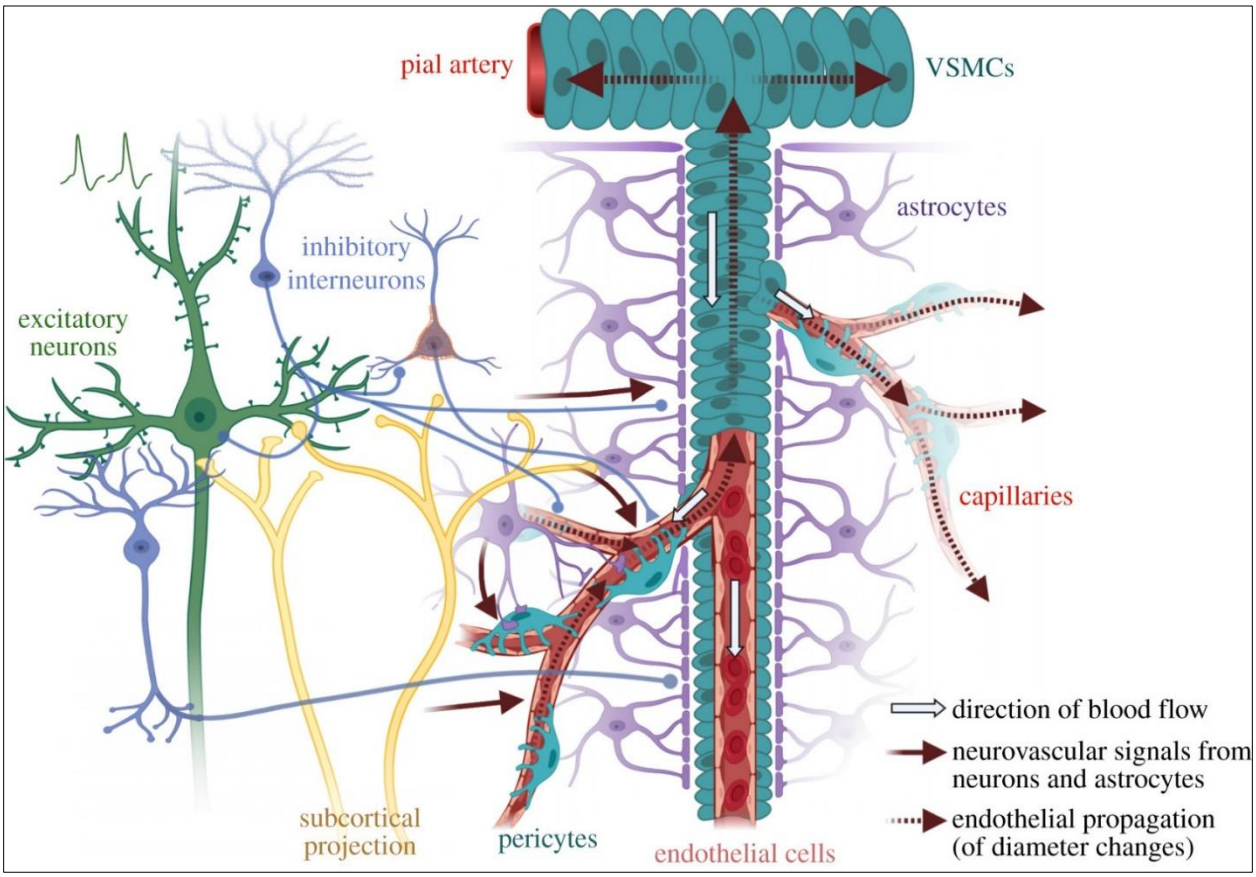

Fig.4. Neurovascular couplings involved in vascular, cellular and cytoarchitecture. (Cited from Howarth, C., *et al.* (2021)[36]).

1.2 Magnetic Resonance Imaging (MRI)

Compared with the above neurophysiological methods, fMRI is non-invasive and has a relatively high spatial resolution. Over the past 30 years, fMRI has becoming a major neuro-methodology in exploring brain functions for human subjects, particularly, in the field of cognitive neuroscience [1, 7]. In addition, the fMRI technique has served as a promising tool in translational and basic research studies, as lots of researchers and groups have integrated this technique on animal models across species, e.g., non-human primate[38], rodents[16, 39], pigeons [40], cats[41], dogs[42], rabbits[43], etc. Because of these advantages, investigators can facilitate the optogenetics, local field potentials (LFP), two-photon or optical fiber recordings with the fMRI simultaneously on animal models. Furthermore, the animals can be repeatedly imaged in fMRI experiments as needed.

Thus, multi-modal fMRI imaging modalities, i.e. combined with other neuroimaging or non-imaging techniques, have allowed us a further step in exploring the brain circuit [44], sensory-driven processes [45, 46], cognition [47, 48], etc., in both normal and pathological brain states.

The magnetic resonance imaging (MRI) dates back as earlier as 1924, when Wolfgang Pauli proposed that the atomic nuclei possesses spin and magnetic moment properties[49]. In addition, he suggested that the atomic nuclei could only spin at certain frequencies under some particular magnetic fields. Later, in 1933, the American physicist Isidor Rabi, based on Pauli's ideal, measured the quantum spins of hydrogen nuclei by changing the strength of the static magnetic field and matched the spin frequency of the atomic nucleus with the frequency of the oscillating magnetic field, which made the nucleus absorb the energy from the field[50]. Afterwards, in 1945-1946, Purcell and Bloch's lab, respectively, measured the resonance effects of the water by applying the transmitter coil, which sent electromagnetic energy into the sample and the receiver coil, which was used to measure changes in the energy emitted back by the sample[51, 52]. Their work laid the foundation for nuclear magnetic resonance (NMR), which forms the basis of all modern MR imaging techniques. Furthermore, the basic design principles of Bloch's simple apparatus shape the nowadays' MR scanner designs, i.e., a strong static magnetic field, a transmitter coil that sends electromagnetic energy to the sample, and a receiver coil that measures energy emitted back from the sample. Until 1972, Paul Lauterbur realized the great potential and value of applying the NMR techniques to biological and physical applications. Thereby, he acquired the first MR images from water sample by introducing four spatial gradients in the magnetic field, which altered the protons' resonant frequencies at different field locations[53]. By measuring how much energy was emitted at different frequencies, he could identify how many protons were presented at each spatial location. This was the first time that the spatial information was introduced in the MR imaging. Later, in 1976, Peter Mansfield, developed the echo-planar imaging (EPI), which sends one electromagnetic pulse from a transmitter coil, introducing rapidly changes of magnetic field gradients while recording the MR signal[54]. This approach underlies the most prevalent and important MR imaging technique even in today's applications. Currently, it has become clear to us that the EPI is particularly important for fMRI studies in exploring

the brain functions, as fast sampling rates are needed to measure hemodynamic changes in the brains. Interestingly, due to the negative impression of the word nuclear, the word MRI came out in earlier 1980s as a consequence of terminological change from the NMR. In 1985, the FDA approved MRI scanners for clinical use[55] and ever since, MRI scans have emerged as a worldwide conventional medical service in any hospital or healthcare centers. Nowadays, any medical professionals can easily access it, which really boosts its current clinical medicine development.

Now we know the basic components of MRI consist of strong static magnetic field to reorient atomic nuclei, the gradient magnetic fields to introduce spatial variation, and the oscillating radiofrequency fields to induce changes in energy states of the nuclei. The today's MRI mainly focuses on hydrogen nuclei[56], because the human body contains large quantity of water, which consist of single proton. In the presence of a strong static magnetic field, the protons show a tendency to align parallel or antiparallel to the main field[57]. Protons in the parallel state have a lower energy level, while protons in the antiparallel state have a higher energy level[57]. The MR signals were not directly measured by the behavior of those single protons, instead a sum of the net magnetization of all spins in a given volume, which was determined by the balance between the parallel and antiparallel states, i.e., the number of protons in low energy and high energy level. In addition, by sending radio frequency (RF) pulses (electromagnetic energy) into the tissue through the transmitter coils, the low energy level protons were excited to a higher energy state, which disturb its original balance of the net magnetization. Subsequently, when the RF pulses were removed, the excited protons will emit the absorbed electromagnetic energy that can be detected by a receiver coil. Measurement of this emitted energy can provide us the detailed information of those protons that form our images.

As the excited spins in the high-energy level (antiparallel) go back to their original low-energy level (parallel). This phenomenon is known as longitudinal relaxation, i.e., the net magnetization recovers to its initial balance. The time constant associated with this longitudinal relaxation process is called T1[58]. While, after an excitation pulse tips the net magnetization into the transverse plane (perpendicular to the magnetic field), all of the spins in the sample precessing coherently in the same phase with all the other

surrounding protons. Over time, the coherence between the spins is gradually lost and they become out of phase, i.e., the separation of neighboring spins from each other. This phenomenon is known as transverse relaxation[58]. Intrinsically, this is mainly caused by the spin-spin interactions, i.e., the spins interact with each other's magnetic fields and disrupt each other's spin rates. The time constant associated with this intrinsic transverse relaxation is called T2[58]. These random interactions differ in quality from one tissue to another depending on how freely mobile the water protons are, e.g., multiple sclerosis plaques in the brain have longer T2 than surrounding tissue [59]. While, the external surroundings can also affect the transverse relaxation time, which for instance, extrinsically, the inhomogeneity of the external fields can alter different frequencies at different spatial locations of the proton's precession. This phenomenon is called T2* decay, which is much faster than T2 in terms of the dephase coherence and transverse magnetization loss[60]. One typical example is that a blood vessel nearby will have some iron in deoxyhemoglobin and this will uniformly affect spins nearby causing more rapid loss of phase coherence and therefore signal loss [61]. This T2* decay is particular important in the Blood oxygen level-dependent (BOLD) contrast for fMRI.

1.3 Blood oxygen level-dependent (BOLD) contrast

The transverse relaxation time is very important in the field for investigating the neural activity. As mentioned above, the T2 mainly depends on the spin-spin interactions intrinsically. However, extrinsically, the T2* transverse relaxation time can be influenced by the external environment, most likely due to the inhomogeneity of the magnetic field. In both human and animal models, the brain tissues consist tons of neurons, blood vessels and fibers that vary region-to-region, which may lead to the inhomogeneity in different brain regions. Particularly, this inhomogeneity highly depends on the state of the brain as well as the local circulation of the blood supply. Notably, the brain physiological states reflect the local neural activity, which lay the foundation for measuring the T2* changes, thus indirectly assembling the neural activities. Physiologically, the activated neurons in the brain consume much more energy, i.e., oxygen and glucose, than that in resting-state. In addition, the activated neurons signal the dilation of local blood vessels, increasing blood flow as well as blood volume to supply the energy demand in the active

brain regions. This process can be simply termed as neurovascular coupling, i.e., the interactions between the local neuronal activities and the surrounding vascular dynamics[62]. The chapter I in this thesis will mainly discuss about the neurovascular coupling events between the calcium and blood oxygen level-dependent signals along the cortical layers in the rat cortex.

Since 1990s, Seiji Ogawa, a Japanese professor firstly introduced the blood oxygen level-dependent (BOLD) signals, which was recorded from rat brains [63]. Later, it turned out that the BOLD effects heavily rely on the relative concentration between the hemoglobin and deoxyhemoglobin in the blood. It's known that blood cells carry O_2 and energy to cells, particularly the vast majority of neurons in the brain tissues, which thus indirectly reflect the energy consumption and tissue metabolism that is related to the neuronal activation or deactivation [3]. Upon neural activations, the hemoglobin in blood loses oxygen and becomes deoxyhemoglobin, which changed the magnetic properties, i.e., the paramagnetic deoxyhemoglobin alters magnetic susceptibility of blood [64, 65]. This changes made the T2* different between blood vessels and the surrounding tissue. By tracking the local changes of the T2*, we can index the neuronal activations. Thereafter, extensive research has been conducted to probe the BOLD signals in human brains in both resting-state and evoked conditions, which enables to label the functional connectivity across multiple brain regions [3, 66-68]. BOLD fMRI has now become a conventional and established technique in helping researchers and physicians to dissect the relationships between the brain's neural and hemodynamic functions comprehensively. For example, the diagnose of Parkinson disease [69], Alzheimer's disease (AD)[70, 71] and many other brain disorders. Furthermore, for non-clinical applications, researchers even go deep further to map the macroscopic or microscopic events in the brain matrix induced by a complex series of manipulations, e.g., sensory stimulations[72], memory loading [73-75] and cognition tasks[75] in both human and animal models. With the rapid development of fMRI in the field of neuroscience, it became clear that the BOLD signals are a consequence of a series of indirect effects. Directly resulted from changes in the magnetic properties of water molecules, which in turn reflect the influence of paramagnetic deoxyhemoglobin from the surrounding blood cells. The increment of deoxyhemoglobin in the blood vessels related with oxygen consumption, which itself is a correlate of a change in neuronal activity

evoked under different imaging paradigms, e.g., sensory, motor, and/or cognitive processes. The underlying mechanisms in this chain are that the transverse relaxation time (T2*) are finally changed in the activated regions, which disrupt the initial field homogeneity between the local and surrounding tissues. In addition, this process inducing BOLD contrast also lead to some other physiological changes, such as cerebral blood flow (CBF) [76-78], cerebral blood volume (CBV) [78, 79] and cerebral metabolic rate of oxygen ($CMRO_2$) [80-82], all of which can in turn modulate the neuronal behaviors. Therefore, the BOLD signal is a complex and indirect surrogate underlying neural activity. Though indirect and complexity, researchers have been interested in exploring the mechanisms or relationships of BOLD response during neural activations. Not surprisingly, with years of investigation, extensive studies have made clear that the BOLD time-series normally behave ~2s onset lag time after stimulus and reach to its peak 6~8s and return to its baseline thereafter in both human and animal models [67, 77, 83, 84]. This temporal behavior is caused by the increase of deoxyhemoglobin upon neural activation, which in turn increases the CBF that supply oxygenated blood [85, 86]. The neurons have a much faster temporal dynamics than the hemodynamics upon stimulations. More recently, much progress have been made to see more detailed temporal characteristics of BOLD time series, e.g., time-to-peak after sensory stimulations [81], post-stimulus undershoot [87] and latency of onset time [88].

As briefly discussed forehand, the fMRI is becoming more and more closely related to our daily life. In addition, it has drawn a broad interest of researchers to combine various neurological techniques to study the brain functions, e.g., two-photon imaging [89], local field potentials (LFP) [10], fiber-based cellular recording system [11], optogenetics [90] and behavior [47, 48]. All these techniques can provide a better understanding of brain functions, but not completely of the whole brain computations. Investigators, nowadays, can more precisely interpret the BOLD signals with the help of those above neuro-methodologies. However, the underlying causal relationships between neural activity and BOLD signals remains largely to be explored. Furthermore, many MRI sequences, which related to the interpretation of BOLD signals, have been developed for different imaging purposes. For instance, spin echo (SE) EPI or gradient echo (GRE) EPI for BOLD detection[87], the arterial spin labeling (ASL) for CBF[91], vascular space occupancy (VASO) for CBV[92], and

calibrated fMRI for $CMRO_2$[93]. For almost 30 years of learning the BOLD fMRI, there are still some limitations and caveats, e.g., the experimental design (small sample size)[94], data acquisition (pulse sequence) and analysis[95], head motions[1], etc. Therefore, there is no 'perfect' BOLD-fMRI study, instead systematically considerations of the possible factors that confound fMRI results should be taken into account before the MRI scans.

1.4 Laminar-specific fMRI

Both the human and animals' cerebral cortex has been studied for years. Histological experiments have made it clear that the cortex consists of six different layers, in which the layers hold different functions [33, 96]. The laminar fMRI has been the major method to investigate the laminae circuit-based pathways, i.e., feedforward or feedback information flows. Notably, with the development of advanced fMRI techniques in recent years, scientists are trying to probe the BOLD fMRI at a sub-millimeter or column level. Furthermore, various computational data analytical approaches and tools have emerged, which greatly boost our understanding of the laminar-specific information flow across the cortical depth through hemodynamic inference [21]. Several groups have investigated the spatial and temporal characteristics of the laminae by applying the BOLD-fMRI [33, 97], CBV [35] or CBF [98]. However, it remains challenging to specify the neuronal circuit's networks that are involved in the widespread functional connectivity within different brain regions, particularly, the regions that are physically distinct from each other. In addition, the fMRI signals indirectly characterize the neuronal activation by capturing the hemodynamic fluctuations are a mixture of BOLD and non-BOLD signals. These non-BOLD signals may come from physiological artifacts, i.e. head motions, heartbeat or respiration [99]. Upon neuronal activation, the laminae hemodynamics imitated in the capillary bed toward cortical surface and subsequently downstream towards local capillary beds and venous networks [21, 100, 101]. This may lead to the distinct temporal behaviors across layers that, in turn, affect its propagations to other parts of the brain. Besides, the blood flows from cortical surface to the deep layers and the laminae vessel diameters vary across the layers [102], making the BOLD signal amplitudes larger in the surface and weaker in the deep layers[33, 35]. These phenomena have been commonly observed in many fMRI experiments[33, 97, 103], including the current projects, i.e., with our high spatiotemporal line-

scanning fMRI data acquired from the rat FP-S1, we have found the cortical superficial and middle layers possess much stronger BOLD responses than that in deep layers upon electrical sensory stimulations. Notably, these variations were not merely caused by the neuronal activations within the layers, instead, the vasculature organizations were also involved. Thus, an interpretation of neuronal activities across the different laminar structures solely based on the fMRI is not precise. Therefore, researchers have implemented optical-fiber based calcium imaging [11], two-photon imaging [89] and local filed potentials (LFPs) [10] recording into fMRI studies to better decipher the causal relationships between neuronal activations and hemodynamics.

Among the various laminar fMRI methods, line-scanning fMRI holds very high temporal and spatial resolution for BOLD signal detection, e.g., sub-millimeter resolution (50um) and a faster sampling (50ms) at a smaller field of view (FOV) [33, 103]. This approach, as its name dubbed, only focus on a single slice that covers the region of interest (ROI) and completely skips the phase-encoding steps, which further shortens the acquisition time. Furthermore, the saturation pluses are applied to suppress the signals outside ROI, which allow a single line from the slice to be excited and acquired after every excitation. In the current projects, the phase-encoding gradient was turned off and the frequency-encoding gradient was set perpendicular to the cortical depth, which provided us detailed information (a line) across each layers in the rat FP-S1.

1.5 Calcium recording

The calcium signal is a relatively direct and activity-dependent fluorescence that can track the fast neural dynamics in *vivo* (Fig.5) [11, 104, 105]. As mentioned above, BOLD contrast is an indirect estimator for brain activity, which is also related with the changes in CBV, CBF and $CMRO_2$. Therefore, seeking possible mechanisms that may provide direct interactions between BOLD responses and neural signals can help us to better interpret fMRI results. With the emerging of optical imaging techniques, scientists have successfully implemented the MRI compatible optical fibers (optogenetics) to stimulate the brain [39, 90]. Based on this method, Schulz et al. further improved this method and extended to record the calcium fluorescent from neurons [11]. Briefly, the genetically encoded protein sensors, i.e., calcium sensors (GCaMP6) or synthetic calcium dyes (for

example, Oregon Green Bapta-1AM, OGB1-AM) were expressed or loaded in the ROIs and single-photon excitation through an optical fiber were applied to target those ROIs by delivering the excitation light form a laser [104]. Upon stimulation, neural activations caused fast changes of intracellular calcium, which can be chelated by the calcium dyes or indicator proteins. Depending on the types of calcium indicators, the chelators emit specific fluorescent that can be easily detected by a photomultiplier. In the current projects, we have built an optical fiber-based recording system for calcium signals detection. Therefore, we can acquire the BOLD and calcium signals simultaneously in the block-designed fMRI experiments.

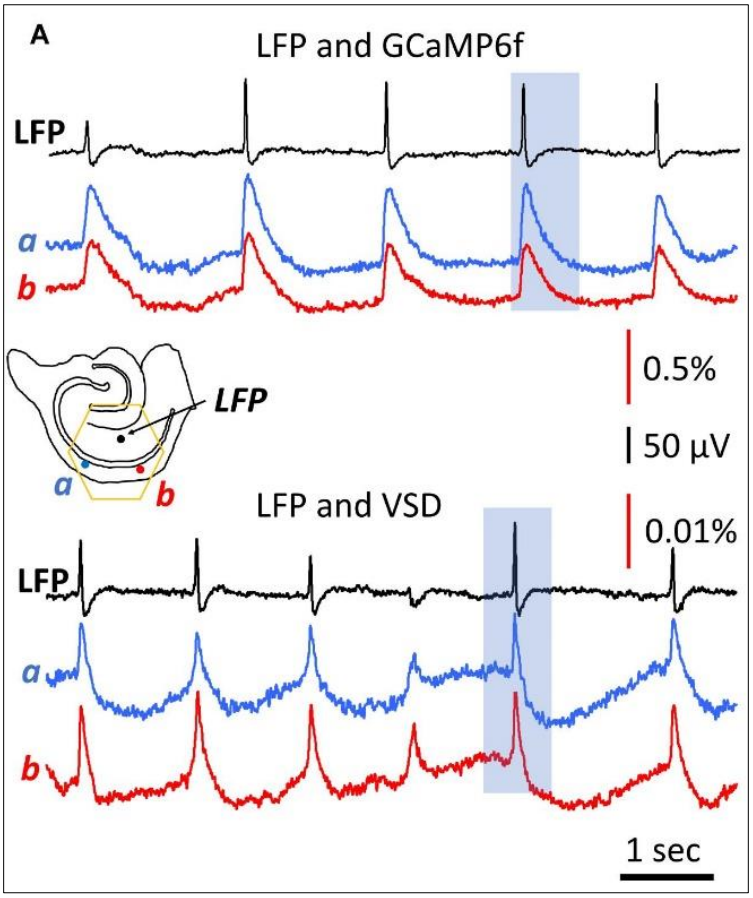

Fig.5. LFP and GCaMP6f/VSD (Voltage-Sensitive Dye imaging) recordings from the same tissue. (Cited from Li, P., *et al.* (2019)[105]).

1.6 Awake mouse fMRI model

Awake animal fMRI studies dated back as early as in late 1990s, couple of years after Ogawa et al., discovered BOLD for indexing the brain functions [3, 106]. Particularly, the rodent fMRI hold a great promise than other species, i.e., not only its small body size that can fit the limited magnetic bore, but also availability in various disease or transgenic models nowadays. Therefore, the functional connectivity can be fully investigated under normal or pathophysiological brain states. In addition, the animal models can be applied to develop new biomarkers, pharmacological therapies or surgical techniques. Furthermore, with the emerging advanced neurological methods, e.g., the electrophysiology[10], optical imaging[11] and optogenetic brain stimulation[90], etc., which have been implemented in the fMRI, providing us a multi-modal imaging system to explore the brain function at multiple dimensions. Those invasive techniques normally cannot directly apply to humans, instead benefit us for the basic brain research on animal models that can in turn facilitate the possible treatments or underlying patho-mechanisms. Therefore, a lot of groups and investigators have gradually focused their research topics on awake animal fMRI projects. We choose mouse as the animal model in the current studies, not only because of it relatively small body size that can fit our apparatus, but also can be easily trained to be familiar with our imaging system. Furthermore, some groups have applied the transgenic mouse model to investigate the possible pathological mechanisms or abnormal behaviors in disease models, which offers possible treatments for the preclinical applications (Table.S1).

In earlier days, the vast majority of animal fMRI studies have applied anesthesia to reduce the motion artifacts and stress in the animals [106, 107]. However, it was clear that the anesthetic effects posed confounding modulations on brain states [107]. Particularly, under resting-state conditions, the functional connectivity that is involved in various neural networks can be disturbed by the different anesthetics [108, 109]. Furthermore, some anesthesia can preserve the functional connectivity, while others may not or even suppress the connectivity [109]. This made it more difficult to interpret the underlying neural fluctuations and to distinguish the possible effects or treatments for circuit-based connectivity, particularly on patho-brain states. Jaakko et al., has compared and

investigated the most common six anesthesia protocols on awake rats, demonstrating that the different anesthetic agents have unique modulations on brain functional connectivity [110]. For instance, medetomidine can suppress the global brain activity, while propofol as well as urethane showed less suppression under resting-state. For investigating the different individual functional connections, the six anesthesia protocols also showed distinct modulation effects. Therefore, in the current awake model, we tried to avoid using any anesthetic agents. This, in turn, posed several challenges to our work, e.g., the animal stress, the motions artifacts and training procedures, etc. Though challenging, it was believed that the awake animal fMRI model holds great promise, as many researches are only possible in the conscious state, e.g. cognitive processing, behavioral studies and decision-making, etc.

The stress level of the animals in awake fMRI has been one of the most commonly discussed questions in the field. The awake animal fMRI studies, unlike human fMRI, need various measurements to monitor the stress level from animals while being exposed in the scanner. As we all know, the imaging system in the magnetic field always produces lots of acoustic noise. The higher the magnetic field, the louder the noise from the scanner. Therefore, being exposed in such a higher decibel of noise and confined in a limited space, the subjects were always stressful. In awake fMRI, the acoustic noise is a key challenge in imaging paradigms, which can pose lots of pressure to the animals. Many previous studies have designed a step-wise training acclimation procedure to train the animals to be familiar with the imaging environment. Some other groups even designed earplugs to avoid the louder noise. However, those restraint devices may also introduce extra stress to the animals. Therefore, in the current awake project, we tried to avoid applying too many restrain apparats, except the head post, to fix the animals in restraint training system.

The motion artifacts are the other most common concerns in awake animal fMRI, since the animals were imaged under full consciousness. This is the reason why it is necessary to head-fix the animals in the scanner. We have designed plastic head post for fixation of the mouse in the training advice. Some investigators even designed some kind of ‘jacket’ for the animals (Table.S1). However, this is not as efficient as using the head post,

especially when the animals were involved in task-related or behavior-based imaging modules. Notably, the head post can also add severe artifacts to the images, especially the tiny air bubbles or bloody spots beneath head post. In addition, to attach the head post/bar on top of the skull, some groups even used the micro-skews to fasten the head post (Table.S1). Compared to the previous awake animal fMRI studies, in the current awake model, only the 3D-printed head post were used for immobilize the animals, avoiding extra surgical manipulations to the skull. Therefore, there were less image distortions, which were induced by the skews.

1.7 Aim of the studies

It remains an open question regarding to what extent the neuronal and vascular activities interact with each other as well as how their interactions contribute to the laminar neurovascular coupling patterns along the cortical depth. Therefore, in the first part of chapter I, we further improved our established multi-modal fMRI platform with concurrent fMRI and intracellular calcium recordings by implementing a multi-slice line-scanning fMRI method with fiber-based calcium recording. Thereby, allowing us to investigate the neurovascular coupling features across the cortical depth by placing three slices consecutively (rostral to caudal) to cover the forepaw somatosensory cortex in one hemisphere on rat brain. This work provides a unique laminar-specific neurovascular coupling feature along the cortical depth within multiple sites in such a short patch region, which may help to characterize the normal and pathological brain states in future studies.

In the second part of chapter I, the questions whether any laminar neurovascular coupling events across the two hemispheres and were the coupling features along cortical layers arise were clarified. Based on the first project, we subsequently performed similar experiments on rat brains, different from the first part that focusing on a short patch of region from one hemisphere, we further placed bilateral slices on FP-S1 regions in left and right hemisphere to investigate the BOLD propagations from one hemisphere to the other side upon stimulations. Simultaneously, calcium signals were also recorded at one hemisphere, which were induced by direct stimulus or contralateral propagations, possibly through corpus callosum (CC). With this bilateral laminar-specific fMRI imaging

modality, it provides us a better deep understanding of the interhemispheric laminar-specific neurovascular coupling events across the two hemispheres.

In chapter II, the aim was to build a newly awake mouse fMRI model with pupillometry recoding. Trying to answer the questions: Can it be possible to image the awake animals (completely free of anesthesia) in ultrahigh filed? Does the real-time pupil fluctuations index stress relief and motion controls in awake animals? This awake mouse fMRI model will allow us to combine behavioral, cognitive-based task or memory loading, etc., in future research and to examine potential dysregulation of brain states, particularly, in transgenic mouse models of human disease in on-going and future projects.

2. Chapter I: Investigation of laminar-specific neurovascular coupling features

2.1 Part 1: Concurrent intracellular calcium recordings with laminar fMRI mapping

2.1.1 Introduction

The cortical layers or laminae constitute a myriad of structural and functional units, signaling a highly value for communicating the feedforward, horizontal and feedback information flow across different brain regions[111, 112]. Layer-dependent functional magnetic resonance imaging (fMRI) allows examination of information flow, as the afferent and efferent connections terminate in different cortical layers. For this reason, it has drawn great interest of neuroscientists to probe how those messages interact through the separate layers as well as to elucidate the neurovascular coupling features. Recent developments in laminar fMRI pave new avenues for distinguishing the laminar and columnar circuitry at different layers in a sub- or supra-millimeter level[21, 33, 35, 111, 113]. However, the limited spatial resolution and low signal-to-noise (SNR) as well as contrast-to-noise (CNR) remains challenging, especially in human fMRI studies[114]. Thereby, the animal laminar fMRI studies have emerged as prefect modalities for achieving unparalleled visualization of vasculature hemodynamics to neuronal processing along the cortical depth. For instance, the different onset time of neural inputs along the cortical layers[33, 97], the top-down and bottom-up interactions between the laminae and distant brain areas[113, 115] and the layer specific non-BOLD (blood oxygen level dependent) fMRI signals[116-118], etc.

With the advancement of ultra-high magnetic field and cutting-edge imaging techniques, researchers have dissociated layer depth-dependent signal changes with ever increasingly fine- higher spatiotemporal resolutions[33, 35, 97]. However, the conventional fMRI measures the neuronal responses indirectly via changes of cerebral blood flow (CBF)[119], cerebral blood volume (CBV)[113] or cerebral metabolic rate of oxygen ($CMRO_2$)[120], which consist a combination of hemodynamic and (non-)neuronal signals. Thus, making it complicated to discriminate the dominate signal sources across the cortical layers for neuroscientific applications. Furthermore, the laminae has different anatomical structures, vascular architectures and neuropils that vary across the cortex, which lead to their distinct functions and connectivity across species. Despite the

complexity of the laminar metric, the neural activity and BOLD signal changes are putatively related[121-124]. To account for those challenges, researchers have implanted various imaging techniques, i.e. spin/gradient-echo (GE/SE) BOLD fMRI and contrast agent MRI, which are vessel-sensitive or vessel-size dependent to pinpoint the interference from the aforementioned confounding effects[113, 115, 116, 118]. Measures of spatiotemporal characteristics of cortical hemodynamic response with laminar fMRI has been applied on both humans and rodents[33, 35]. The laminar connectivity demarcating the cellular metabolism and vascular hemodynamics reflects the neurovascular coupling events from the different cortical layers[24, 34]. It remains an open question regarding to what extent the neuronal and vascular activities interact with each other as well as how their interactions contribute to the laminar neurovascular coupling patterns along the cortical depth.

Here we propose the hypothesis that the neuronal activities drive the hemodynamic changes, showing distinct neurovascular coupling features that can be detected by laminar fMRI. For this purpose, we developed a multi-modal line-scanning fMRI that allows for simultaneously recording neuronal and BOLD signals under different stimulus paradigms in rodents. To rule out the relationships between the cellular and vascular oscillations along the cortical depth, we measured the evoked and spontaneous intracellular calcium fluorescence using the genetically encoded or virally mediated calcium indicator (GCaMP6f) in the rat somatosensory cortex. The GCaMP6f has been widely used as a biomarker of neural activity[125]. In parallel, BOLD signal from multiple sites of the rat brain were acquired through our multi-slice line-scanning fMRI method. The results indicate that calcium signals are strongly correlated with the BOLD along the cortical depth and play a leading role for the hemodynamic fluctuations. Of note, we also found the laminar spatiotemporal coupling features varied and inhomogeneous even within such a short patch of region, showing an altered laminar fluctuation pattern. Thereby, our analysis provides a glimpse into opportunities of the cellular origins that underpins cortical mechanisms of the BOLD signals through the newly developed multi-modal molecular fMRI approach.

2.1.2 Materials and Methods

Animals

All experimental procedures were approved by the state authority (Regierungspräsidium, Tübingen, BadenWürttemberg, Germany) and conducted in accordance with the guidelines. Fifteen male Sprague-Dawley rats (3 week-old) were employed in the project and four of them were excluded for further data analyses due to the brain damage or weak response of BOLD. The animals were habituated individually/group at a 12hr-12hr light-dark cycle with food and water *ad libitum*.

Surgery

All procedures were described in a previous study[72]. Rats were initially anesthetized with isoflurane (5% induction, 1.5% maintenance). Each rat was orally intubated and placed on a mechanical ventilator (SAR-830/AP, CWE). Plastic catheters were inserted into the right femoral artery and vein to allow monitoring of arterial blood gasses and administration of anesthetics. After surgery, each rat was given an intravenous bolus of α-chloralose (60 mg/kg) and isoflurane was discontinued. Anesthesia was maintained with α-chloralose (26.5 mg/kg/hr) in combination with pancuronium bromide (4 mg/kg/hr) to reduce motion artifacts. The rats' rectal temperature was maintained at around 37°C. To prevent head motion, rats were secured in a head holder with a bite bar. All relevant physiological parameters (end-tidal CO_2, rectal temperature, heart rate, and arterial blood pressure) were continuously monitored during imaging. The pulse sequence-based trigger and stimulation control were established using the BIOPAC system (Goleta, USA) and Master-9 A.M.P.I system (Jerusalem, Israel).

Viral vector injection and optical fiber implantation

The viral vectors (AV-1-PV2822 AAV5.Syn.GCaMP6f.WPRE.SV40) expressing GCaMP in neurons were purchased from University of Pennsylvania Vector Core. Viral vectors were injected in the forepaw region of the primary somatosensory cortex (S1FL) of 3-4 week-old rats. For the stereotactic injection procedure, rats were initially anesthetized with isoflurane. After exposing the skull, a small bur hole was drilled on top of the S1FL. The nanoliter injector (WPI, FL) was used to place a 35-gauge needle at the proper

coordinates in the stereotactic frame. Injections were performed slowly over 5-6 mins and the needle was slowly removed after being kept in the injection site for 10 min after finishing the injection. The injection sites of S1FL were as follows: AP= 0.2 mm, ML= 3.7 mm, 400 nL for each injection at 1.2 mm and 0.7 mm depth. After 6-8 weeks of viral expression, an optical fiber (FT200EMT: NA = 0.39, Ø200 μm; Thorlabs) was carefully implanted for detecting the calcium florescence in S1FL (AP = 0.2 mm; ML = 4.0 mm; DV = 1.0~1.3 mm; angle=10°-20°). The optical fiber was fixed on the skull with glue. Then, the skin was sutured to cover the glue with the optical fiber (9m length) extending outside of the rat head.

MRI experiments

Under α-chloralose anesthesia, all MRI were carried out on a 14.1T horizontal bore magnet (Magnex) interfaced to an Avance III console (Bruker). A transceiver surface coil (Ø 6mm) was positioned over the S1FL to acquire images. Electrodes were placed into the left forepaw to deliver trains of 300μs electrical pulses (2.5mA, 3Hz, 4s) in each epoch. To locate the BOLD-fMRI signals, 3D echo planar imaging (EPI) sequence was applied with the following parameters: 1.5s TR, 14ms TE, 19.2×19.2×8.0mm FOV, 64×64×16 Matrix, 0.3×0.3×0.5mm^3 resolution, 130 TRs in total. Anatomical images were quickly acquired by using the fast low angle shot (FLASH) sequence with the same geometry displacement as that in EPI. Once the geometry position for BOLD activations was located in the S1FL, the line scanning multiple slices were placed to cover the most activated regions. The laminar fMRI data were acquired using the following parameters: 100ms TR, 10ms TE, 6.4×3.2mm FOV, 128×32 Matrix, temporal (100ms) and spatial (50μm) resolution, 200 repetitions, total scan time=640s, slice thickness 1.2mm, inter distance between slices 1.5mm. Two saturation slices were applied to suppress the signals outside ROI and the phase-encoding gradient was turned off. The cortical space between two saturation slices was 1.2mm.

Simultaneous fMRI with calcium recording

The light path system for the calcium signal recording was built up based on our previous study[45] (Fig.1b). A 488nm laser (OBIS 488LS, Coherent Inc., USA.) was applied as the excitation light source. The beams passed through a continuously variable metallic ND

filter (NDC-50C-4M-A, Thorlabs) and were reflected by a reflection mirror to the dichroic mirrors (F48-487, reflection 471-491nm, >94%; transmission 500-1200 nm, >93%; AHF Analysentechnik), and focused through a tube lens (AC254-030-A1-ML; Thorlabs) into a multimode optical fiber. Laser intensity was measured at the fiber tip (~5μW for neuronal calcium recording) by an optical power meter (PM20A, Thorlabs). The emitted fluorescent signal was guided back through the same fiber. Firstly, passing the dichroic mirror and optical filter (F37-516; 500-550nm band pass, AHF Analysentechnik), and then focused by the tube lens (AC254-030-A1-ML, Thorlabs) to directly project to a silicon photomultiplier (MiniSM 10035, SensL, Germany). Finally, the signal was amplified by voltage amplifier (DHPVA-100, Femto, Germany) before detected by the analogue input module of BIOPAC system (Goleta, USA) at a sampling rate of 5000Hz.

Data processing and statistical analysis

3D-EPI BOLD fMRI processing

To locate and confirm BOLD responses under stimulation in FP-S1 region, the 3D-EPI fMRI data were analyzed using AFNI software (NIH; https://afni.nimh.nih.gov/). Detailed descriptions of signal procedures can be found in our previous published paper[126]. The hemodynamic response function (HRF) model was used to generate BOLD fMRI map: BLOCK (d, p), which convolved (linear program 3dDeconvolve in AFNI) with a square wave of duration d and made a peak amplitude of p (the amplitude of basis function and usually set to 1). The HRF model is defined as follows:

$$HRF(t) = int(g(t-s), s = 0..\min(t, d))$$

Where g (t) =$g(t) = t^q e^{-t}/[q^q e^{-q}]$, q = 4, d is the square wave of duration.

Line-scanning BOLD fMRI processing

Line scanning BOLD fMRI line profiles were extracted from the raw FID files by applying our custom-written Matlab codes. BOLD signal intensity was plotted along the cortical depth as a function of time (50μm resolution along the 2mm cortical depth, 640s for each trail). We define the half maximum signal magnitude intensity as the cortical surface for

each trail[33]. The BOLD line-scanning fMRI percentage change map was made by averaging the line profile time-series from each epoch (1s-pre-4s-on-15s-off, 32 epochs/trail) and converted to percentage changes by subtracting and dividing each time-series by the average of 10 TRs (1s-pre) prior to stimulus. The formula for calculating the line-scanning BOLD signal percentage change:

$$\mathrm{Signal(i)} = \frac{\mathrm{S(i)} - \mathrm{S(base)}}{\mathrm{S(base)}}$$

Signal(i) is the signal percentage change, i = 0: TR: 20s, S(i) is signal intensity, and S(base) is the averaged pre-stimulation signal intensity from 0 to1s.

Ca^{2+} signal processing

The calcium time series were first segmented to match the fMRI data length and demeaned within each trial for further analysis by our custom-written Matlab codes. For evoked conditions, the calcium relative percentage change of fluorescence ($\Delta F/F$) was calculated, where ΔF is the 'noise-corrected' signal ($F-F_0$) and F_0 is the background signal intensity (0-1s, pre-stimulation). The calcium transient fluorescence signal in response to each single stimulus pulse (12 pulses, 3Hz, 4s) was calculated as the difference in $\Delta F/F$ in a time window of 300ms and 30ms pre-baseline, where the pre-baseline is the background signal before onset of each individual stimulus pulse. The calcium power spectrum density (PSD) was calculated by applying the *pwelch* function in Matlab (2500 Discrete Fourier transform points; 1s window length; 50% overlap) [127]. The calcium spectrogram and signal decomposition (power spectral profile:1-5Hz) were extracted by using the *timefreq* function[128] (https://sccn.ucsd.edu/eeglab/index.html).

Correlation analysis between fMRI and Ca^{2+}

For evoked conditions, the BOLD line profile time series were firstly detrend and normalized for all the trails acquired from each animal. Then, the normalized signals were band-pass filtered to 0.01-0.1Hz in MATLAB by using *butter* and *filtfilt* functions. The calcium signals were also band-pass filtered (0.01-0.1Hz) and subsequently down-sampled to match the fMRI temporal resolutions (100ms) in using the Matlab function *downsample*. Finally, the pre-processed fMRI and calcium signals were z-scored to

perform the correlations (*corr* function in Matlab) along the cortical depth for each slice. The distributions of correlation coefficient was plotted based on the correlation patterns within the three slices. For resting-state trails, the fMRI line profiles and calcium signals were firstly demeaned and filtered (0.01-0.1Hz). Then, the filtered signals were z-scored for correlation analysis. The subsequent processing were similar to those mentioned above in evoked conditions.

Cross-correlation analysis between fMRI and Ca^{2+}

To investigate the spatiotemporal features between fMRI and calcium. Cross-correlation analysis were performed for each individual trail in both evoked and resting-state conditions. As has been mentioned above, the mean calcium power spectral profile (e.g. 1-5 Hz) and voxel-wise fMRI time series (40 voxel) were extracted and cross-correlated in MATLAB using the *xcorr* function with a maximum of 100-150 data points. The cross-correlation coefficient were averaged along the cortical depth (40 voxels) and plotted together to produce the cross-correlations maps (Fig.4a). Based on these cross-correlation patterns, the lag times between the calcium and fMRI signals were extracted at the maximum of cross-coefficient. To further specify the laminar spatiotemporal features between Ca^{2+} and BOLD signals along the cortical depth, the color-coded cross-correlation maps were also produced by plotting each individual voxel-Ca^{2+} cross-correlation coefficient along the cortical depth (Fig.4c-d). One-way ANAON (post-hoc: Bonferroni correction) was applied to distinguish the cross-correlation lag time within the three slices.

Immunofluoresencent staining of the brain slices

To confirm the GCaMP expression in S1FL region after 3-4 weeks of virus injection, we firstly euthanized and perfused rats in pilot studies. Then, the brain tissues were carefully removed and fixated in 4% paraformaldehyde (PFA). To avoid cell damage, the fixated brain tissues were exposed in a 30% sucrose hypertonic solution for later cryostat sectioning. Finally, the immunofluoresencent staining experiments were conducted to localize the GCaMP expression. The detailed experimental procedures can be found in our previous published papers[126, 129].

2.1.3 Results

Concurrent multi-slice line-scanning fMRI mapping and Ca^{2+} recordings

We successfully established the fiber-optic based calcium recordings with fMRI mapping at multi-site of brain in our ultra-high magnetic field (Fig.1 & Fig.S1). The Ca^{2+} fluorescent is a good indicator for measuring neocortical activities, which can be specifically expressed in the rat S1FL regions (Fig.1a). Furthermore, the fiber photometry recordings can be combined simultaneously with fMRI for probing functional connectivity at targeted brain regions (Fig.1b & Video.S1). We carefully positioned the fiber tip into the S1FL region (Layer 2-4, ~1.0mm) to capture the fluorescence changes upon electrical forepaw stimulation. Concurrently, fMRI mapping with three slices were placed around to measure the neighboring BOLD response (Fig.1c). To better elicit the laminar hemodynamics, the rat head was usually positioned 20°-30° to the left, which makes the cortical layers orthogonal to the B_0 field (Fig.1c). The line-scanning fMRI method was specially developed to explore the laminar connectivity at ultrafast and high spatial resolutions along the cortical columns, which only needs the frequency-encoding gradient to align the 6.4mm line from the cortical surface to the subcortical regions[33]. Therefore, when repetitively acquiring the line profiles as a function of time in the block-design paradigm, we can plot all lines together to investigate the BOLD dynamics along the cortical depth (Fig.1d). These results support that our newly developed multi-slice line-scanning fMRI mapping and Ca^{2+} recordings are capable of indexing the regional hemodynamics and neuronal activities in S1FL under different conditions, respectively.

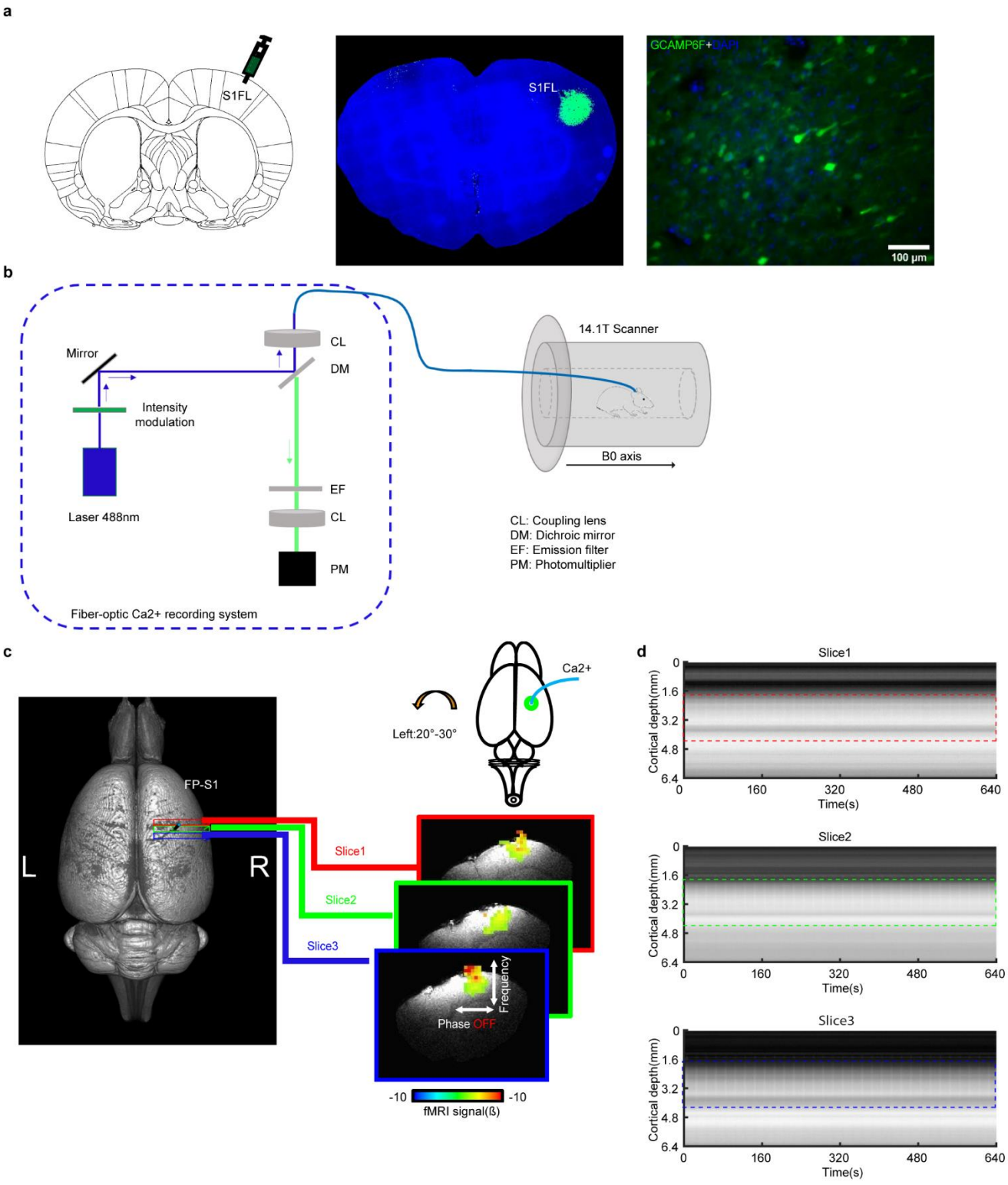

Fig.1.Setup for simultaneous fiber-optic calcium recording and multi-slice line-scanning fMRI. (a) Schematic of virus injection in S1FL (left); immunostaining images showing calcium expression in S1FL (middle); enlarged immunostaining image of co-localized calcium in neurons (green) and DAPI (blue). (b) Schematic drawing of the concurrent optical fiber-based calcium recording system and fMRI imaging. (c)

Anatomical displacement of the multiple slices line-scanning fMRI and calcium recording in S1FL (left), representative BOLD fMRI maps (p<0.001) within the three slices overlaid on FP-S1 (right). (d) BOLD line profiles plotted as a functional of time from the three slices, one animal, n=27 trails, the dash rectangular boxes denote the 2-mm cortical depth.

Laminar correlations between BOLD and Ca^{2+} in evoked conditions

To decipher the laminar neurovascular coupling features between BOLD and Ca^{2+} *in vivo*, we performed the block-design fMRI experiments with trains of brief electrical pulses to the rat forepaw. The Ca^{2+} and BOLD responses were robust and showed similar trend in response to the electrical stimulations in every imaging epoch (Fig.2a). The Ca^{2+} relative percentage change of fluorescence ($\Delta F/F$) showed a maximum of ~60% changes, which is consistent with previously published reports[45, 126, 130, 131]. The three slices showed a slightly different BOLD response with a maximum of ~0.6%, ~1.0% and ~1.5% signal intensity changes, respectively (Fig.2b). The Ca^{2+} spikes and transients were also extracted from the time series, showing solid neuronal activities in response to the electrical pulses (Fig.2b-2c top row). The Ca^{2+} transients showed an onset time of 31.9±10.0ms and rise time of 19.6±1.2ms (Fig.S2). The laminar BOLD features displayed distinct patterns within the three slices, showing stronger activities in Layer 2-4 in the third slice (Fig.2c).

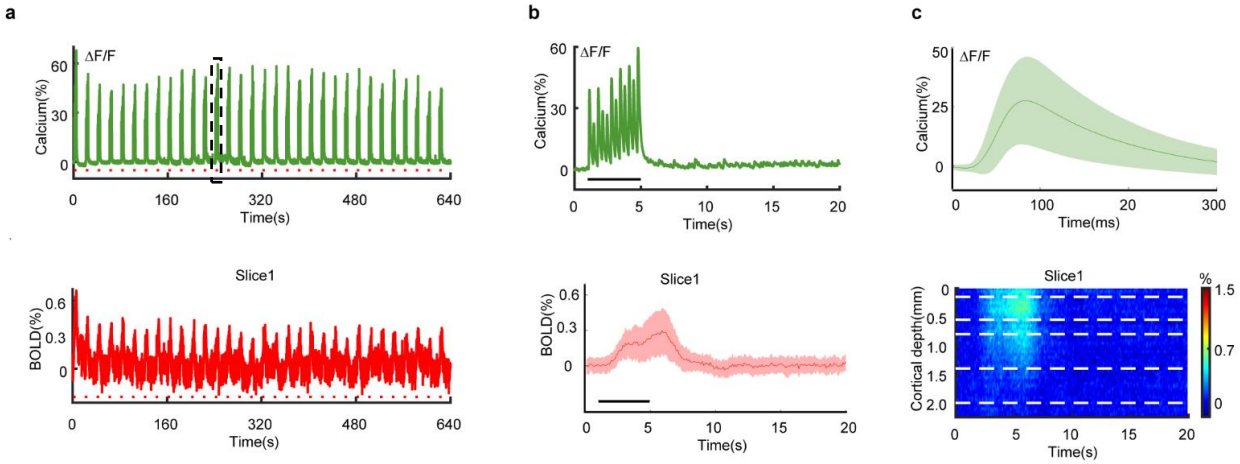

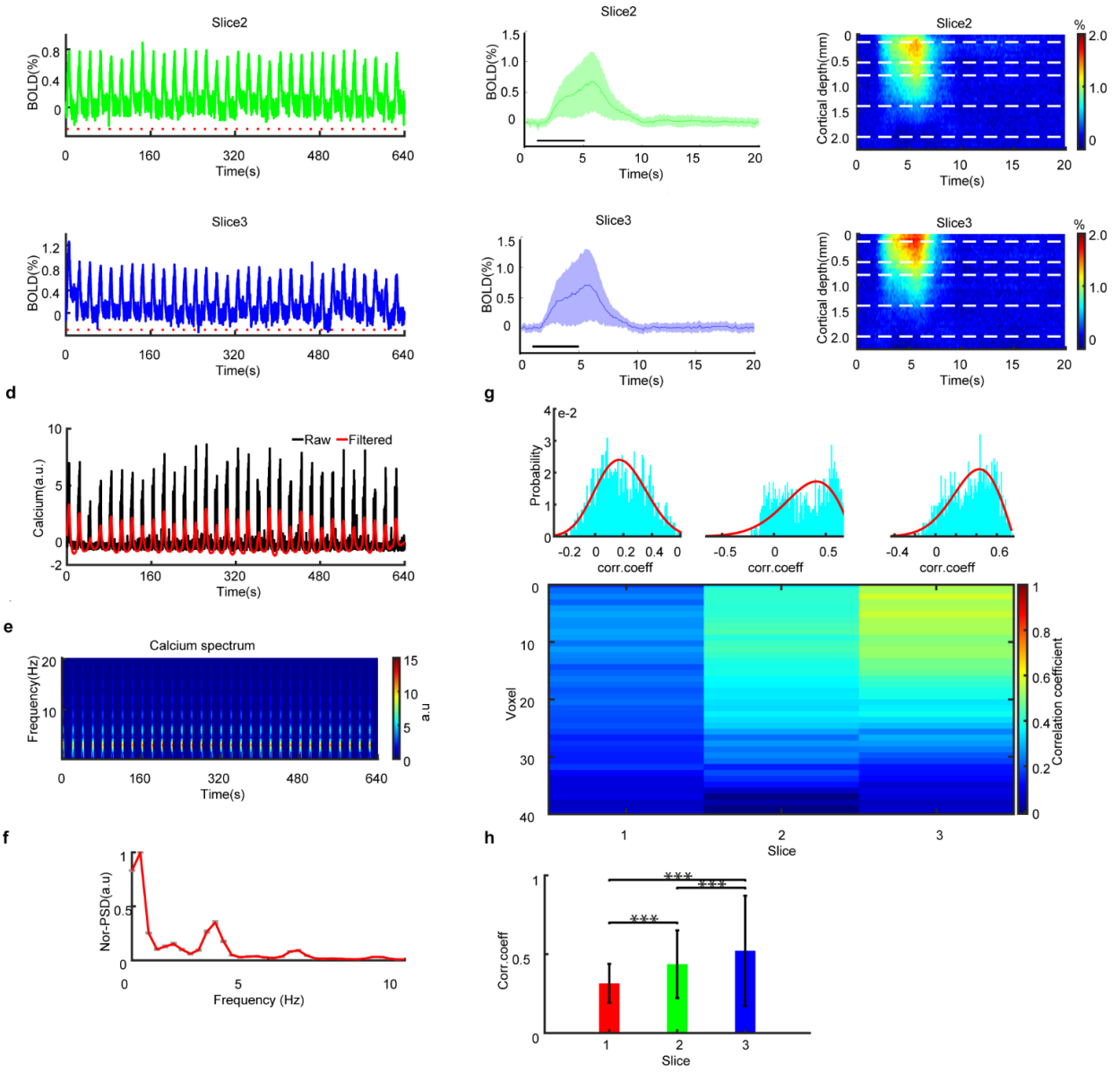

Fig.2. Simultaneous recorded calcium and fMRI signals within the three slices under forepaw stimulation. (a) The averaged time course of calcium (upper row) and BOLD signal percentage changes from one representative rat (n=27 trails), ΔF/F is the fluorescence change normalized by mean fluorescence, and horizontal red dot is the stimulation time (3Hz, 4s). (b) Upper: enlarged figure of calcium signals from left black dash line box, lower: mean epoch time course of BOLD signal percentage changes from three slices (20s/epoch, 4s-on-15s-off block design, shaded region: mean±S.D, black horizontal bar, 4s stimulation). (c) The averaged evoked calcium traces (upper row) in response to a single electrical pulse stimulus (1920 traces, shaded region: mean±S.D), lower: 2D maps (epoch-wise) of average BOLD fMRI signals along the cortical depth within the three slices (864 epochs), white dash lines indicating cortical layer1-6 along the 2mm depth. (d) A representative evoked raw and band-pass filtered calcium signal. (e) The average spectrogram of the evoked calcium from one representative rat (n=27 trails). (f) Mean calcium power spectrum density (mean±S.E.M, n=11 rats, and n=191 trails). (g) Correlation patterns between calcium and BOLD fMRI from the three slices along the cortical depth (n=27 trails), top row: distribution of the correlation coefficient from the corresponding slices, bottom row: averaged 2D correlation map between

the calcium and BOLD signals. (h) Statistical estimation of the correlation patterns within the three slices (mean±S.D, one-way ANOVA, Bonferroni post-hoc test, F (2, 494) =44.96, ***P=1.15e-18, n=11 rats).

Next, the filtered Ca^{2+} time series were paired with the BOLD line profiles (within each individual trail) along the cortical depth from the corresponding three slices, depicting stronger correlation patterns in the superficial layers in the third slices than in the other two slices (Fig.2c). In addition, the distribution of the correlation coefficients within the three slices were plotted, eliciting non-Gaussian distribution features in the second and third slices in contrast to the first slice (Fig.2g, top row). Statistical analysis revealed significant correlation patterns among the three slices (Fig.2h, correlation coefficient: 0.32±0.12, 0.44±0.21 and 0.52±0.35 for slice1-3 respectively, mean±S.D, ***P<0.001, n=11 rats). We conclude that our multi-modal imaging of Ca^{2+} and fMRI system provides the evidence of distinct laminar coupling features between neurons and surrounding hemodynamics in the S1FL under evoked conditions.

Laminar correlations between BOLD and spontaneous Ca^{2+} in resting-state

The spontaneous Ca^{2+} fluctuations and BOLD fMRI from the three slices were also acquired under resting-state. Fig.3a-3b showed raw and filtered fMRI time series along the cortical depth. Fig.3c revealed the spectrum information of the fMRI oscillations within the three slices, showing a dominate frequency of 0.01-0.1Hz signals that had been reported in previous studies[68, 132]. Similarly, correlation analysis was also performed to explore the laminar coupling features between Ca^{2+} and fMRI fluctuations. The filtered Ca^{2+} (Fig.3d) and corresponding BOLD time series from the three slices were correlated along the cortical depth, showing a much more varied and spare correlation patterns (Fig.3g). Furthermore, the correlation coefficient were much lower than the evoked conditions. Statistical estimations of the correlation coefficient for the trails from all animals showed no difference within the three slices (Fig.3h). We, therefore based on those results, summarize that the laminar neuronal oscillations and neighboring hemodynamics showed a much more diversely correlation features under resting-state.

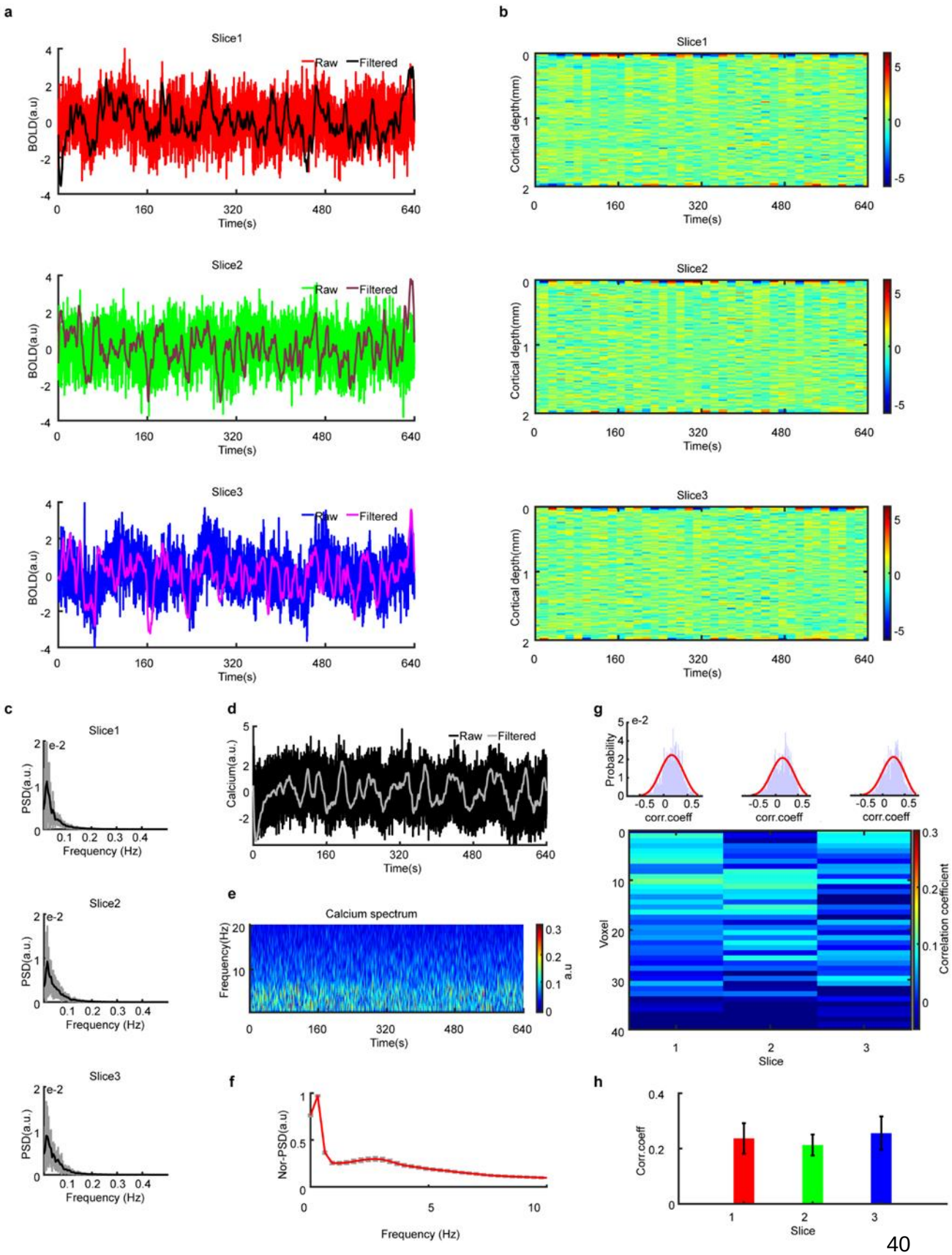
a
Slice1
Raw
Filtered
BOLD(a.u)
Time(s)
Slice2
Slice3
b
Cortical depth(mm)
c
PSD(a.u.)
Frequency (Hz)
d
Calcium(a.u.)
e
Calcium spectrum
Frequency(Hz)
a.u
f
Nor-PSD(a.u.)
g
Probability
corr.coeff
Voxel
Slice
Correlation coefficient
h
Corr.coeff

Fig.3. Spontaneous recorded calcium and fMRI signals within the three slices in resting-state. (a) Representative of normalized time course of raw and filtered (0.01-0.1Hz) BOLD signal from the three slices. (b) fMRI line profiles across the cortical depth. (c) Mean power spectrum density of the fMRI within the three slices from one representative rat (mean±S.D, n=25 trails). (d) A representative trail of spontaneous fluctuation of raw and filtered (0.01-0.1Hz) calcium signals. (e) Mean spectrum power density of calcium (meant ± S.E.M, n=11 rats, 189 trails). (f) The average spectrogram of the calcium (n=78 trails, from 3 rats), showing 1-5Hz band power. (g) Correlation patterns between calcium and BOLD fMRI from the three slices (25 trails), top row: distribution of the correlation coefficient from the corresponding slices, bottom row: average 2D correlation map between the calcium and BOLD signals across the cortical depth. (h) Statistical estimation of the correlation patterns within the three slices (one-way ANOVA, Bonferroni post-hoc test, F (2, 357) =1.63, P>0.1, n=11 rats).

Laminar spatiotemporal coupling features between BOLD and Ca^{2+}signals

The calcium spectrum analysis revealed a slow baseline (<0.5Hz) and 'faster' (1-5Hz, Fig.2e-2f & Fig.3e-3f) frequency band, which had been reported in our previous experiments[133]. To further investigate the laminar spatiotemporal coupling features between BOLD and Ca^{2+} signals, we decomposed the Ca^{2+} signals and extracted the 1-5Hz power spectral profiles for preforming cross-correlations analyses in both evoked and resting-state conditions. Fig.4a shows the averaged cross-correlation patterns for each individual trails from all animals, showing a lag time of 1-5s earlier Ca^{2+} events at maximum cross-correlation coefficient. The resting-state trails showed much-varied coupling features as many outliers were observed (Fig.4a, top row). However, the evoked trails displayed a more uniformed trend of temporal features (Fig.4a, bottom row). In addition, the evoked conditions showed a much higher cross-correlation coefficient than the resting-state. Statistical analysis revealed significant earlier Ca^{2+} events than the BOLD fMRI signals in evoked conditions with a median lag time of -1.4s, -1.9s and -2.0s for the three slices, respectively (Fig.4b, evoked, median and interquartile range: 25th and 75th percentiles, slice1 vs. slice2: p=3.8*e-4, slice1 vs. slice3: p=1.8*e-4).

Next, we conducted voxel-wise cross-correlation analyses along the cortical depth between Ca^{2+} and fMRI signals. Fig.4c-4d showed the averaged cross-correlation coupling features for all trails in resting-state (Fig.4c) and evoked conditions (Fig.4d). Either condition showed an earlier Ca^{2+} event than the hemodynamics along the cortical depth. Nevertheless, the evoked conditions showed much stronger cross-correlation

patterns than the resting-state across the different cortical layers. In addition, the cross-correlation patterns along the cortical layers were much sparer and diverse than the evoked conditions, when look at the individual trails (Video.S2). Those results support that Ca^{2+} kinetics leading earlier dynamics than BOLD fMRI that can be applied to investigate the specific laminar features in evoked and resting-state conditions.

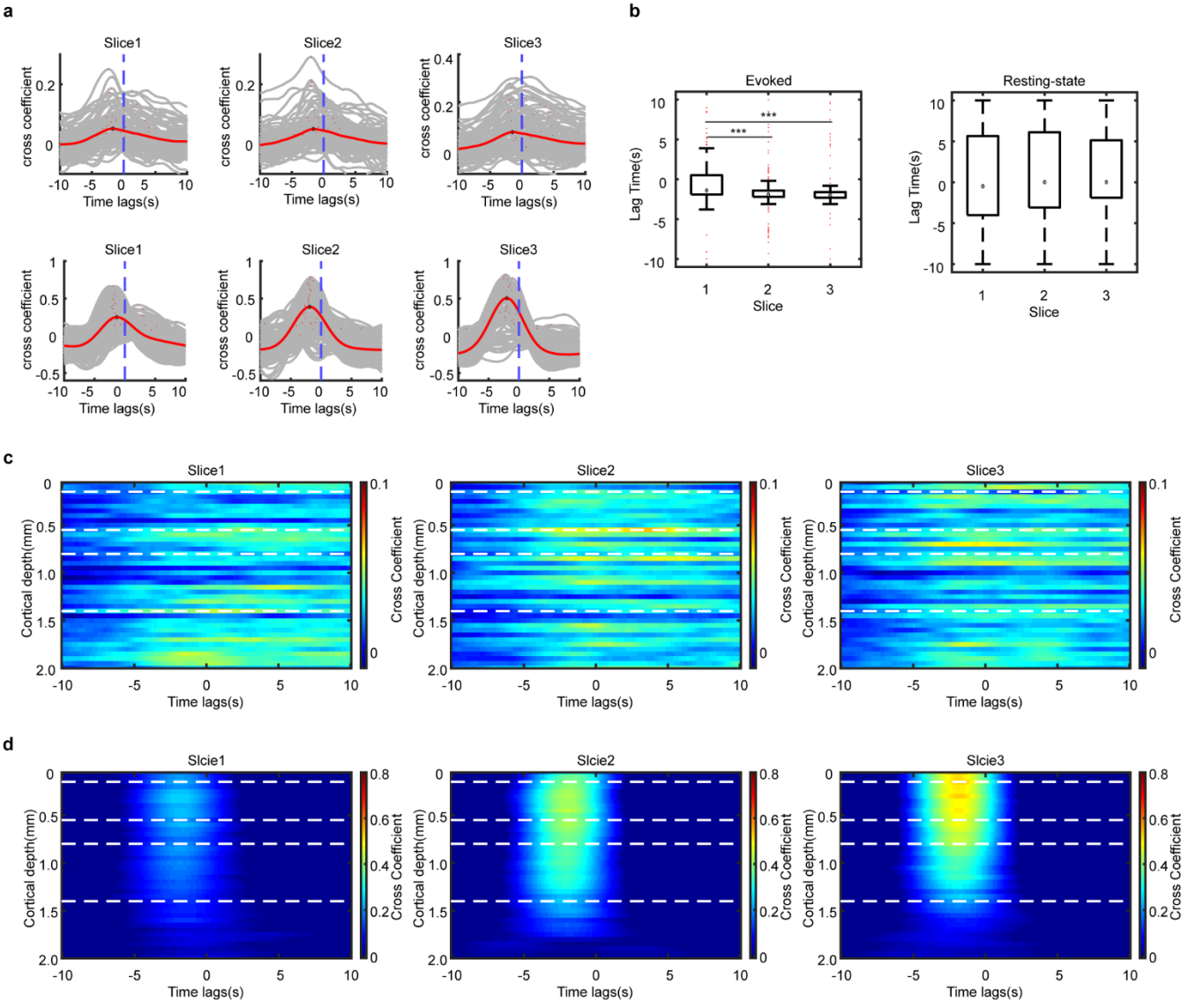

Fig.4. Cross-correlation patterns between calcium and BOLD within the three slices. (a) The cross-correlation analysis of BOLD fMRI and calcium power (1–5 Hz) profile from the calcium spectrogram illustrates earlier calcium events in both resting-sate and evoked conditions (11 rats, resting n=189, evoked n=191 trials). (b) Statistical estimations of the lag time at peak cross-correlation coefficient among the three slices (resting-state:-0.9s, -1.1s, -0.8s for the three slices in resting-state, 11 rats, n=97 trials, evoked:-1.4s,

-1.9 and -2.0s for the three slices under evoked, 11 rats, 191 trails, boxplot: central dot is the median, interquartile range 25th and 75th percentiles denotes the maximum and minimum, outliers are showed by red dots, ***p<0.001, one-way ANOVA: slice1 vs. slice2: p=3.8*e-4, slice1 vs. slice3: p=1.8*e-4). (c-d) The cross-correlation patterns of BOLD and calcium power profiles along the cortical depths within the three slices under resting-state (top row, n=25 trails) and evoked conditions (bottom row, n=26 trails) from one representative rat, respectively. White dash lines indicating cortical Lyler1-6 along the 2mm depth.

2.1.4 Discussion

Taken together, we demonstrate the feasibility of our newly developed multi-slice line-scanning fMRI and Ca^{2+} imaging method for probing the neurovascular coupling patterns in unprecedented details along the cortical depth on rat brain. Our results revealed a greater role for calcium-leading events than BOLD signals both in evoked and resting-state conditions. The novelty of our method lies in implementing the direct neuronal dynamics with local hemodynamics at columnar level, mapping a wealth of distinct coupling features that were characterized by the dynamic neuronal events across the cortical layers. It is thus plausible that future and ongoing experiments, e.g. different neurotransmitter markers (glutamate, dopamine), non-BOLD fMRI (CBV, CBF) can be also applied in the current imaging modalities.

Our results mitigate disadvantages of conventional BOLD-fMRI, which generally utilizes the GLM (general linear model) to characterize the sensory evoked activations as a whole instead of inferring the individual voxel. Furthermore, we directly combined the cellular measurement of neural activity with laminar fMRI, allowing the interrogation of neurovascular couplings in a spatio-temporally precise manner. Under stimulation conditions, the three slices showed stronger activations in superficial/middle layers (layer 2-4), with the third slice holding stronger signal power than the other two slices (Fig.2c). In consistent with previous reports, stronger fMRI signal changes were observed at superficial layers, resulting from the ascending venous blood flows towards the pial surface[21, 134]. In addition, the bottom-up information arrives at layer 4 and spreads across the other layers, which drives the surrounding hemodynamic response changes locally and then widely spreads across the whole cortex[24, 33, 135]. Notably, the correlations between Ca^{2+} and fMRI signals showed uniformed patterns across animals, depicting a stronger relationship in the superficial layers (Fig.2g-2h) in the third slice. This further

indicates that microvasculature and micro-architecture of laminae differs along the cortical depth even within such a short patch of cortex[111], which leads to the distinct correlation patterns across the different layers.

In contrast to the evoked conditions, the resting-state showed sparer and more de-synchronous correlations between fMRI and Ca^{2+} across the cortex (Fig.3g-3h). This could be explained by the brain-state dependent characteristics, since the neurons and vascular oscillate intrinsically[136-138]. Previous studies assume that spontaneous hemodynamics indexing neuronal activities, which of no doubt displaying coupling features[132, 139]. However, Aaron T et al[138], demonstrated the weak correlations between hemodynamic signals and neural activity during resting-state under different brain states, underpinning complex coupling features that are not only driven by the local neural activities, but also by non-neural processes. Therefore, it should be cautious to interpret the correlations between fMRI and Ca^{2+} along the cortical depth, particularly under α-chloralose in our current imaging modalities.

The cytoarchitecture of cerebral cortex varies along the cortical depth with distinct connectivity patterns, embryonic origins and molecular profiles, which distributed along the 0.2-2.0mm cortical thickness[114]. Therefore, we implemented the Ca^{2+} recordings in the current project, trying to investigate the layer-specific neuronal activities. Results showed that neurons lead to an earlier event than the hemodynamics in both evoked and resting-state conditions (Fig.4a). Consistent with previous measurements that Ca^{2+} is a good indictor to predict the hemodynamic fluctuations[124, 140]. The cross-coefficients were much stronger in evoked than in resting-state, likely due to the more rhythmic and synchronous of neuronal activities driven by the electrical stimulations.

To further unravel the spatial coupling patterns within the different layers, cross-correlation analysis were also performed between the individual voxel timecourse and the Ca^{2+} signals. We found that both evoked and resting-state showed ~5s earlier neuronal activities than fMRI dynamics along the cortical depth (Fig.4c). The third slice displayed stronger couplings than the other two slices, which may account for by the closer distance between calcium recording site and slice displacement. Namely, the local neurons drive surrounding vascular events and propagate as it spreads to the far distant cortical layers

and slices[141]. Meanwhile, compared with the evoked conditions, the resting-state coupling patterns varied along the cortical depth and showed much more diverse and spare features trail-by-trail along the different layers (Video.S2), indicating a more heterogeneous hemodynamic coupling pattern.

In summary, we demonstrate here that our multi-slice line-scanning fMRI with Ca^{2+} recordings opens the door for probing the laminar-specific coupling features with ever-unprecedented details. The cortical neuronal activities leading earlier events along the different cortical layers in both evoked and resting-state. Nevertheless, we were not able to distinguish the earlier events into specific layers, due to the single focal Ca^{2+} recording site. However, this concurrent imaging modality offers a promising new tool for cognitive functional framework in further exploration for other parts of the cortex, particularly, those affected in clinical disorders. Furthermore, labeling specific neurons (e.g. with glutamate, potassium, and dopamine, etc.) and high spatiotemporal resolution make this platform more valuable and informative when studying brain dynamics in future experiments.

Limitations

Firstly, within a given patch of cortex, we were not able to investigate the column circuity on a macroscopic level of the whole brain. Secondly, the calcium fluorescence critically depends on the opsin expressing volume, which were affected by many factors, e.g., the virus titer, serotype, promoter, injected volume, and cytoarchitecture of the targeted regions. Last but not least, α-chloralose was applied in the current project indicating that the brain states may vary depending on the anesthesia depth. Therefore, the laminar coupling features warrant verification using ongoing developed techniques (e.g., labeling layer-specific neurons) and experimental paradigms (e.g., fully awake state).

2.2 Part 2: Bilateral line-scanning fMRI with intracellular calcium recording

2.2.1 Introduction

The laminar functional magnetic resonance imaging (fMRI) has dramatically widened our vision to decode the layer-specific details within given regions of the brain on human or animal models[16, 142]. For instance, the onset of fMRI response in layer 4 of the rat forepaw somatosensory cortex (FP-S1) mainly originates from the ascending feedforward thalamocortical input[16, 33]. While, layer 2/3 and layer 5 of the rat motor cortex displayed earlier onset of fMRI response *via* somatomotor corticocortical inputs[33]. Those findings demonstrated that the layer-specific fMRI fluctuation derives from different neural inputs or reflects discrepancy of cerebrohemodynamic activities due to vascular distributions across layers[102, 143]. The neurons in superficial (layer 1) and deep layer (layer 5-6) predominantly receive feedback corticocortical and thalamocortical projections[21]. While, the central layer (layer 4) neurons are mainly projected by the feedforward thalamocortical inputs[16, 21]. Thereby, the cortical layers functionally differ from each other in addition to their distinct anatomical and physiological properties, i.e., neural cell types/sizes, cytoarchitecture, metabolism[113, 144], etc. Furthermore, it has become clear that the superficial neurons project downwards into cortical areas, whereas the deep layers project back to upwards cortical layers as well as subcortically[100]. However, it remains elusive to dissect how fMRI signals are reflected or modulated *via* layer-specific neuronal processes.

To decipher the neuronal-related fMRI signals, investigators have built multimodal fMRI imaging platforms, which combine various neuro-methodologies, such as electrophysiology[10], fiber-based calcium recordings[11], optogenetics[90], two-photon microscopy[89], to probe the underlying neural activities. For instance, N.K. Logothetis et al. demonstrated the close link between local field potentials (LFPs) and BOLD (blood oxygenation level dependent) signals on anesthetized monkeys[10]. Later, J.B.M. Goense et al. revealed that fMRI signals coincide well with the gamma band of LFP[145]. J.H Lee et al. applied the optogenetic stimulation to specifically modulate the local excitatory neurons, which can be characterized by the BOLD-fMRI signals[90]. Despite the widespread application of these multimodal fMRI platforms, few studies have focused on

investigating the relationships between the neural activities and BOLD signals at the laminar level. Previously, Yu et al. have developed a line-scanning fMRI method with unprecedented spatial (50 μm) and temporal (50 ms) resolution to image the cortical layers on rat brain, showing distinct BOLD onset behaviors in FP-S1 and motor cortex upon sensory stimulations[33]. However, the underlying neuronal mechanisms need further clarifications. Furthermore, it remains how or if different stimulus paradigms modulate these temporal features across layers. Subsequently, Y. Albers et al. compared the BOLD temporal features across layers between the optogenetic-driven and sensory-driven fMRI imaging modalities[97]. They found faster BOLD onset time under optogenetic-driven paradigms as compared to the sensory-driven[97]. In addition, our previous studies (the first part in chapter I), based on this unparalleled line-scanning fMRI, have implemented an optical-based fiber recording system for simultaneous calcium signal detection to investigate the layer-specific events between BOLD and neuronal activities, namely, neurovascular coupling. Nevertheless, we extended the single slice acquisition to multi-slice imaging on rat FP-S1 region in this multimodal fMRI platform. Our preliminary results showed ~5s earlier calcium events than BOLD signals across the cortical depth. Furthermore, the BOLD response also showed laminar differences in such a short patch of confined region. However, those data were acquired in one hemisphere of the rat brain. It temped us to explore if and how the BOLD fluctuations interhemispherically interact with the neuronal activities in a layer-specific manner under contralateral or ipsilateral sensory stimulus.

The interhemispheric functional connectivity, particularly, the bi-hemispheric cortical connections have been demonstrated on both human and animals models[146, 147]. However, the underlying mechanisms for this bilateral symmetry remains largely to be elucidated. Our previous studies revealed brain-wide effects through corpus callosum mediated excitation/inhibition under callosal optogenetic stimulation[148]. Nevertheless, it is still unclear, if and to what extent the neuronal activities correlated with the BOLD fluctuations in the opposite hemisphere under contralateral or ipsilateral sensory stimulus. Therefore, to address this question, we have developed the bilateral line-scanning fMRI with concurrent calcium recording system to acquire bi-hemispheric BOLD responses and unilateral calcium signals on rat FP-S1 regions. Either bilateral stimulus or resting-state

fMRI showed a bilateral symmetry as well as earlier calcium events (~5s) as compared with the BOLD signals along the cortical layers. However, the contralateral BOLD and calcium signals showed inverse correlations under unilateral sensory stimulation. These measurements, on the one hand, suggest that the layer-specific interhemispheric neurovascular couplings may be modulated by distinct neuronal inputs (global brain-wide), on the other hand, further demonstrate the potential application of this multimodal fMRI platform to investigate the interhemispheric functional connectivity in a layer manner.

2.2.2 Materials and Methods

Animals

All experimental procedures were approved by the state authority (Regierungspräsidium, Tübingen, and BadenWürttemberg, Germany) and conducted in accordance with the guidelines. Eighteen Sprague-Dawley rats were employed in the project (9 rats for calcium recording and 2 rats were excluded for further analysis due to brain damage or weak responses). The animals were habituated individually/group at a 12hr-12hr light-dark cycle with food and water *ad libitum*.

Surgery

All procedures were described in a previous study[72]. Rats were initially anesthetized with isoflurane (5% induction, 1.5% maintenance). Each rat was orally intubated and placed on a mechanical ventilator (SAR-830/AP, CWE). Plastic catheters were inserted into the right femoral artery and vein to allow monitoring of arterial blood gasses and administration of anesthetics. After surgery, each rat was given an intravenous bolus of a-chloralose (60 mg/kg) and isoflurane was discontinued. Anesthesia was maintained with a-chloralose (26.5 mg/kg/hr) in combination with pancuronium bromide (4 mg/kg/hr) to reduce motion artifacts. The rats' rectal temperature was maintained at around 37°C. To prevent head motion, rats were secured in a head holder with a bite bar. All relevant physiological parameters (end-tidal CO_2, rectal temperature, heart rate, and arterial blood pressure) were continuously monitored during imaging. The pulse sequence–based trigger and stimulation control were established using the BIOPAC system (Goleta, USA) and Master-9 A.M.P.I system (Jerusalem, Israel).

Viral vector injection and optical fiber implantation

The viral vectors (AV-1-PV2822 AAV5.Syn.GCaMP6f.WPRE.SV40) expressing GCaMP in neurons were purchased from University of Pennsylvania Vector Core. Viral vectors were injected in the forepaw region of the primary somatosensory cortex (S1FL) of 3-4 weeks old rats. For the stereotactic injection procedure, rats were initially anesthetized with isoflurane. After exposing the skull, a small bur hole was drilled. A nanoliter injector (WPI, FL) was used to place a 35-gauge needle at the proper coordinates in the

stereotactic frame. Injections were performed slowly over 5-6 min and the needle was slowly removed after being kept in the injection site for 10 min after finishing the injection. The injection sites of S1FL were as follows: AP= 0.2 mm; ML= 3.7 mm injections each 400 nL at 1.2 mm and 0.7 mm depth. After 6-8 weeks of viral expression, an optical fiber (FT200EMT: NA = 0.39, 230 mm cladding diameter; Thorlabs) was inserted through the burr hole on S1FL (AP = 0.2 mm; ML = 4.0 mm; DV = 1.0~1.3 mm). The optical fiber was fixed on the skull with glue. Then, the skin was sutured to cover the glue with the optical fiber (9m length) extending outside of the rat head.

MRI experiments

Under alpha-chloralose anesthesia, all MRI was carried out on a 14.1 T/26 cm horizontal bore magnet (Magnex) interfaced to an Avance III console (Bruker). A transceiver surface coil (Ø 10mm) was positioned over the whole brain to acquire images. Electrodes were placed on the left and right forepaws to deliver trains of 300μs (3Hz, 4s, 2.5mA) in each epoch. To locate the fMRI signals, 3D echo planar imaging (EPI) sequence was applied with the following parameters: 1.5s TR, 11.5ms TE, 19.2×19.2×19.2mm FOV, 48×48×48 Matrix, 0.4×0.4×0.4mm^3 resolution, 410 TRs in total. Anatomical images were quickly acquired by using the rapid acquisition with relaxation enhancement (RARE) sequence with the same geometry displacement as that in EPI. Once the geometry position for BOLD activations was located in the left and right FP-S1, we could place our line scanning slices to cover the most activated regions in left and right hemisphere. The laminar fMRI data were acquired using the following parameters: 60ms TR, 8ms TE, 6.4×3.2mm FOV, 128×32 Matrix, temporal (60ms) and spatial (50μm) resolution, 400 repetitions, total scan time=768s, slice thickness 1.4mm. Two saturation slices were applied to suppress the signals outside FP-S1 and the phase-encoding gradient was turned off. The cortical space between two saturation slices was 1.2~1.5mm.

Simultaneous calcium recording

The light path system for the calcium signal recording was built up based on our previous study[45] (Fig.3). A 488nm laser (OBIS 488LS, Coherent Inc., USA.) was applied as the excitation light source. The beams passed through a continuously variable metallic ND filter (NDC-50C-4M-A, Thorlabs) and were reflected by a reflection mirror to the dichroic

mirrors (F48-487, reflection 471-491 nm, >94%; transmission 500-1200 nm, >93%; AHF Analysentechnik), and focused through a tube lens (AC254-030-A1-ML; Thorlabs) into a multimode optical fiber (FT200-EMT; NA = 0.39; 230μm diameter, Thorlabs). Laser intensity was measured at the fiber tip (~5μW for neuronal calcium recording) by an optical power meter (PM20A, ThorLabs). The emitted fluorescent signal was guided back through the same fiber. Firstly, passing the dichroic mirror and optical filter (F37-516; 500-550nm band pass, AHF Analysentechnik), and then focused by the tube lens (AC254-030-A1-ML, Thorlabs) to directly project to a silicon photomultiplier (MiniSM 10035, SensL, Germany). Finally, the signal was amplified by voltage amplifier (DHPVA-100, Femto, Germany) before detected by the analogue input module of BIOPAC system (Goleta, USA) at a sampling rate of 5000Hz.

Data processing and statistical analysis

3D-EPI BOLD fMRI processing

To locate and confirm BOLD responses under stimulation in FP-S1 region, the 3D-EPI fMRI data were analyzed using AFNI software (NIH; https://afni.nimh.nih.gov/). Detailed descriptions of signal procedures can be found in our previous published papers[126]. The hemodynamic response function (HRF) model was used to generate BOLD fMRI map: BLOCK (d, p), which convolved (linear program 3dDeconvolve in AFNI) with a square wave of duration d and made a peak amplitude of p (the amplitude of basis function and usually set to 1). The HRF model is defined as follows:

$$HRF(t) = int(g(t-s), s = 0..\min(t, d))$$

Where g (t) =$g(t) = t^q e^{-t}/[q^q e^{-q}]$, q = 4, d is the square wave of duration.

Line-scanning BOLD fMRI processing

Line scanning BOLD fMRI line profiles were extracted from the raw FID files by applying our custom-written Matlab codes. BOLD signal intensity was plotted along the cortical depth as a function of time (50μm resolution along the 2-mm cortical depth, 768s for each

trail). We define the half maximum signal magnitude intensity as the cortical surface for each trail[33]. The BOLD line-scanning fMRI percentage change map was made by averaging the line profile time-series from each epoch (1.2s-pre-4s-on-18.8s-off, 32 epochs/trail) and converted to percentage changes by subtracting and dividing each time-series by the average of 20 TRs (1.2s-pre) prior to stimulus. The formula for calculating the line-scanning BOLD signal percentage change:

$$\mathrm{Signal(i)} = \frac{\mathrm{S(i)} - \mathrm{S(base)}}{\mathrm{S(base)}}$$

Signal(i) is the signal percentage change, i = 0: TR: 24s, S(i) is signal intensity, and S(base) is the averaged pre-stimulation signal intensity from 0 to1s.

Ca^{2+} signal processing

The calcium time series were first segmented to match the fMRI data length and demeaned within each trial for further analysis by our custom-written Matlab codes. For evoked conditions, the calcium relative percentage change of fluorescence ($\Delta F/F$) was calculated, where ΔF is the 'noise-corrected' signal ($F-F_0$) and F_0 is the background signal intensity (0-1.2s, pre-stimulation). The calcium power spectrum density (PSD) was calculated by applying the *pwelch* function in Matlab (2500 Discrete Fourier transform points; 1s window length; 50% overlap) [127]. The calcium spectrogram and signal decomposition (power spectral profile:1-5Hz) were extracted by using the *timefreq* function[128] (https://sccn.ucsd.edu/eeglab/index.html).

Coherence analysis of the line scanning fMRI between the two slices

The BOLD line profile time series were firstly demeaned for all the trails acquired from each animal. Then, the demean signals were band-pass filtered to 0.01-0.1Hz in MATLAB by using *butter* and *filtfilt* functions. Finally, the pre-processed fMRI signals from the bilateral slices were z-scored to perform the coherence analysis across trails by applying the *mscohere* function in MATLAB (Hamming window length: 2000, FFT length: 2000, overlap 50%). The frequency resolution of coherence is 1/120s=0.0083Hz.

Correlation analysis of fMRI between the bilateral slices

Under the unilateral stimulation paradigms, i.e., either stim1 or stim2 was on, correlation analyses were performed to explore the relationships of BOLD signals from the evoked hemisphere and the contralateral non-stimulated hemisphere. The BOLD line profile time series from the bilateral slices were firstly demeaned. Then, band-pass filtered to 0.01-0.1Hz in MATLAB by using *butter* and *filtfilt* functions. Finally, the pre-processed fMRI signals from the evoked hemisphere were averaged and z-scored to correlate with the non-stimulated contralateral hemisphere BOLD signals (zscored) across the cortical depth by applying the *zscore and corr* function in MATLAB.

Cross-correlation analysis between fMRI and Ca^{2+}

To investigate the spatiotemporal features between fMRI and calcium. Cross-correlation analysis was performed between the line profiles and calcium signals in both evoked and resting-state conditions. The mean spectrum calcium power profiles along the time (i.e. 1-5 Hz) and voxel-wise fMRI time series (40 voxels) were extracted and cross-correlated in MATLAB using the x*corr* function with a maximum of 400 data points. The cross-correlation coefficient were averaged along the cortical depth (40 voxels) and plotted together to produce the cross-correlations maps (Fig.4a-4b). Based on these cross-correlation patterns, the lag times between the calcium and fMRI signals were extracted at the maximum cross coefficient. To further specify the laminar spatiotemporal features between Ca^{2+} and BOLD signals along the cortical depth, the color-coded cross correlation maps were also produced by plotting each individual voxel-Ca^{2+} cross-correlation coefficient along the cortical depth (Fig.4c-4d). Two-sample *t-test* was applied to distinguish lag times within the two slices by using the *ttest2* function in MATLAB.

Immunofluoresencent staining of the brain slices

To confirm the GCaMP6f expression in S1FL region after 3-4 weeks of virus injection. Firstly, we euthanized and perfused the rats in pilot studies. Then, the brain tissues were carefully removed and fixated in 4% paraformaldehyde (PFA). To avoid cell damage, the fixated brain tissues were exposed in the 30% sucrose hypertonic solution for later cryostat sectioning. Finally, the immunofluoresencent staining experiments were

conducted to localize the GCaMP expression. The detailed experimental procedures can be found in our previous published papers[126, 129].

2.2.3 Results

Establishment of Bilateral line-scanning fMRI and Ca^{2+} recording.

To enable simultaneously recording of laminar fMRI and calcium, we developed the bilateral line scanning fMRI with calcium recoding system. Figure 1 shows the multi-modal imaging of the layer-specific fMRI in the left and right hemisphere at FP-S1 regions. For the bilateral stimulus paradigms, i.e. both stim1 and stim2 were on, and BOLD responses were detected from both hemispheres (Fig.1a). Genetically encoded fluorescent calcium (GCaMP6f) sensors were expressed in the right FLS1 (Fig.1b). Fig.1c shows the bilateral slices geometrical placement in the left and right FP-S1 covering the most activated regions (Fig.S1 and Video.S1). Two saturation slices were applied to suppress the signals outside FP-S1. Therefore, this multi-modal imaging system (Fig.1d) allowed us to investigate the laminar-specific neurovascular coupling features under different stimulation paradigms, e.g. either stim1 or stim2 was on, or both were on/off.

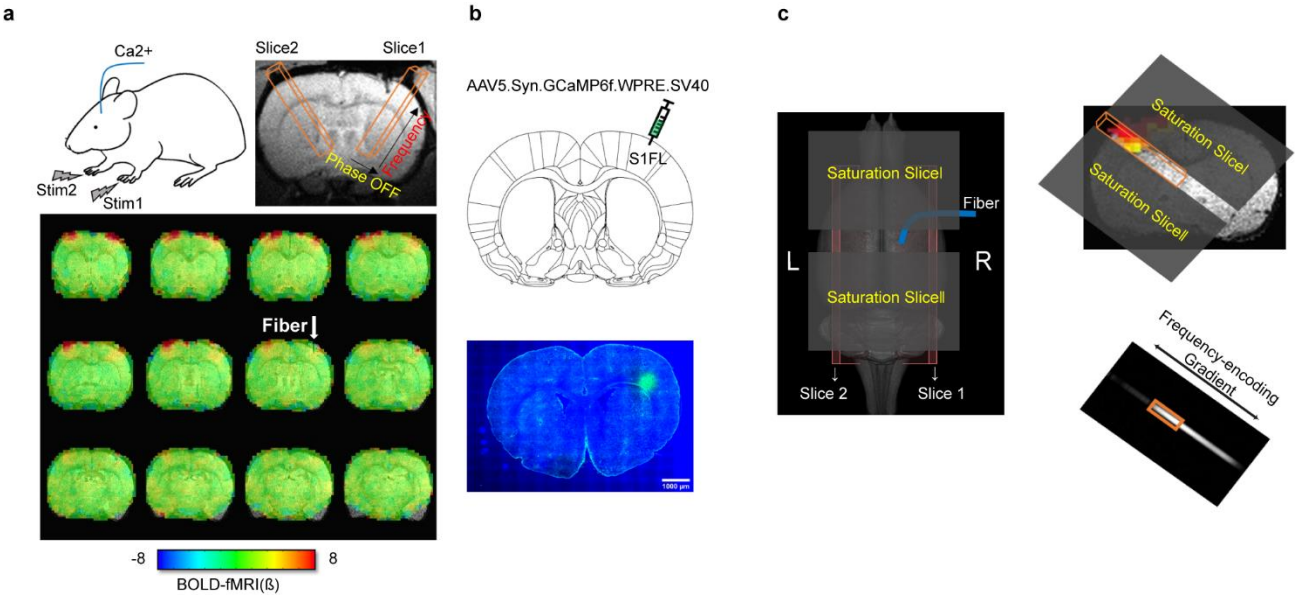

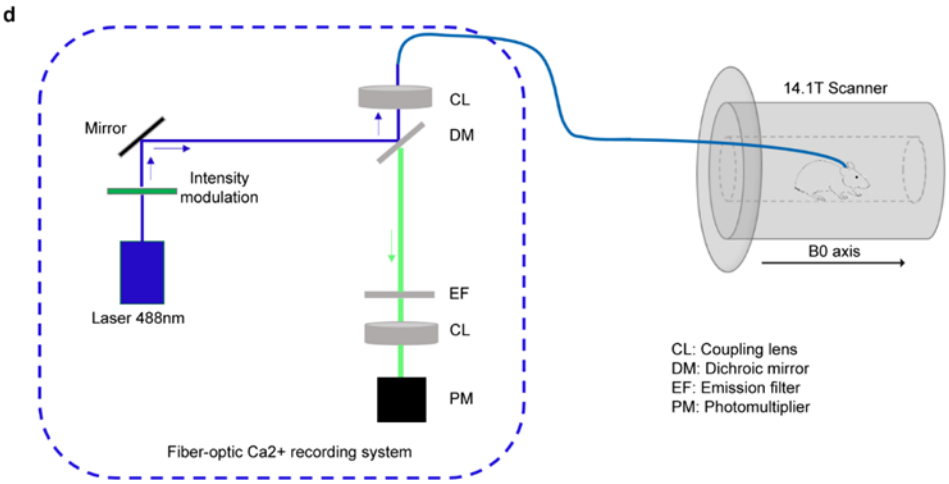

Fig.1. Setup for simultaneous fiber-optic calcium recording and bilateral line-scanning fMRI. (a) Experimental designs and BOLD responses at bilateral slices of FP-S1 regions. Top row: bilateral stimulus were given; bottom row: 3D-EPI BOLD fMRI map overlaid on anatomical image showing BOLD responses at FP-S1 in the two hemispheres (3 rats, n=24 trails, 3Hz, 4s, 2.5mA). (b) Schematic of virus injection in FP-S1 (upper panel), immunostaining images showing calcium expression in FP-S1 (lower panel), co-localizations of calcium in neurons (green) and DAPI (blue). (c) Bilateral line-scanning slice geometrical displacement, the phase-encoding gradient was off and only the frequency-encoding gradient was on, two saturation slices were applied to suppress the regions outside of FP-S1. (d) Schematic drawing of the multi-modal imaging system for calcium and fMRI recording.

Concurrent bilateral line-scanning fMRI and Ca^{2+} recording.

The bilateral BOLD fMRI line profiles were plotted as a function of time (Fig.2a). When keep repeatedly acquiring these line profiles, we can extract and plot them out for visualization of the hemodynamics at both hemispheres (Fig.2b-2d). These responses were robust in every imaging epochs. The domain frequency of the bilateral bold fMRI was 0.01-0.1Hz (Fig.2e), which is consistent with the previous published reports[33, 68]. Simultaneously, the calcium signals were also acquired upon stimulations (Fig.2f-2i). These results indicated the successful establishment of this multi-modal imaging system on rodents.

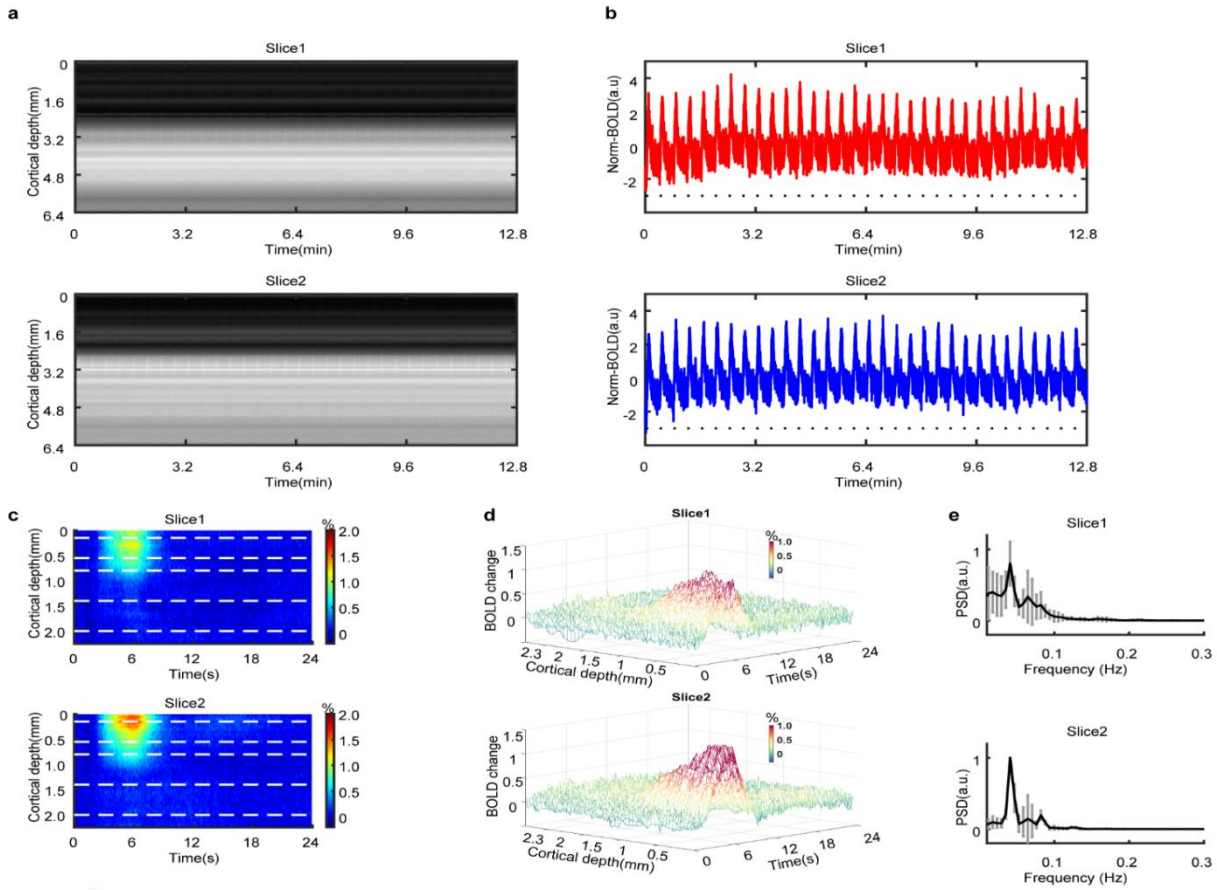
a
Slice1
Cortical depth(mm)
Time(min)
Slice2
b
Norm-BOLD(a.u)
c
%
Time(s)
d
BOLD change
Cortical depth(mm)
e
PSD(a.u.)
Frequency (Hz)

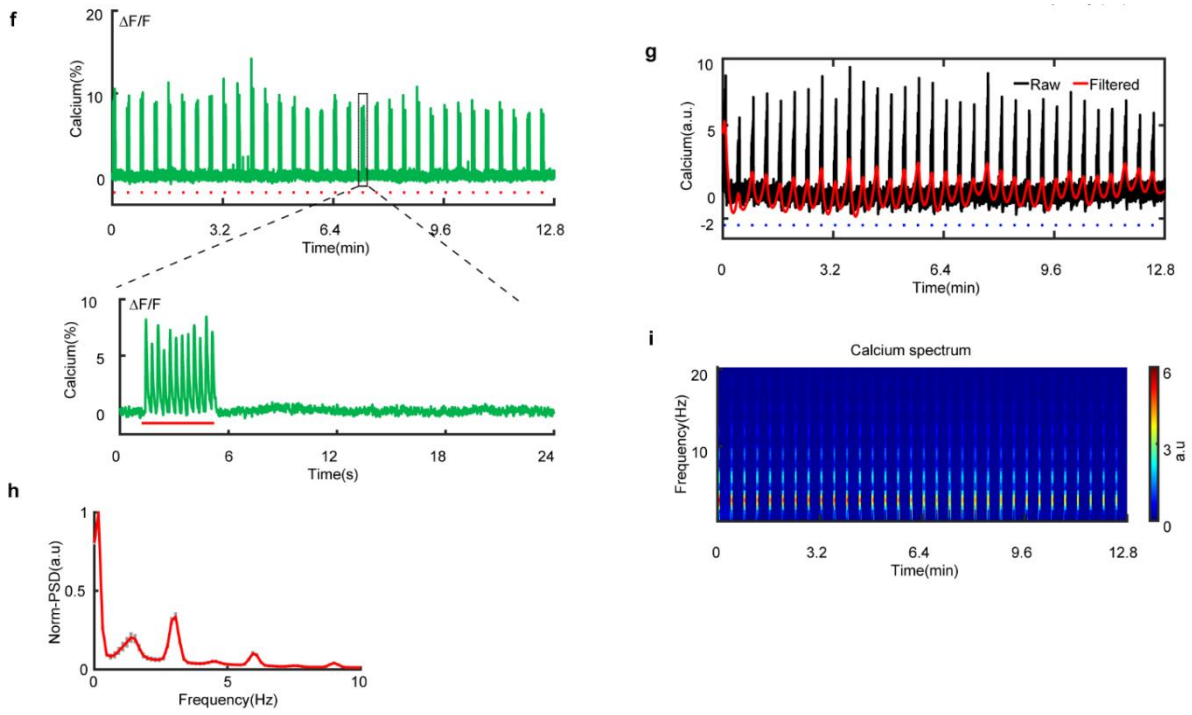
f
ΔF/F
Calcium(%)
Time(min)
Time(s)
g
Raw
Filtered
Calcium(a.u.)
h
Norm-PSD(a.u)
Frequency(Hz)
i
Calcium spectrum
Frequency(Hz)
a.u

Fig.2. Simultaneous recorded calcium and fMRI signals under bilateral forepaw stimulation. (a) Animal-wise cortical line profiles plotted as a function of time (3 rats, n=24 trails). (b) Averaged BOLD time series (3 rats, n=24 trails, block dots denote block stimulations: 1.2pre-4s-on-18.8s-off). (c) Mean BOLD line profiles within epochs (24s/epochs) for the 2-mm cortical depth (3 rats, n=24 trails, white dash lines: layer1-6). (d) 3D plot of averaged epochs of BOLD signal changes (3 rats, n=24 trails). (e) Averaged power spectral density from one representative rat (n=8 trails). (f) The averaged raw time course of calcium signals from two animals (n=16 trails, red dots denote 4s stimulation on, block stimulations: 1.2pre-4s-on-18.8s-off), zoomed figure shows the calcium signal in one epoch. (g) A representative trail of raw and filter (0.01-0.1Hz) calcium time course; blue dots are the stimulus durations. (h) Normalized spectrum power density of calcium (mean±S.E.M, 7 rats, n=75 trails). (i) Averaged spectrogram of calcium signals from three animals, showing a frequency band of 1-5Hz (n=22 trails).

Under resting-state conditions, i.e. both stim1 and stim2 were off, BOLD and calcium signals were recorded. Fig.3a-3b show an example of BOLD time courses from left (Slice2) and right (Slice1) hemisphere. Likewise, the domain frequency is 0.01-0.1Hz (Fig.3d). In addition, slow calcium fluctuations were observed and showed a higher robust power at 1-5Hz band (Fig.3c&3e). Coherence analysis further shows that BOLD fMRI line profiles from the left and right hemisphere were highly interconnected at 0.01-0.1Hz (Fig.3f). These results further allowed us to investigate the layer-specific cross correlations analysis between the calcium and BOLD signals.

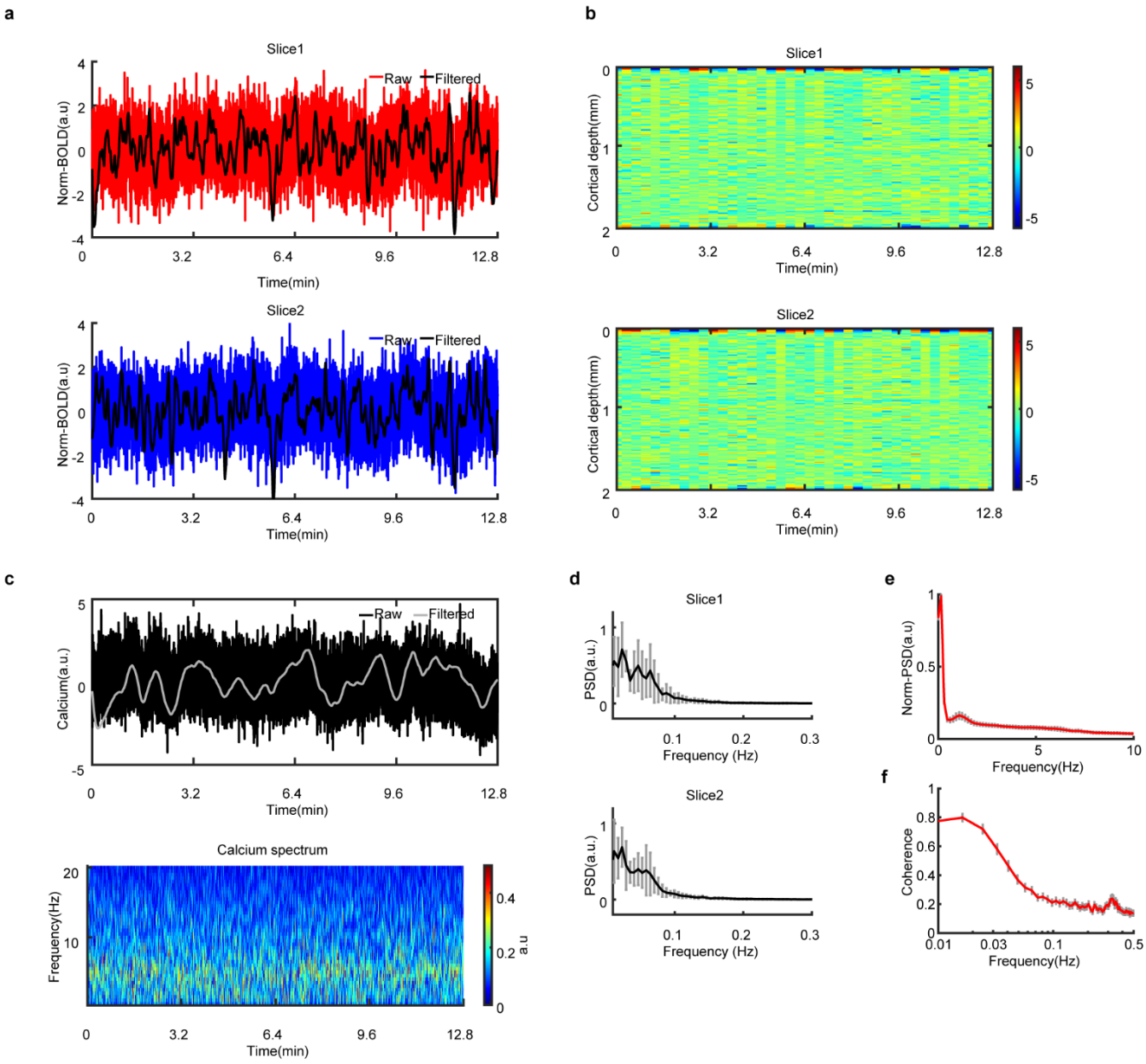

Fig.3. Simultaneous recorded calcium and bilateral fMRI signals under resting-state. (a) A representative trail of raw and filtered (0.01-0.1Hz) BOLD line profile signal. (b) fMRI line profiles across the cortical depth. (c) *Top row:* A representative trail of spontaneous fluctuation of raw and filtered (0.01-0.1Hz) calcium signal. *Bottom row:* The average spectrogram of calcium signals from one animal (n=6 trails). (d) Mean power spectrum density of the fMRI from one representative rat (mean±S.D, n=6 trails). (e) Mean spectrum power density of calcium signals (meant±S.E.M, 7 rats, and n=74 trails). (f) The averaged BOLD coherent coefficient between the two slices (meant±S.E.M, 7 rats, n=74 trails).

Laminar neurovascular coupling features under bilateral stimulus and resting-state.

Aforehand, we have successfully established the bilateral line scanning fMRI with calcium recording on rat brain. Therefore, we can go deep further to investigate the coupling features between the BOLD line profiles and calcium signals along the cortical depth. Fig.4a-4b show the cross-correlation patterns across trails in bilateral stimulus and resting-state conditions, respectively, showing earlier calcium fluctuations than BOLD signals. Notably, the cross coefficients were higher in evoked states than that in resting-state. Under bilateral stimulus condition, the calcium showed a median time of 1.38s, 1.68s for Slice1 and Slice2, respectively. While, under resting-state, the calcium showed 1.86s earlier for Slice1 and 0.42s for Slice2. Further analysis revealed the earlier calcium fluctuations along the 2-mm cortical depth in the left and right hemisphere under evoked and resting-state (Fig.4c-4d). We did not find any significant difference in the lag times across those two slices in evoked or resting-state conditions (Fig.4e).These results support that calcium signal behaves earlier than BOLD fluctuation along the cortical depth.

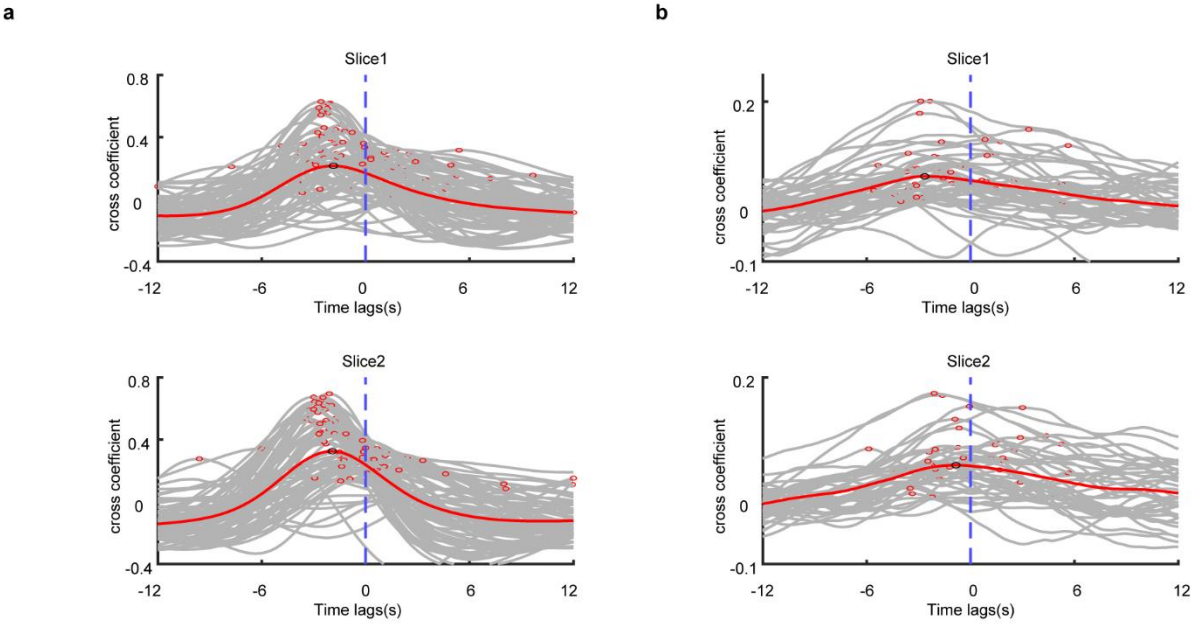

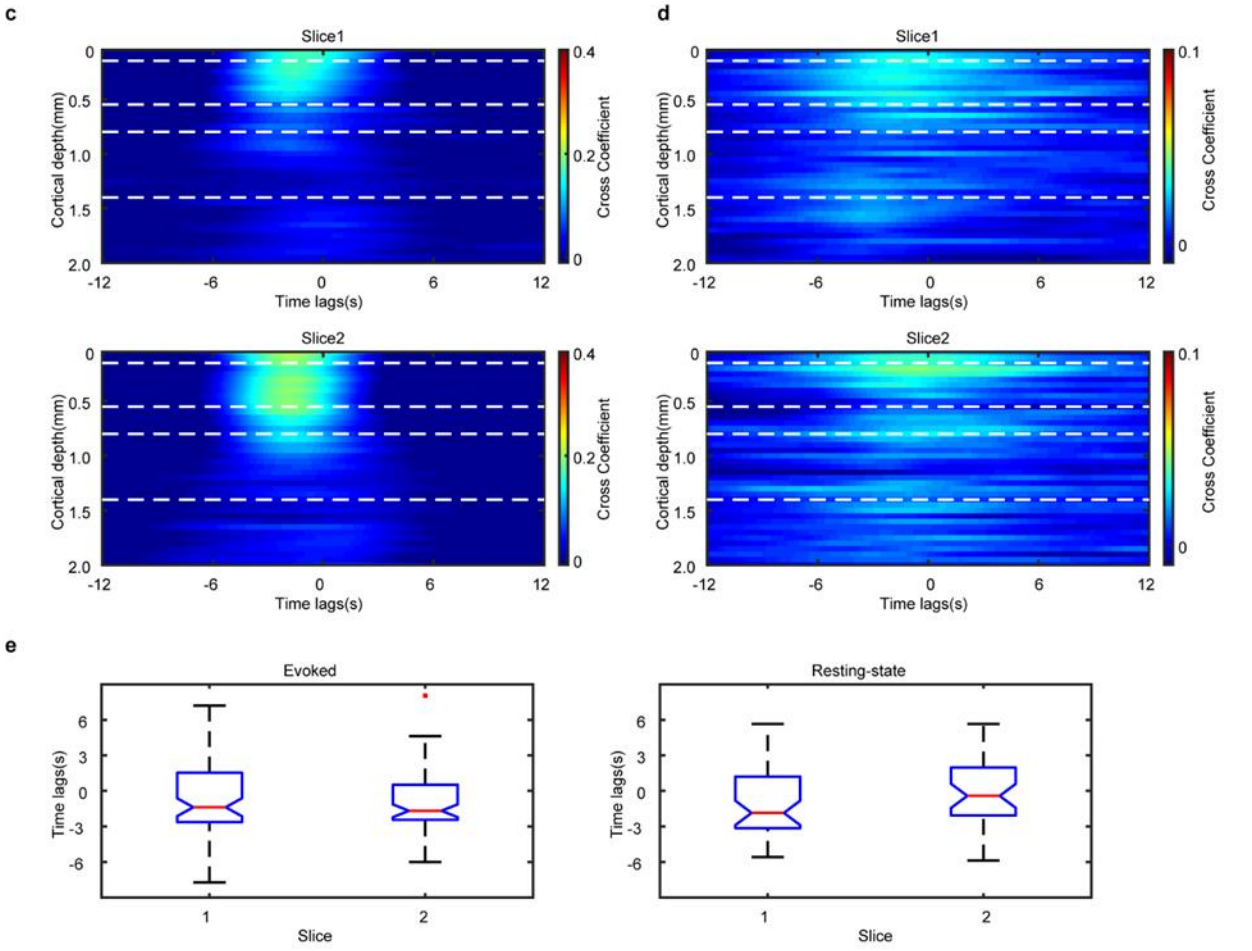

Fig.4. Cross-correlation patterns between calcium and BOLD within the two slices. (a-b) The cross correlations analysis of BOLD fMRI and calcium power (1–5 Hz) profile illustrates earlier calcium events in both evoked (n=75 trails) and resting-state conditions (n=39 trails), respectively. (c-d) The cross-correlations patterns of BOLD and calcium power profiles along the 2-mm cortical depths within the two slices under evoked (n=75 trails) and resting-state conditions (n=39 trails), respectively. White dash lines indicating cortical layer 1-6. (e) Statistical estimations of the lag time at peak cross-correlation coefficient with the two slices (evoked:-1.38s, -1.68s for the two slices; resting-state:-1.86s, -0.42s for the two slices, boxplot: central dot is the median, interquartile range 25th and 75th percentiles denotes the maximum and minimum, outliers are showed by red dots, two-sample *t-test*).

Laminar neurovascular coupling features under unilateral stimulus *(Slice2 or Slice 1-evoked)*

Under unilateral stimulus, i.e. only stim2 was on, BOLD fMRI and calcium singles were acquired and analyzed. The evoked hemisphere (Slice2) shows robust BOLD responses compared to the non-stimulated contralateral hemisphere (Slice1) (Fig.5a-5b). Coherence analysis supports the BOLD signals from the two hemisphere are highly

related at 0.01-0.1Hz (Fig.5c). Furthermore, the BOLD signals from Slice1 and Slice2 showed positive correlations along the cortical layers, which is consistent with the coherent results (Fig.5d). Cross-correlation analyses further showed zero lags of the BOLD signals from the two slices (Fig.5e). Similarly, the calcium shows earlier events than BOLD signals along the cortical depth in Slice1 (Fig.5f). However, the BOLD signals from Slice2 were negatively correlated with the calcium fluctuations (Fig.5g). Despite Slice1 was not directly stimulated, the calcium signals still showed a 1-5Hz power bands (Fig.5h). Further statistical analysis reveal significant temporal lag time between the two slices, i.e., Slice1: -0.54s and Slice2: 4.08s, which indicates that the BOLD signals showed an earlier dynamics than the contralateral neuronal activities upon stimulation (Fig.5i, *p<0.01*).

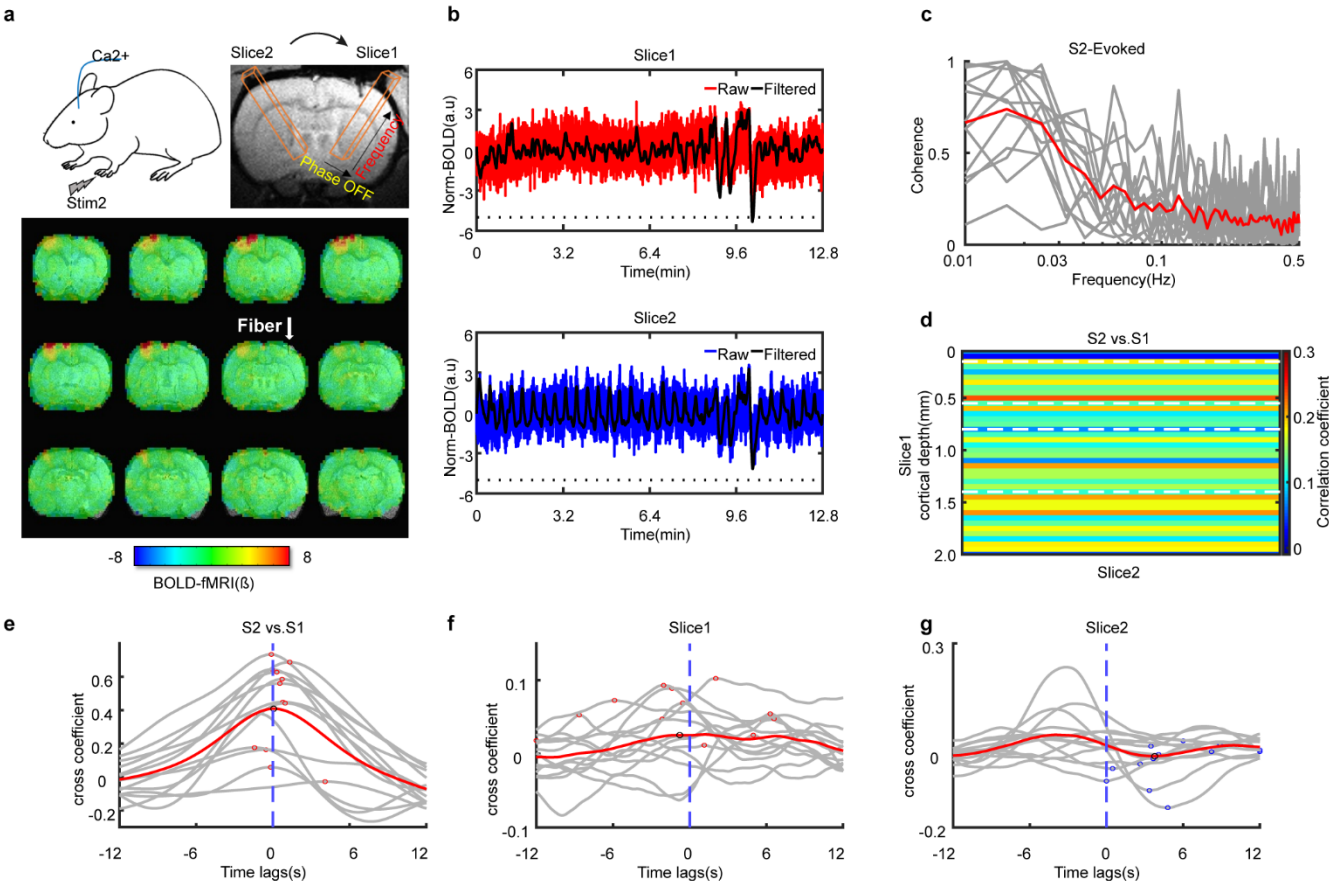

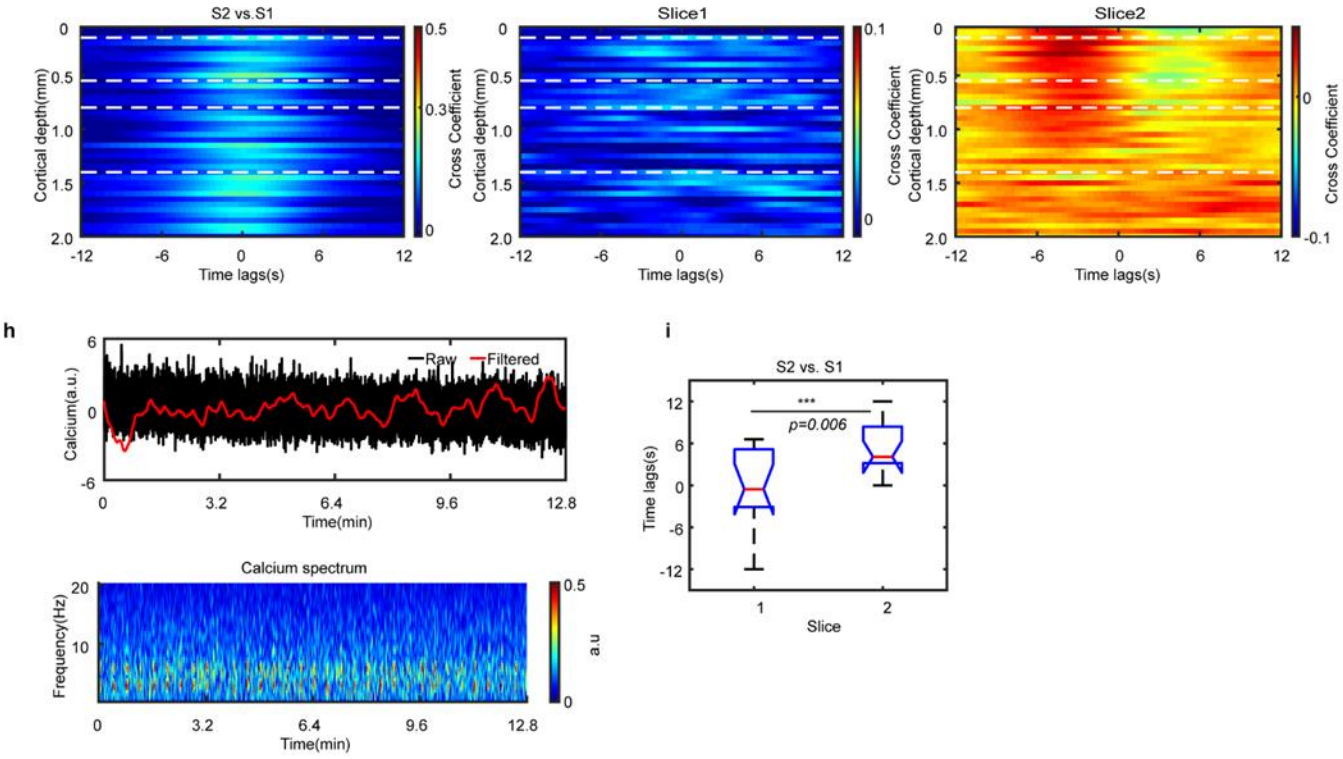

Fig.5 Bilateral line scanning fMRI mapping under unilateral stimulation in Slice2. (a) Experimental designs and BOLD responses at unilateral side in Slice2. *Top row:* only stim2 was given electrical stimulus, *bottom row:* 3D-EPI BOLD fMRI map overlaid on anatomical image showing BOLD responses on FP-S1 at 'Slice2' hemisphere. (b) A representative trail showing raw and filtered (0.01-0.1Hz) line profile BOLD fMRI. (c) Coherence analysis of the BOLD line profiles between the two slices, grey lines are the individual trails and red line is the mean (3 rats, n=13 trails). (d) Linear correlation of BOLD signals from the two slices. (e) Cross-correlation analysis of the BOLD fMRI signals from the two slices. (f-g) *Top row*: cross-correlation coefficient between the calcium power (1-5Hz) and line profiles across the different trails in slice1&2; grey lines are the individual trials, read line is mean, dark/red circle is the lag time at maximum cross-correlation value. *Bottom row:* averaged cross-correlation analysis between the calcium power (1-5Hz) and BOLD line profiles along the 2-mm cortical depth within the bilateral slices; white lines are the layer1-6 (3 rats, n=13 trails). (h) *Top row:* a representative trial of raw and filtered (0.01-0.1Hz) calcium time course, *bottom row:* Averaged calcium power spectrogram along the time (3 rats, n=13 trails). (i) Statistical analysis of the lag time at maximum cross-correlation value within the two slices (two-sample t-test, 3 rats, n=13 trails, boxplot: central red line is the median, interquartile range 25th and 75th percentiles denotes the maximum and minimum, Slice1: -0.54s, Slice2: 4.08s, ***p<0.01).

Contrast to the above unilateral stimulus paradigms, instead, Slice1 was the stimulated hemisphere. Fig.6a-6b show the BOLD responses from the stimulated hemisphere (Slice1) and non-stimulated hemisphere (Slice2). Likewise, the coherence and cross-correlation analysis showed highly interconnection of the BOLD signals from Slice1 and Slice2 (Fig.6c &6e). The 2D correlation map shows a diverse pattern of the BOLD signal from the two slices. The cross-correlation analysis revealed earlier calcium events than

BOLD signals in Slice1 (Fig.6f). However, the BOLD signals from Slice2 and the calcium signals showed a negative cross-correlation pattern (Fig.6g). Furthermore, the statistical analysis showed significant calcium leading events than BOLD signals across the two hemispheres, i.e., Slice1: -2.28s and Slice2: -5.58s (*p<0.05*).

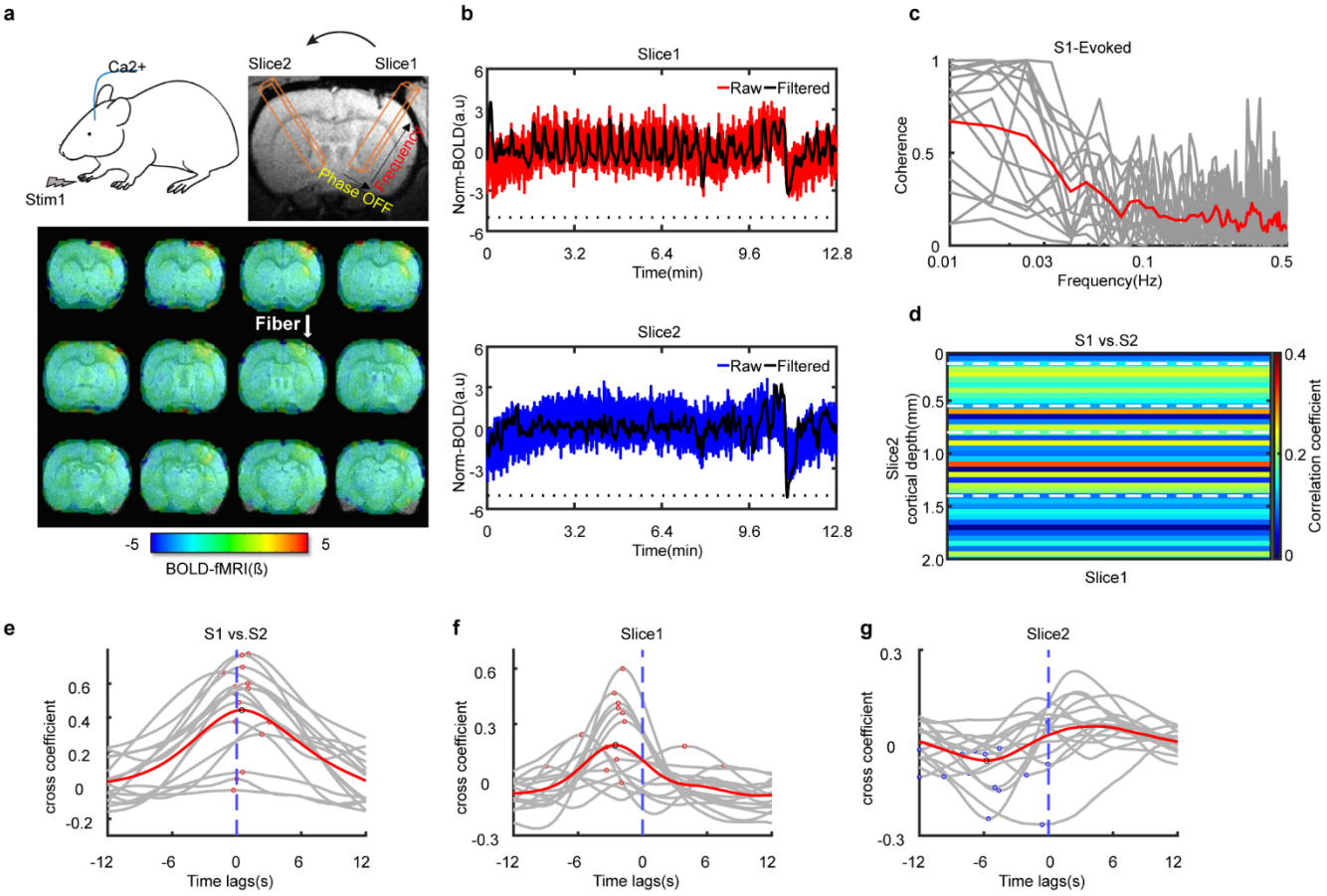

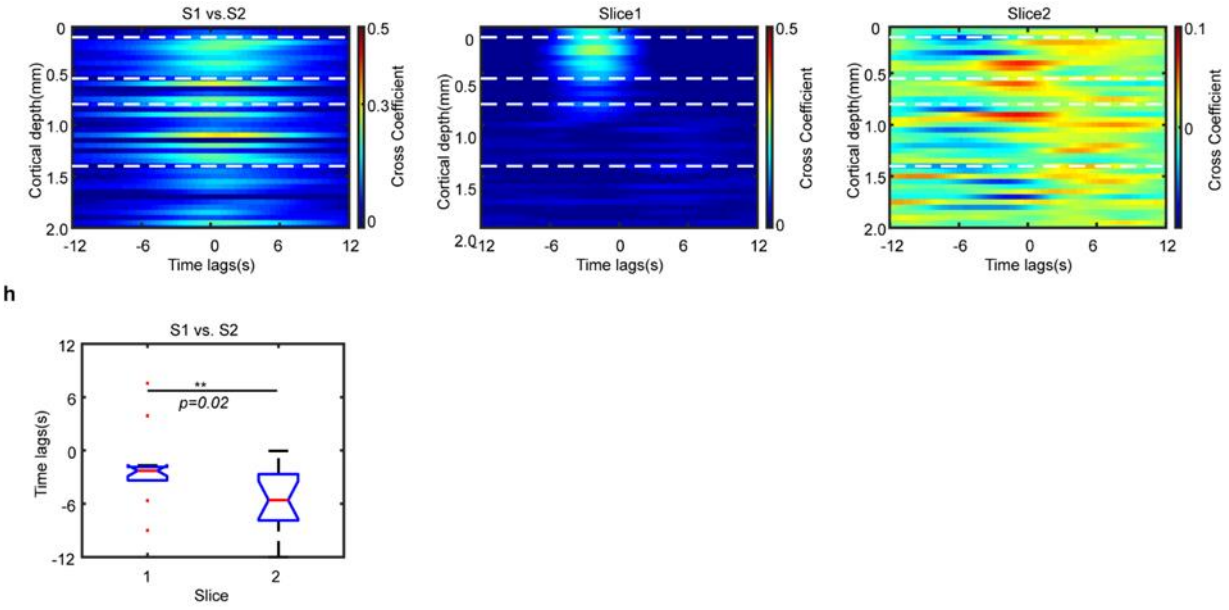

Fig.6 Bilateral line scanning fMRI mapping under unilateral stimulation in Slice1. (a) Experimental design and BOLD responses at unilateral side in Slice1. *Top row:* only stim1 was given electrical stimulus; *bottom row:* 3D-EPI BOLD fMRI map overlaid on anatomical image showing BOLD responses on FP-S1 at 'Slice1' hemisphere. (b) A representative trail showing raw and filtered (0.01-0.1Hz) BOLD line profile time courses. (c) Coherence analysis of the BOLD line profiles between the two slices, grey lines are the individual trails and red line is the mean (3 rats, n=15 trails). (d) Linear correlation of BOLD signals from the two slices. (e) Cross-correlation analysis of BOLD fMRI signals from the two slices. (f-g) *Top row:* Cross-correlation coefficient between the calcium power (1-5Hz) and line profiles across the different trails between the two slices, grey lines are the individual trials, read line is mean, red/dark circle is the lag time at maximum cross-coefficient (3 rats, n=15 trails). *Bottom row:* averaged cross-correlation analysis between the calcium power (1-5Hz) and BOLD line profiles along the 2-mm cortical depth within the bilateral slices, white lines are the layer1-6 (3 rats, n=15 trails). (h) Statistical analysis of the lag time at maximum cross-coefficient value between the two slices (two-sample t-test, 3 rats, n=15 trails, boxplot: central red line is the median, interquartile range 25th and 75th percentiles denotes the maximum and minimum, Slice1: -2.28s, Slice2: -5.58s, outliers are showed by red dots, **p<0.05).

2.2.4 Discussion

We have developed the bilateral line-scanning fMRI with calcium recording system to map the bi-hemispheric neurovascular coupling features at a column level. Along the cortical layers in FP-S1 regions, earlier calcium events were found in bilateral, resting-state as well as ipsilateral imaging modalities, which are consistent with our previous findings performed on one hemisphere of rat brain. For instance, the calcium showed 1.38s and 1.68s earlier responses than bi-hemispheric BOLD signals along the cortical depth upon bilateral sensory stimulations. While, in resting-state, the calcium events still showed earlier fluctuations (1.86s and 0.42s) than the bilateral BOLD signals, but displayed much more sparser and trail-to-trial variations (Fig.4b). Furthermore, the temporal coupling features between the contralateral BOLD and calcium signals were different and showed negative cross-correlations along the cortical depth upon unilateral sensory stimulations (Fig.5-6). Thereby, this multimodal fMRI platform allowed us to disentangle the layer-specific neurovascular coupling features bi-hemispherically under different stimulation paradigms.

Bilateral symmetry of the two hemispheres, in particular, the cortical-to-cortical connections have been fully investigated on human and animal models[143, 146, 147]. However, the paralleled symmetry across the cortical hemisphere and the layer-specific neuronal origins underpinning BOLD signals are still ambiguous. In our experiments, the observation of earlier calcium events as compared to the bi-hemispherical BOLD signals upon bilateral sensory stimulations or resting-state conditions indicate the neuronal driven hemodynamic fluctuations along the cortical depth. Furthermore, the coherent and cross-correlation analyses across the bilateral BOLD line profiles, particularly under resting-state, revealed the symmetrical hemodynamic patterns, which is consistent with the previous reports[143, 149]. It has become clear to us that the corpus callosum plays, at least partially, an important role in mediating the bi-hemispherical neuronal fluctuations through the acallosal animal models[149, 150]. However, bilateral symmetry is also found in humans born without a corpus callosum, indicating that bi-hemispherical activities were not solely sustained and mediated by corpus callosum, instead may possibly by other brain structures as well[151]. This may be the reasons for the sparse and diverse cross-correlation

patterns between the calcium fluctuations and bilateral BOLD signals under resting-state (Fig.4b). The bilateral sensory stimuli paradigms on the rat FP-S1 showed well match of calcium and BOLD signals. However, it still needs further demonstrations in acallosal animal models, to explore if and to what extent the bilateral BOLD responses can be modulated and involved in the contralateral neuronal signals. Previous electrophysiology and resting-state fMRI studies conducted on rat brain have reported involvement of multi-neural pathways for the layer-specific interhemispheric functional connectivity[143]. However, the multi-neural projections to the bi-hemispheric cortical areas that underlying laminar-specific hemodynamic discrepancy is still unclear. We would like to investigate to how the bi-hemispheric BOLD signals can be modulated by the contralateral cortical neuronal activations. Therefore, we were also curious about how the neuronal activities propagate across layers interhemispherically and if these events affect the BOLD signals that lead temporal heterogeneity across cortical-cortical regions in the two hemispheres.

To investigate the interhemispheric propagations that underpins neurovascular-coupling features between the contralateral BOLD and calcium signals along the cortical layers, unilateral sensory stimulus imaging paradigms were conducted. We acquired bilateral BOLD and unihemispheric calcium signals either under contralateral or ipsilateral-evoked conditions *via* the unilateral sensory stimuli modalities (Fig.5-6). The coherent and cross-/correlation analyses showed well arrangement in bi-hemispherical connections of BOLD signals across the cortical layers (Fig.5e & Fig.6e). However, the neurovascular coupling features between BOLD and calcium signals (from the opposite hemisphere) were distinct. For instance, in one imaging modalities, the evoked BOLD responses in Slice2 negatively cross-correlated with the calcium signals from the contralateral cortical side, showing earlier responses of BOLD than the calcium signals (Fig.5g). While, in other modality, the evoked calcium signals in Slice1 negatively cross-correlated with the contralateral BOLD fluctuations (Slice2), showing earlier calcium events (Fig.6g). Despite the different unilateral stimulus paradigms, the ipsilateral calcium fluctuations showed earlier behavior than ipsilateral BOLD signals along the cortical depth in both imaging modalities (Fig.5f & Fig.6f). Previous studies have shown non-linear neurovascular coupling features under unilateral optogenetic stimulations[152, 153]. Our results, i.e., negative cross-correlation patterns between BOLD and calcium signals (from the

opposite hemisphere), further support this phenomenon. One possible explanation maybe that the electrical stimuli currents, in the present experiments, delivered to one hemisphere activate the transcallosal inhibitory circuits, which suppress the hemodynamic and neuronal fluctuations in the contralateral hemisphere[148, 153, 154]. Other potential explanations may account for the multi-origins of upwards stream projections, which suppress cortical activities in the opposite hemisphere. For instance, the thalamocortical (TC) projections to rodent FP-S1 regions mainly arrive at layer 4, which not only activate the intratelencephalic neurons, but also the interneurons as well[155, 156]. Notably, the excitations of these interneurons can produce fast and powerful feedforward inhibition across the cortical layers[155-157]. Furthermore, this inhibitory events precedent slightly delay after the excitations[155, 156], which present an excitation/inhibition balance across multiple layers.

In summary, by taking advantage of this multimodal fMRI platform, we monitored the bi-hemispheric layer-specific hemodynamic responses under different stimulation paradigms. Simultaneously, calcium indicators (GCaMP6f) specifically targeting neuronal populations in the FP-S1 in one hemisphere were recorded. The neurovascular coupling features between calcium and BOLD signals along the cortical layers were consistent with our previous published reports, i.e., the calcium displayed an earlier (~5s) event than hemodynamics under evoked and resting-state conditions[126]. Furthermore, the bi-hemispheric neurovascular couplings were also investigated at laminar level under unilateral stimulation imaging schemes. The contralateral BOLD and calcium signals showed non-linear coupling features, particularity, the evoked BOLD signals from one hemisphere showed earlier temporal features than the calcium signals from the opposite hemisphere. This interhemispheric temporal heterogeneity between BOLD and calcium signals along the cortical layers need future studies to validate. Possibly by applying bi-hemispheric fiber-based calcium recording in combination with bilateral line scanning fMRI on acallosal models with sensory or optogenetic stimulation.

3. Chapter II: Awake mouse fMRI and pupillary recordings in ultrahigh magnetic field

3.1 Introduction

Awake functional magnetic resonance imaging (fMRI) on animal models have been arising since late 1990s [106]. In the past two decades, numerous biological techniques (e.g. optogenetics, transgenic and pharmacological manipulations, etc.) have been implemented, which brought the animal fMRI studies in molecular and behavioral level [39, 48, 158]. However, it remains challenging to interpret the fMRI signals properly as that in anesthetized conditions. This is unfortunate because animal stress and motion artifacts were inevitable during imaging. To minimize these confounding effects, various habituation protocols and restraint systems have been introduced. This is by far most effective procedure in preforming fMRI on conscious animals. In addition, to achieve a better MRI shimming and secure the animals into MRI apparatus, short-period interval anesthesia were still applied in many imaging modalities (Table.S1). Despite clearance after a certain time, the global long-lasting effects and neurotoxicity to neuronal/non-neuronal cells were still unknown [44, 159, 160]. It is therefore of absolutely crucial that completely anesthetic-free awake animal fMRI platform is needed.

With ever-growing exploration of awake animal fMRI, 3D printed and customized restraint apparatus as well as graded training procedures were designed for circumventing the confounding effects (animal stress and motion artifacts). Generally, all imaging protocols started with some forms of consecutive and intensive training prior to imaging. Of note, those training periods varied among laboratories, ranging from 10 mins at the very beginning to 60-90 mins at the final step for continually 7-10 days (Table.S1). Despite heart/respiration rate, blood pressure and plasma corticosterone were monitored to assess the stress level and motions, such an intensive repetitive training/imaging modalities may cause chronic stress and pain that potentially lead to an overall depressed state or a state of helpless [161-163]. It became clear that the existence of restraint effects among the acclimated animals cannot be completely wiped out. Instead, minimizing and attenuating the effects as much as possible even below the tolerable level matters. Therefore, researchers suggested that intermittent training sessions might minimize the

long-lasting chronic restraint effects during acclimation and imaging modalities [161]. This is particularly useful when complex cognition tasks or behaviors are involved.

Compared with the other imaging paradigms, the awake mouse fMRI, not only provides new translatable methods for investigating behavioral, environmental, genetic and pharmacological manipulations on emotional and cognitive processes, but also facilitates the results to pre-clinical applications with the availability of various disease models. For instance, T. Tsurugizawa et al. [44] preformed awake mouse fMRI on a model of autism, figuring out dysfunction/anomalies in white matter and validating possible pharmacological treatments for behavior rescue. Additionally, N. Takata et al. [164] applied optogenetic fMRI on different transgenic mouse lines to study the astrocyte dynamic features. Furthermore, many labs were also trying to link behaviors to brain dynamics in awake fMRI studies. For instance, pupillometry, a non-invasive measurement, indexing the alteration of arousal [165], vigilance [166], emotion [167] and cortical states [168], has been implemented into fMRI on humans as well as animals [133, 169-171]. The pupil size has been linked to track brain state changes. Therefore, bearing these in mind, we propose that the real-time fMRI with pupillary recording of the awake animals should provide us a more robust brain dynamics and physiological state after repetitive exposure to the restrain system in the current training and imaging modalities, opening a new avenue for our further neuroimaging researches.

In the present study, we aim to establish a concurrent fMRI-pupillometry platform on awake mouse (without any anesthesia) at an ultrahigh magnetic field (14.1T). A graded intermittent training protocol was designed to acclimate the mice, which showed good habitual performance and allowed longitudinal studies in the same animal. Furthermore, the pupil dynamics were measured during scanning. In addition, blood oxygen level dependent (BOLD) responses under visual stimulation confirmed the success and reliability of this platform. Overall, in the current study, an awake mouse fMRI-pupillometry platform and an intermittent restraint system without any anesthetics were established. Then, two functional imaging paradigms: light-driven visual stimulus fMRI and resting-state fMRI were conducted. Consequently, the BOLD fMRI under visual stimulation and real-time pupil dynamics under iso-/luminant conditions were assessed.

3.2 Materials and Methods

Animals

All experimental procedures were approved by the state authority (Regierungspräsidium, Tübingen, and BadenWürttemberg, Germany) and conducted in accordance with the guidelines. Nine male C57BL/6 mice (Charles River Laboratory) were employed in this project and two were excluded due to the headpost cracking in later imaging. The animals were habituated individually at a 12hr-2hr light-dark cycle (light on from 8 a.m. to 8 p.m.) with food and water *ad libitum*, starting at age 10-15 weeks.

Behavioral Handling and Training

The 3D printed headpost and customized training boxes [172] have been designed for acclimating the animals (Fig.S1). Briefly, intermittent habitual procedures were applied to the animals for 5-8 weeks before the real fMRI experiments. The acclimation included the following: 1) quietly settled in a comfortable, natural posture in the training box; 2) immobilized with headpost in the training box; 3) exposure to the loud noise in the real 14.1T scanner; 4) slow fluctuations of pupil dynamic; 5) less/no urination or defecation (fecal boli <10) during imaging/training. Only mice that show good performance (mostly quiet, little urination or defecation, slow pupil dynamics) will continue with next phase for imaging.

The mice were acclimatized to handling gradually for 5 days by letting them sit in experimenter's gloved hands for approximately 5 mins/section until they exhibit grooming behaviors, indicating they are comfortable being handled. The training period increases by 10-15 mins/day from 10 mins at the beginning until 60 mins at the maximum. Mice body posture and movements were monitored as an indication of comfort in the restraint system. A video camera with infra light was used to continuously monitor the animals during acclimation (Video.9-10). Mice were first acclimated in the training box without head fixation (~2 weeks) in the scanner and, during later times, intermittent (rest 1-2 days per training session) head fixed in the MRI scanner for at least 5 weeks prior to actual MRI experiment (Video.1). Scanner noises are identical to the precise imaging protocols to which mice would later be exposed during the imaging modalities. Animals receive

sucrose water several times between each training sections (Video.2). After finishing the last training section, animals were retrieved and imaged in the 14.1T MRI scanner within 24 hours.

Headpost Implantation

Mice were firstly anesthetized by isoflurane (2% for induction; 1-1.3% for surgery in a mixture of 30% oxygen in air). The depth of anesthesia was checked by the lack of pedal withdrawal to a firmly pinched hind toe or foot, or the lack of head movement to a firmly pinched ear. Temperature was maintained at 37˚C using a controlled heating pad. A small amount of ophthalmic ointment was placed in each eye to protect from drying.

Then, the mouse was secured to a stereotaxic frame by two earpieces and a bite bar. The skull was shaved and disinfected and, then the surface was exposed. After exposing the skull, the soft tissue and periosteum were carefully removed and cleared with Kerr Gel Etchant (37.5% phosphoric acid, OptiBondTM FL) for 15s. Then, the skull surface for implantation were prepared following the procedures as suggested by the manufacturer (OptiBondTM FL). We applied the dental cement (Charisma flow) to attach the headpost onto the skull. The remaining incision area were sutured and disinfected with antiseptic liquid. Painkillers and antibiotics were administered to relieve pain and inflammation immediately after finishing the surgery. Animals were maintained on a heated blanket until full consciousness restored (15-30 mins) and placed back in their original cages. Post-surgical observations were made and documented for a minimum of five consecutive days following the surgery (twice a day for five days and then daily). The wounds were monitored daily in the first week after surgery to ensure that there was no infection, and that sutures have not come undone (Video.3).

Visual stimulus paradigms and Pupil diameter recording

To investigate BOLD responses under visual stimulations in the awake state. A customized LED light Matrix System (P160104 LED matrix, 470nm) for visual stimulus (Video.4) was triggered by the scanner and controlled with the system (Master-9, A.M.P.I). A block design paradigm of 4s-on-16s-off in 10 epochs for each imaging session was conducted. The light brightness (~6 μW) and flickering frequency (~5Hz) were also

controlled within the system. To monitor the chest movement, a pressure sensor (Graseby Sensor, Medicare Health & Living Ltd) was attached under the animals' abdomen and a tube running from it was connected to the BIOPAC acquisition system (Biopac Systems Inc., USA).

Customized and copper-sealed MRI-compatible cameras (RS-OV7949-1818, Conrad Electronic SE) were applied for monitoring body movements and acquiring pupillometry videos during imaging (32 bites/pixel, 60 frames/s, and resolution: 1920×1080). The camera was held on an adjustable holder made by our mechanical workshop (Fig.S2). A movable infrared LED light (850nm) was additionally positioned aside to left eye of the animal for better pupil recording contrast.

Magnetic resonance imaging

All fMRI imaging modalities were performed in our Bruker Avance III System (Bruker BioSpin, Ettlingen, Germany) with a 14.1-T superconducting magnet with 12cm diameter gradient providing 100G/cm with 150μs rise time. A custom-made transceiver surface coil (8mm in diameter) covering the whole-brain was applied for imaging. Functional scans were acquired using a 2D echo planar imaging (EPI) sequence, with the following parameters: 1s TR, 8ms TE, 12×12mm FOV, 40×40 acquisition matrix, 24 slices, $0.3\times0.3\times0.5mm^3$ resolution, 210 TRs total time. The anatomical RARE (rapid acquisition with relaxation enhancement sequence) images were acquired with exactly the same geometry placements as the functional scans within each session for the following parameters: 2.5s TR, 7ms TE, 12×12mm FOV, 96×96 acquisition matrix, 24 slices, $0.125mm^2$ in-plane resolution, 0.5mm slice thickness, 6× RARE factor, 4× Repetition. Magnetic field homogeneity was corrected using FASTMAP scout. B_0 field homogeneity in the whole brain is a key factor to ensure the image quality and BOLD fMRI signals acquisition. A long-term (>3 months acclimation, quiet, less motions) well-trained mouse was applied at the beginning of each fMRI session to adjust the magnetic homogeneity as well as for references of positioning later-imaging animals on the MRI apparatus. The whole shimming and position adjustment took ~17mins.

Data preprocessing and analyzing

All fMRI data were analyzed using the AFNI software package (Analysis of Functional NeruoImage, https://afni.nimh.nih.gov/)[173]. The preprocessing steps including: 1) motion correction (3dvolreg), 2) co-registration to the anatomical images (align_epi_anat.py), 3) wrap out of non-brain tissue from anatomical/functional data (3dSkullStrip, using a brain mask), 4) spatial smoothing (3dmerge, using a Gaussian kernel of FWHM= 0.2mm), 5) whole brain intensity normalization. 6) Finally, voxel-wise calculated BOLD statistical maps were produced with a generalized linear model (GLM) by applying AFNI's 3dDeconvolve. This final step involved in utilizing a hemodynamic response function (HRF) model: BLOCK (d, p), which convolved with a square wave of duration d and made a peak amplitude of p (the amplitude of basis function and usually set to 1). The HRF model is defined as follows:

$$HRF(t) = int(g(t-s), s = 0..\min(t, d))$$

where g(t) =$g(t) = t^q e^{-t}/[q^q e^{-q}]$, q = 4, d is the square wave of duration.

The activated ROIs, based on previous reports [174, 175], within the functional maps were extracted and detrend for baseline shift. The baseline signal of EPI images were normalized to 100 for later multiple trial statistical analysis. To characterize the signal changes, custom-written MATLAB (MathWorks, Natick, USA) scripts were used to average the BOLD signal time-series from each epoch and converted to percentage change by subtracting and dividing each time-series by the average of 6 TRs prior to stimulus. The anatomical MRI images were registered to a template across animals for later image processing by applying the 3dAllineate function.

For pupil data (PD) preprocessing, all the pupillometry videos were cropped and processed using the DeepLabCut toolbox [176]. A mouse pupil network was built in this project for extracting the pupil size from each individual video (Video.5-6). The network was generated by using 5670 frames from 27 videos (5 mice). Through this specially built network, the upper/lower and left/right of the pupil boundaries were labeled for calculating the pupil diameter. The pupil diameter was calculated based on the algorithm [133]:

$$diameter = \frac{1}{2} \times (\sqrt{(x2 - x1)^2 + (y2 - y1)^2} + \sqrt{(x4 - x3)^2 + (y4 - y3)^2})$$

3.3 Results

Establishment of concurrent fMRI-pupillometry platform

The schematic of the fMRI-pupillometry platform and acclimation procedures for awake mice imaging are shown in Fig.1. The intermittent habitual protocol was gradually applied to train the animals (Fig.1a). Different from previous 'mock scanner' restraining system, the animals in the current experiments underwent a gradual intermittent exposure to the real scanner noise as well as to restraint system (Fig.S1). Of note, the animals normally took 1-2 days rest after each training session, which prolonged the overall training period up to 5-8 weeks. In addition, no anesthetics were applied during the entire acclimation and imaging modalities. After 5-8 weeks training, the animals got accustomed to the restraint system and showed an inclination to keep an 'imaging posture' even without head fixation compared with the less well-trained animals (Video.7-10). The chest movements also showed less motion spikes, indicating a quiet/calm state after training (Fig.S3).

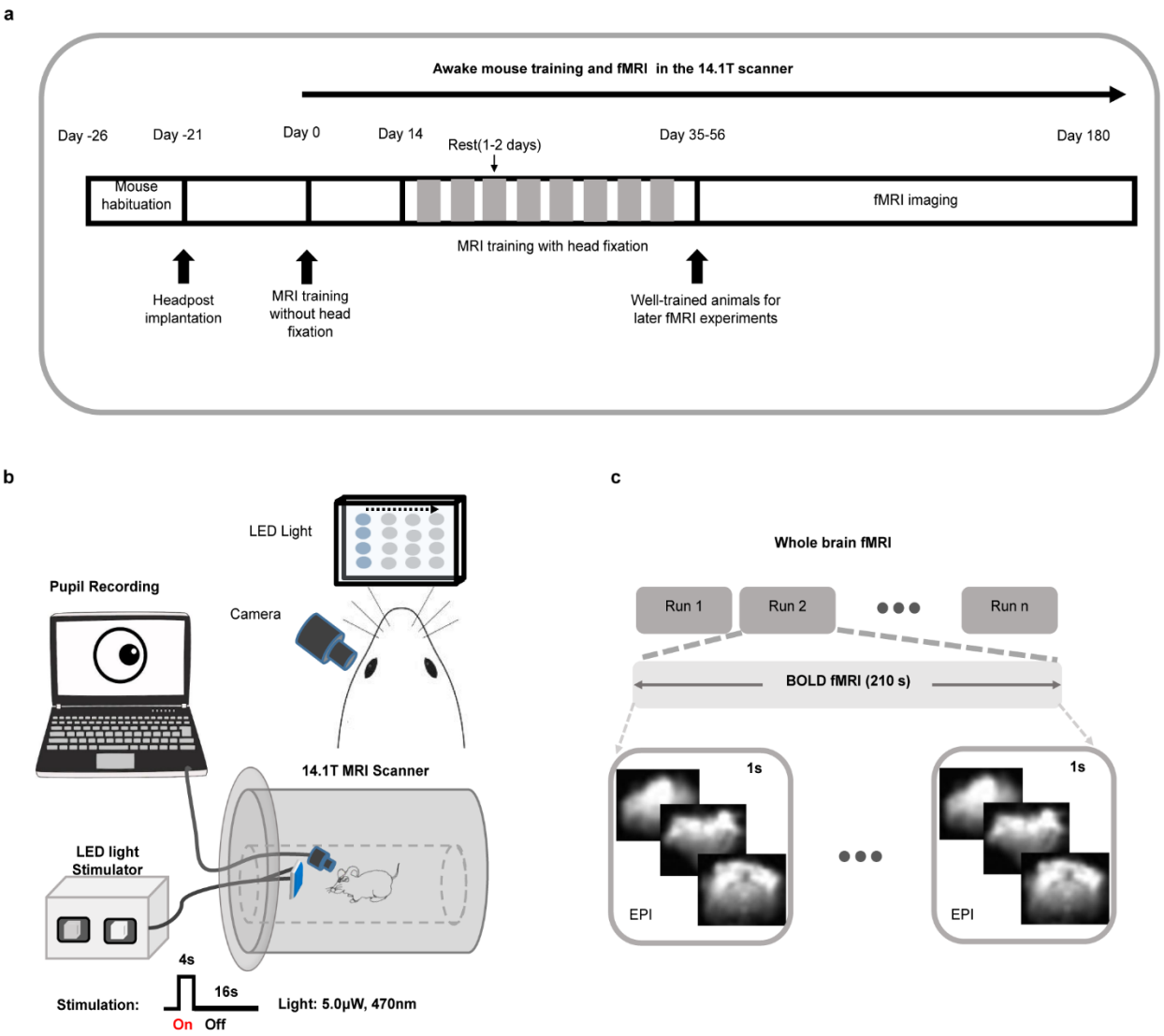

Fig.1. Awake fMRI-pupillometry setups and imaging modalities. (a) Schedule of the intermittent restraint protocol. (b) Schematics of visual stimulation paradigms and pupil recordings. (c) Designs of whole-brain fMRI modalities.

An infrared camera with copper shielding and blue LED light matrix were implemented to record the pupil diameter and deliver visual stimulation, respectively (Fig.1b, Video.4-6 & Fig.S2). The light intensity (0-6μW) and moving frequency (0-10Hz) were adjustable during imaging sessions. Whole-brain fMRI paradigms were designed under visual stimulus as well as resting-state (Fig.1c). Importantly, shimming and filed homogeneity determine the quality of signals in awake fMRI experiments. Therefore, one mouse (showing good performance) was scanned every time prior to imaging for ameliorating

shimming and adjusting the camera's angle/focus in optimum for later animal scanning.

Head motion assessment

Head motion assessment was calculated and compared after different periods of training sessions (1st, 5th and 8th week). As showed in Fig.2, six motion parameters (three translation displacements AP, RL, IS and three rotational displacements of roll, pitch, and yaw) were calculated during the acclimation. The rotation and movement time courses were gathered from six mice. The average time courses of translation and rotation displacements corresponding to the 1st, 5th and 8th week are shown in Fig.2a (A-P, 0.04±0.03 vs. 0.01±0.01 vs. 0.003±0.002mm; I-S, 0.04±0.03 vs. 0.01±0.01 vs. 0.01±0.009mm; R-L, 0.003±0.002 vs. 0.002±0.002 vs. 0.002±0.001mm; Pitch, 0.27± 0.22 vs. 0.11±0.09 vs. 0.14±0.08degree; Yaw, 0.08±0.05 vs. 0.05±0.04 vs. 0.02±0.01degree; Roll, 0.05±0.05 vs. 0.03±0.02 vs. 0.03±0.02degree; mean±SD). The variance of those motion parameters from each individual trial were extracted and compared (Fig.2b, one-way ANOVA, A-P, F(2, 47)=3.26, P=0.047; I-S, F(2, 47)=6.94, P=0.002; R-L, F(2, 47)=2.36, P=0.106; Pitch, F(2, 47)=8.63, P=0.0006; Yaw, F(2, 47)=5.64, P=0.006; Roll, F(2, 47)=2.6, P=0.085). Head motions were substantially reduced along all planes following the acclimation protocol. *Bonferroni* post-hoc test was performed to specify the group difference.

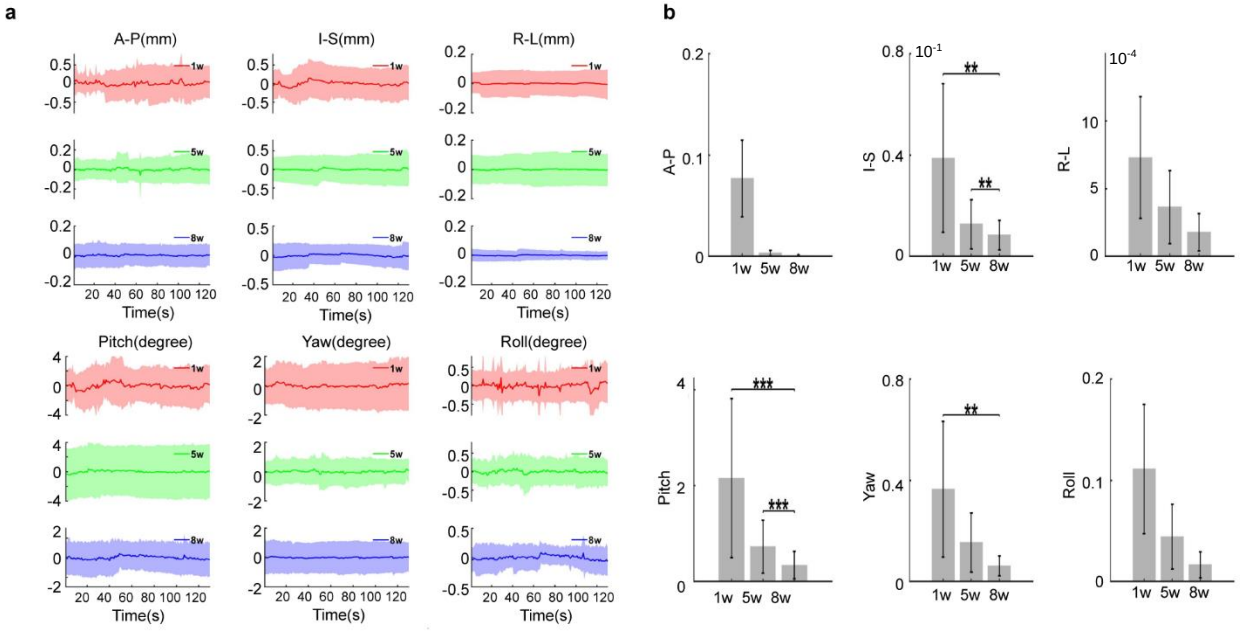

Fig.2. The estimated motion parameters during intermittent acclimation from different weeks. (a) Averaged time course of translation displacement (A-P: anterior-posterior; I-S: inferior-superior; R-L: right-left) and rotations (pitch, yaw and roll) after different weeks of training (first, fifth, eighth week), six mice, shaded regions: mean±S.D. (b) Variance of translation and rotation time course, ** $p < 0.01$, *** $p < 0.001$ by Bonferroni post-hoc test, error bars, S.E.M.

BOLD responses under moving light visual stimulation.

To confirm the fidelity of this platform, BOLD fMRI signals were acquired under visual simulation. Three main regions of the visual pathway showed significant positive BOLD activation ($p<0.001$): the visual cortex (VC), superior colliculus (SC) and dorsal lateral geniculate nucleus (LGd) (Fig.3a). The three regions showed similar patterns upon stimulus with slightly variations across different imaging sessions. Averaged time courses of BOLD signal changes of the three regions from different animals (VC, SC and LGd) showed a maximum of 0.72%, 2.5% and 0.5%, respectively (Fig.3b). Similar to previous fMRI studies, these responses were robust and reliable in all of the current imaging modules [46, 174].

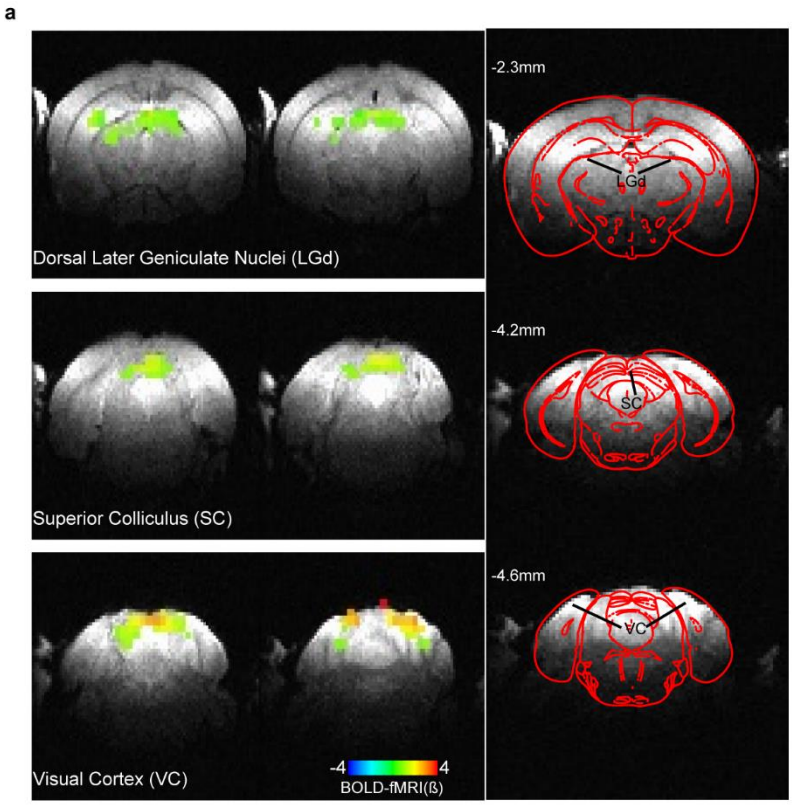

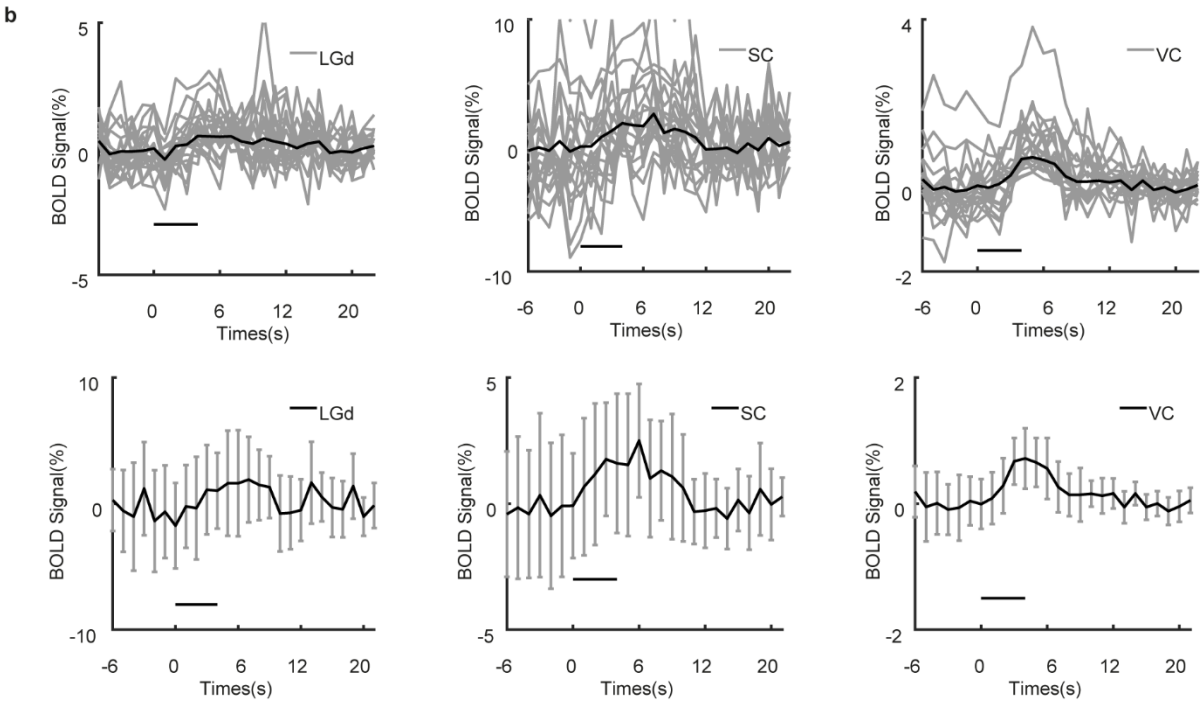

Fig.3. The BOLD response under visual stimulus. (a) Representative color-coded BOLD-fMRI maps overlaid on anatomical images, showing visual cortex (VC), superior colliculus (SC) and dorsal lateral geniculate nucleus (LGd) activations in visual circuit-related regions ($p<0.001$). (b) Averaged BOLD signals changes upon visual stimulations in the visual circuit-related regions, top row: the individual epoch of signal changes from all the animals, bottom row: the mean BOLD signal changes (6 mice, ~94 trails, Error bars, mean±S.D, horizontal bars, duration of light stimulation).

3.4 Discussion

We have successfully customized an intermittent acclimated protocol free of any anesthesia and restraint system for concurrent fMRI-pupillometry on awake mouse. Thus, making it possible to map the large-scale brain dynamics that were linked to behaviors, cognition processing and information perception. The circuit-related visual brain regions (VC, SC and LGd) displaced BOLD response upon the light stimulation, which are in line with previous published reports [46, 174, 175, 177]. Furthermore, PD was simultaneously recorded for monitoring the animal movements and stress assessment, validating a reliable proxy in awake imaging at ultrahigh magnetic field. To summarize, we have established an awake mouse pupillometry-fMRI platform and successfully performed two imaging modalities, i.e., the light-driven visual stimulus fMRI and resting-state fMRI. This platform opens up numerous subsequent studies such as, how behavior is organized and integrated across multiple brain regions, how genetic and pharmacological manipulations effects on emotional and cognitive processes in the fully conscious brains, etc.

Unlike the previous awake rodent fMRI studies, in this project, intermittent training procedures instead of 7-10 days consecutive training steps were applied to the animals. This intermittent exposure to the restraint system could possibly minimize chronic effects compared with the longer, daily consecutive restraint sessions for the animals [178]. Furthermore, our acclimation procedures did not apply any anesthetics during fMRI acquisition for head/body immobilization and position. Thus, making it completely free from confounds of anesthesia and rendering a higher potential for human translation. Though, numerous previous studies implicated that light anesthesia may preserve the brain dynamic patterns in rodents [44, 179], it remains controversial whether the global brain fluctuations can be affected. Some researchers even claimed that low dosage inhalation of the isoflurane can be shortly cleared after cessation of administration [180]. Therefore, many labs still applied a short interval anesthesia for fixating and positioning the animals as well as shimming adjustment before fMRI scanning (Table.S1). However, it is still challenging to specify the residual effects [110], since the administrated volumes and time varied across laboratories. Contrast to the previous studies, the current intermittent habitual acclimatization without any anesthetics, though lasting 5-8 weeks, can also

achieve the goal for awake imaging, during which the animals did not undergo a daily consecutive time-intensive training procedures.

Similar to many previous awake fMRI protocols, restraint apparatus and acclimating procedures were designed to minimize the head motion and artifacts. However, many labs have attempted to design a bite bar, earplugs and plastic neck covering pieces, etc., to firmly immobilize the animals into the magnetic bore (Table.S1). All these customized designs could also result in extra stress, which in turn increases the animals' escape attempts or helplessness. Furthermore, in some extreme cases, the escape attempts could loosen the headpost (headpieces) or even crack the skull, introducing severe image distortions or completely failures regardless of how long or how well the animals had been trained. In several earlier awake rodent fMRI studies, researchers even applied a long tube/cradle or jacket to fit the animals for controlling the body movements (Table.S1). These made it impractical for studying cognitive or behavioral tasks. The main advantage of our restraint apparatus is simplicity/flexibility as well as the open space without any other forms of constraints expect for the head immobilization.

The pupil behavior is a reliable marker for characterizing brain state and reflecting the ANS (autonomic nervous system) activities [165, 168, 170]. Previous studies have reported that pupil dilation is modulated through sympathetic system as a consequence of various cognitive operations, e.g., memory maintenance, mental effort, and physiological stress, etc. [181-183]. While, pupil constrictions were controlled by the parasympathetic system [184]. In particular, the pupil naturally returns to its previous state after dilation/constriction. Therefore, based on this phenomenon, we recorded the real-time pupil dynamics for assessing the animal motion and stress. In the present studies, pupillary data were acquired simultaneously with fMRI under (iso-) illuminant conditions as a function of time. Unlike other biomarkers (e.g., blood pressure, heart/breath rate, and corticosterone level etc.), we simply look at the pupil dynamics while imaging in the scanner and indexed it as an indicator for motion and stress assessment. This gains greater benefits to translational studies, as the PD acquisition is non-invasive and no need for physical contact.

To verify the fidelity of the current awake fMRI model, we implemented the visual stimulations for detecting BOLD responses. Consistent with the many published reports,

BOLD activation maps overlaid in the visual pathway-related areas [46, 174]. However, the flickering light stimulus paradigms instead of the conventional flashing light stimulus were applied in the project, making it complicated to interpret the activation patterns in different brain regions. Previous studies have reported the mouse visual system not only decodes the external visual information flow, but also selectively transmits the specific visual features to different brain regions. Furthermore, some neurons are sensitive to the velocity and direction, exhibiting inhibitory/excitatory effects with regard to the moving visual stimulus [185, 186]. This further explains the negative or non-visual related BOLD responses upon exposure to the flickering light stimulations in some of the imaging trails (data not shown).

Conclusion

In summary, we report here a successful awake mouse fMRI protocol with pupillary measurement undergoing an intermittent restraint system without any anesthetics. We conducted two awake imaging paradigms: light-driven visual stimulus fMRI and resting-state fMRI. In line with the previous studies, the visual-related brain nuclei were activated upon visual stimulations. Furthermore, concurrent pupillometry were recorded while the animals were being imaged, providing a real-time assessment of the motion and stress level control for our data acquisition. To conclude, the current awake mouse fMRI platform prepared us for ongoing and future translational studies, such as cognition processing or pre-clinical pharmacological therapies on disease models.

Limitations

The intermittent restraint protocol extending as long as 5-8 weeks in the current image modalities, which was a little bit time consuming compared with most of the current awake rodent fMRI studies (Table.S1). However, it was worth to train the animals to be gradually familiar with the external environment, especially when combined with complex behavioral related tasks in future studies, such as sensory discriminations or reward/punishment processing. Another caveat is that the animal stress levels were not fully quantified during acclimation and imaging. The serum corticosterone, an indicator of stress levels, may provide further index for stress level dynamics [44, 163], which in turn can precisely guide the experimenters to adjust the acclimation procedures step-by-step in

further studies. However, repetitive blood sampling from the same animal remains a concern, due to the small circulating blood volume. While, from the behavioral perspective, the animals did show a relief of motion and stress in the current protocol. For instance, the mouse behaved quite differently inside/outside scanner (Video.7-10). In addition, the pupil fluctuated very fast at the very beginning with head-fixed under noise conditions, which disappeared after following intermittent exposures (Video.11-12).

Instead of flashing light visual stimulus, we applied a moving blue light matrix in the current imaging modalities, making it complicated to interpret the BOLD signals in non-visual related brain regions. In addition, the very close distance (<8mm) between eye and camera, perturbing the light-distributing balance into the two eyes. Furthermore, the mouse visual system consists various neuronal cells that are selectively sensitive to orientation, direction, motions and color [187], which further complicated the possible underlying mechanisms for BOLD activations in current imaging modalities. Therefore, a better visual stimulation paradigm involving light moving frequency, illumination power, moving direction, etc. should be carefully considered in future imaging modalities.

4. Summary

In summary, these projects in this thesis that I had been working during my PhD training for the past four years, not only did they prepare me the critical thinking about biological problems or bio-phenomena for my future academic career, but also drove me bit-by-bit to think about or seek possible solutions. For instance, the chapter I mainly focused on investigating the neurovascular coupling relationships between the cortical layers and calcium signals. We conducted the evoked and resting-state stimulus paradigms in the forepaw regions on anesthetized rats. Either unilateral hemispheric or bilateral hemispheric line-scanning fMRI with calcium recording experiments were performed. However, considering the confounding effects from the anesthetic agents, we were thinking to build an awake animal fMRI model upon finishing the projects in chapter I. In addition, the main reason that drives us to start the awake experiments is that the awake animal fMRI allows us to combine behavioral tasks or cognitions processes, which is not possible under anesthetic brain states. Therefore, in chapter II, we were trying to build an awake mouse fMRI model free from any anesthesia. Furthermore, we implemented the pupillometry and visual stimulus on this awake model. Actually, not only the visual stimulation paradigms, but also many other stimulus modalities, such as odor stimulation, rewarding or discrimination task, etc. can be implemented on this awake model for further studies as well.

In chapter I, my main work was to acquire and analyze the line-scanning fMRI BOLD and calcium signals from the rat forepaw regions under α-chloralose. The rat forepaw regions have been studied thoroughly, which can always show a robust and reliable response upon contralateral paw electrical stimulations [188]. The reason we chose the FP-S1 as the ROI is that the cortical excitatory neurons are 10~15 times more than the inhibitory neurons, which means that the BOLD response will be less contaminated by the inhibitory neuronal activations upon stimulations [95]. Furthermore, the line-scanning fMRI method only needs the frequency-encoding and skips the phase-encoding step, which allows us an unparalleled fast sampling rate. In addition, it also shows less sensitive to the head motions, which provides us the ‘true’ BOLD responses in the images. In parallel, we expressed the genetically encoded calcium indicators for measuring the excitatory

neuronal activities. Ultimately, the BOLD and calcium signals were acquired along the cortical depth within the FP-S1 regions. Correlating the calcium signals with laminar BOLD dynamics allowed us to decipher the relationships between neuronal and hemodynamics in a sub-millimeter or column level. Furthermore, we were not confined in one hemisphere. Subsequently, we extended the multi-slice line-scanning fMRI to bilateral hemisphere, i.e., the bilateral line-scanning fMRI, which allows us to systematically investigate the layer-specific neurovascular couplings bihemispherically under different stimulation paradigms.

In the first part, we developed the multi-slices line-scanning fMRI method based on our previous published reports [33]. Confined within such a short patch of FP-S1, we hypothesized that the cortical BOLD responses are different, as the vascular structures varied along the cortical layers and the laminar projections to downstream or upstream also distinct within each layers [34, 100]. Our results showed the distinct BOLD responses along the cortical depth, with the superficial and middle layers presenting stronger responses than the deep layers that were consistent with previous studies [27, 34]. The neurovascular coupling features between the BOLD and calcium signals were also different along the cortical depth, with the superficial and middle layers showing stronger correlation features. The three slices also showed distinct coupling features in such a short patch of region in FP-S1. Significant difference were found within the three slices in the evoked conditions. However, the neurovascular coupling features were much varied trial-to-trial along the cortical layers in resting-state conditions. Further analysis revealed that the calcium signals leading an earlier of ~5s event than the BOLD responses along the laminae in both evoked and resting-state.

In the second part, we further extended the line-scanning fMRI method to investigate the two hemispheres, covering the left and right FP-S1, namely, bilateral line-scanning fMRI. The functional connectivity between the two hemispheres has long been explored in both evoked and resting-state [146, 148, 189]. Likewise, we also simultaneously recorded the calcium and BOLD signals from the FP-S1 regions. The electrical stimulus pluses were delivered to the left and right forepaw, which provided us the bilateral FP-S1 BOLD responses. Together with the calcium signals, we conducted the similar analysis as

discussed above to investigate the layer-specific coupling features between the BOLD and calcium, particular the contralateral BOLD-calcium. We found similar result in the ipsilateral hemisphere of calcium showing ~5s earlier responses than BOLD. However, the contralateral BOLD-calcium showed negative cross-correlations upon unilateral stimulations, depicting possible multi-origins of neural circuits in modulating the neurovascular couplings along the cortical layers, which needs further explorations

In all, this multi-modal imaging system provided us a detailed spatiotemporal information across the cortical layers. The laminar fMRI has been the major method to investigate the laminae circuit-based pathways, i.e., feedforward or feedback information flows. However, there were several challenges, which obscured our understanding of the interactions about those information flows. For instance, the hemodynamic responses, in particular, under resting-state fluctuated at a finer slow pace compared with the neuronal activities, which made it difficult for us to interpret the underlying signal origins. This motived us to combine the optical-fiber based calcium recording with the line-scanning fMRI method in the current projects. However, it remains uncertain how the specific types of neurons within each layers modulated the hemodynamics. The single fiber photometry system in the current projects limited further investigation of the multi-origins of neural fluctuations that may underlie possible interpretation for the BOLD response. Therefore, further advanced optical-fiber recording system containing multi-channel recordings may help us to better understand the layer-specific neurovascular coupling features. Furthermore, various genetically encoded sensors for in vivo imaging or transgenic animal models should provide us a much more detailed information about the neurovascular coupling features, which can serve as the underlying mechanism for hemodynamic fluctuation origins in future and on-going studies.

In the chapter II, we aimed to build an awake mouse fMRI model without any anesthesia in the ultrahigh filed. Notably, different from the many previous awake rodent fMRI studies, we did not apply any anesthesia during the entire training process, which should guarantee us a ‘true’ brain state for mapping the brain functuntional dynamics for future studies under different stimulus paradigms. Furthermore, the pupillometry system was implemented on this awake model to continuously monitor the pupil dynamics during

imaging. The pupil dynamics has long been used to index the brain state on human as well animal models, e.g. the arousal state, alertness or emotional states[190]. In the current project, we continuously monitored the pupil dynamics following the acclimating procedures in the restraint system, which provided us a real-time control for stress and motion artifacts in our imaging acquisitions. Furthermore, instead of continuously daily training of the animals, we started an intermittent training protocols for the animals, which prolonged the training period, but rewarding for our further experiments. Since the animals were acclimated to the imaging environment gradually and intermittently, there were less stress and motions during imaging as demonstrated by the pupil and animal behaviors (Video.7-12). To test the fidelity of this model, we acquired BOLD responses in the visual-circuit regions by giving visual stimulations in a block design paradigm. The BOLD responses were reliably found in the visual cortex, superior colliculus and dorsal lateral geniculate nucleus, which were consistent with previous studies [41, 46, 191]. Currently, a lot of groups and investigators have gradually focused their research topics on awake animal fMRI projects. The availability of the various tansgenetic mouse models that allow us to investigate the possible pathological mechanisms or abnormal behaviors in disease brain states, which may in turn facilitate the possible treatments or underlying patho-mechanisms for the preclinical applications (Table.S1).

In all, we successfully established an awake mouse fMRI model in the ultrahigh filed and it prepared us on-going and future experiments that involves in behavior, decision making or complicated cognitional task, etc., which should pose a great value for the translational studies to humans. The stress and motion artifacts are the two major awake animal fMRI challenges that cannot be completely eliminated. However, we can optimize the newly developed methods to reduce the motion and stress level as much as possible. Depending on the research purpose and acquisition methods, it is better for us to make a balance between the motion artifacts and restraint procedures in awake fMRI experiments.

5. Statement of contribution:

Chapter I part 1: Concurrent intracellular calcium recordings with laminar fMRI mapping. Dr. Xin Yu designed the experiments and started this research topic. In addition, Dr.Xin Yu has helped to set the EPI and line scanning sequences for data generation. Hang Zeng built the calcium light path system and prepared the animals (virus injections) as well as preformed the experiments for data acquisitions. Dr. Rolf Pohmann provided the initial Matlab functions of extracting the fMRI signals from the raw data. Hang Zeng finished all the data analysis with Qi Wang and Filip Sobczak's comments and suggestions. Furthermore, Qi Wang and Filip Sobczak have discussed and helped to double check the figures or codes that I have made for the thesis writing in this part. Hang Zeng finished the initial writings. Prof. Dr. Sandra Beer-Hammer, Prof. Dr. Cornelius Schwarz and Dr.Xin Yu provided the comments and revised suggestions in writing this chapter.

Chapter I part 2: Bilateral line-scanning fMRI with intracellular calcium recording. Dr. Xin Yu designed the experiments and started this research topic. In addition, Dr.Xin Yu has helped to set the EPI and bilateral line scanning sequences for data generation. Hang Zeng built the calcium light path system and prepared the animals (virus injections) as well as preformed the experiments for data acquisitions. Dr. Rolf Pohmann provided the initial Matlab functions of extracting the fMRI signals from for the raw data. Hang Zeng finished all the data analysis as well as the initial writings. Prof. Dr. Sandra Beer-Hammer, Prof. Dr. Cornelius Schwarz and Dr.Xin Yu provided the comments and revised suggestions in writing this chapter.

Chapter II: **Awake mouse fMRI and pupillary recordings in ultrahigh magnetic field.** Dr. Xin Yu initiated this awake fMRI research topic. Hang Zeng wrote the animal protocol and designed the customized experimental apparatus for awake training in this chapter. Prof. Dr. Cornelius Schwarz's lab provided the supports and trained me of how to perform the headpost surgery on mouse models. Prof. Dr. Sandra Beer-Hammer's lab provided mice as well as surgery training that prepared me for this project. Hang Zeng did surgery and animal training for each animals in this chapter. Hang Zeng finished all the data analysis with suggestions from Filip Sobczak. Hang Zeng finished the initial writings of this

chapter and the literatures searching in the field, which generated the supplementary table. Prof. Dr. Sandra Beer-Hammer, Prof. Dr. Cornelius Schwarz and Dr.Xin Yu provided the comments and revised suggestions in writing this chapter.

6. Reference

1. Roalf DR, Gur RC. Functional brain imaging in neuropsychology over the past 25 years. Neuropsychology 2017;31:954-971.
2. Ogawa S, Lee TM, Nayak AS, Glynn P. Oxygenation-Sensitive Contrast in Magnetic-Resonance Image of Rodent Brain at High Magnetic-Fields. Magnetic Resonance in Medicine 1990;14:68-78.
3. Ogawa S, Tank DW, Menon R, et al. Intrinsic signal changes accompanying sensory stimulation: functional brain mapping with magnetic resonance imaging. Proc Natl Acad Sci U S A 1992;89:5951-5955.
4. Cabeza R, Nyberg L. Imaging Cognition: An Empirical Review of PET Studies with Normal Subjects. J Cogn Neurosci 1997;9:1-26.
5. Mariani G, Bruselli L, Kuwert T, et al. A review on the clinical uses of SPECT/CT. Eur J Nucl Med Mol Imaging 2010;37:1959-1985.
6. Chen WL, Wagner J, Heugel N, et al. Functional Near-Infrared Spectroscopy and Its Clinical Application in the Field of Neuroscience: Advances and Future Directions. Front Neurosci 2020;14:724.
7. Glover GH. Overview of functional magnetic resonance imaging. Neurosurg Clin N Am 2011;22:133-139, vii.
8. Singh SP. Magnetoencephalography: Basic principles. Ann Indian Acad Neurol 2014;17:S107-112.
9. Biasiucci A, Franceschiello B, Murray MM. Electroencephalography. Current Biology 2019;29:R80-R85.
10. Logothetis NK, Pauls J, Augath M, Trinath T, Oeltermann A. Neurophysiological investigation of the basis of the fMRI signal. Nature 2001;412:150-157.
11. Schulz K, Sydekum E, Krueppel R, et al. Simultaneous BOLD fMRI and fiber-optic calcium recording in rat neocortex. Nat Methods 2012;9:597-602.
12. Balaram P, Kaas JH. Towards a unified scheme of cortical lamination for primary visual cortex across primates: insights from NeuN and VGLUT2 immunoreactivity. Front Neuroanat 2014;8:81.
13. Larriva-Sahd J. Cytological organization of the alpha component of the anterior olfactory nucleus and olfactory limbus. Front Neuroanat 2012;6:23.

14. Wagstyl K, Larocque S, Cucurull G, et al. BigBrain 3D atlas of cortical layers: Cortical and laminar thickness gradients diverge in sensory and motor cortices. PLoS Biol 2020;18:e3000678.
15. Felleman DJ, Van Essen DC. Distributed hierarchical processing in the primate cerebral cortex. Cereb Cortex 1991;1:1-47.
16. Silva AC, Koretsky AP. Laminar specificity of functional MRI onset times during somatosensory stimulation in rat. Proc Natl Acad Sci U S A 2002;99:15182-15187.
17. Shipp S. Structure and function of the cerebral cortex. Curr Biol 2007;17:R443-449.
18. Tigges J, Tigges M, Perachio AA. Complementary laminar terminations of afferents to area 17 originating in area 18 and in the lateral geniculate nucleus in squirrel monkey. J Comp Neurol 1977;176:87-100.
19. Hubel DH, Wiesel TN. Laminar and columnar distribution of geniculo-cortical fibers in the macaque monkey. J Comp Neurol 1972;146:421-450.
20. Schroeder CE, Mehta AD, Givre SJ. A spatiotemporal profile of visual system activation revealed by current source density analysis in the awake macaque. Cereb Cortex 1998;8:575-592.
21. Petridou N, Siero JCW. Laminar fMRI: What can the time domain tell us? Neuroimage 2017.
22. Nassi JJ, Cepko CL, Born RT, Beier KT. Neuroanatomy goes viral! Front Neuroanat 2015;9:80.
23. Jones EG. What Are the Local Circuits? Neurobiology of Neocortex 1988.
24. Rockland KS. What do we know about laminar connectivity? Neuroimage 2019;197:772-784.
25. Lodato S, Arlotta P. Generating neuronal diversity in the mammalian cerebral cortex. Annu Rev Cell Dev Biol 2015;31:699-720.
26. Kim SG, Ogawa S. Biophysical and physiological origins of blood oxygenation level-dependent fMRI signals. Journal of Cerebral Blood Flow and Metabolism 2012;32:1188-1206.
27. Duvernoy HM, Delon S, Vannson JL. Cortical blood vessels of the human brain. Brain Res Bull 1981;7:519-579.

28. Kim SG, Harel N, Jin T, Kim T, Lee P, Zhao F. Cerebral blood volume MRI with intravascular superparamagnetic iron oxide nanoparticles. NMR Biomed 2013;26:949-962.
29. Weber B, Keller AL, Reichold J, Logothetis NK. The microvascular system of the striate and extrastriate visual cortex of the macaque. Cereb Cortex 2008;18:2318-2330.
30. Blinder P, Tsai PS, Kaufhold JP, Knutsen PM, Suhl H, Kleinfeld D. The cortical angiome: an interconnected vascular network with noncolumnar patterns of blood flow. Nature Neuroscience 2013;16:889-U150.
31. Baez-Yanez MG, Ehses P, Mirkes C, Tsai PS, Kleinfeld D, Scheffler K. The impact of vessel size, orientation and intravascular contribution on the neurovascular fingerprint of BOLD bSSFP fMRI. Neuroimage 2017;163:13-23.
32. Gagnon L, Sakadzic S, Lesage F, et al. Quantifying the Microvascular Origin of BOLD-fMRI from First Principles with Two-Photon Microscopy and an Oxygen-Sensitive Nanoprobe. Journal of Neuroscience 2015;35:3663-3675.
33. Yu X, Qian C, Chen DY, Dodd SJ, Koretsky AP. Deciphering laminar-specific neural inputs with line-scanning fMRI. Nat Methods 2014;11:55-58.
34. Dumoulin SO. Layers of Neuroscience. Neuron 2017;96:1205-1206.
35. Huber L, Handwerker DA, Jangraw DC, et al. High-Resolution CBV-fMRI Allows Mapping of Laminar Activity and Connectivity of Cortical Input and Output in Human M1. Neuron 2017;96:1253-1263 e1257.
36. Howarth C, Mishra A, Hall CN. More than just summed neuronal activity: how multiple cell types shape the BOLD response. Philosophical Transactions of the Royal Society B-Biological Sciences 2021;376.
37. Shipp S. Structure and function of the cerebral cortex. Current Biology 2007;17:R443-R449.
38. Goense JB, Logothetis NK. Neurophysiology of the BOLD fMRI signal in awake monkeys. Curr Biol 2008;18:631-640.
39. Desai M, Kahn I, Knoblich U, et al. Mapping brain networks in awake mice using combined optical neural control and fMRI. J Neurophysiol 2011;105:1393-1405.

40. De Groof G, Jonckers E, Gunturkun O, Denolf P, Van Auderkerke J, Van der Linden A. Functional MRI and functional connectivity of the visual system of awake pigeons. Behav Brain Res 2013;239:43-50.
41. Ma M, Qian C, Li Y, Zuo Z, Liu Z. Setup and data analysis for functional magnetic resonance imaging of awake cat visual cortex. Neurosci Bull 2013;29:588-602.
42. Berns GS, Brooks AM, Spivak M, Levy K. Functional MRI in Awake Dogs Predicts Suitability for Assistance Work. Sci Rep 2017;7:43704.
43. Chen PC, Shoa KH, Jao JC, Hsiao CC. Dynamic magnetic resonance imaging of carbogen challenge on awake rabbit brain at 1.5T. J Xray Sci Technol 2018;26:997-1009.
44. Tsurugizawa T, Tamada K, Ono N, et al. Awake functional MRI detects neural circuit dysfunction in a mouse model of autism. Sci Adv 2020;6:eaav4520.
45. Wang M, He Y, Sejnowski TJ, Yu X. Brain-state dependent astrocytic Ca(2+) signals are coupled to both positive and negative BOLD-fMRI signals. Proc Natl Acad Sci U S A 2018;115:E1647-E1656.
46. Niranjan A, Christie IN, Solomon SG, Wells JA, Lythgoe MF. fMRI mapping of the visual system in the mouse brain with interleaved snapshot GE-EPI. Neuroimage 2016;139:337-345.
47. Han Z, Chen W, Chen X, et al. Awake and behaving mouse fMRI during Go/No-Go task. Neuroimage 2019;188:733-742.
48. Behroozi M, Helluy X, Strockens F, et al. Event-related functional MRI of awake behaving pigeons at 7T. Nat Commun 2020;11:4715.
49. Castelvecchi D. Just a moment. Nature Physics 2020;16:994-994.
50. Rabi, II, Zacharias JR, Millman S, Kusch P. Milestones in magnetic resonance: 'a new method of measuring nuclear magnetic moment' . 1938. J Magn Reson Imaging 1992;2:131-133.
51. Pound RV, Purcell EM. Measurement of Magnetic Resonance Absorption by Nuclear Moments in a Solid. Physical Review 1946;69:681-681.
52. Bloch F, Hansen WW, Packard M. Nuclear Induction. Physical Review 1946;69:680-680.
53. Lauterbur PC. Image formation by induced local interactions. Examples employing nuclear magnetic resonance. 1973. Clin Orthop Relat Res 1973:3-6.

54. Mansfield P. Multi-Planar Image-Formation Using Nmr Spin Echoes. Journal of Physics C-Solid State Physics 1977;10:L55-L58.
55. Shorvon SD. A history of neuroimaging in epilepsy 1909-2009. Epilepsia 2009;50 Suppl 3:39-49.
56. Crooks L, Hoenninger J, Arakawa M, et al. Tomography of hydrogen with nuclear magnetic resonance. Radiology 1980;136:701-706.
57. Logothetis NK. The neural basis of the blood-oxygen-level-dependent functional magnetic resonance imaging signal. Philosophical Transactions of the Royal Society B-Biological Sciences 2002;357:1003-1037.
58. Bottomley PA, Hardy CJ, Argersinger RE, Allen-Moore G. A review of 1H nuclear magnetic resonance relaxation in pathology: are T1 and T2 diagnostic? Med Phys 1987;14:1-37.
59. Blystad I, Hakansson I, Tisell A, et al. Quantitative MRI for Analysis of Active Multiple Sclerosis Lesions without Gadolinium-Based Contrast Agent. American Journal of Neuroradiology 2016;37:94-100.
60. Logothetis NK, Wandell BA. Interpreting the BOLD signal. Annual Review of Physiology 2004;66:735-769.
61. Barnes SRS, Haacke EM. Susceptibility-Weighted Imaging: Clinical Angiographic Applications. Magnetic Resonance Imaging Clinics of North America 2009;17:47-+.
62. Huneau C, Benali H, Chabriat H. Investigating Human Neurovascular Coupling Using Functional Neuroimaging: A Critical Review of Dynamic Models. Frontiers in Neuroscience 2015;9.
63. Ogawa S, Lee TM. Magnetic-Resonance-Imaging of Blood-Vessels at High Fields - Invivo and Invitro Measurements and Image Simulation. Magnetic Resonance in Medicine 1990;16:9-18.
64. Pauling L, Coryell CD. The Magnetic Properties and Structure of Hemoglobin, Oxyhemoglobin and Carbonmonoxyhemoglobin. Proc Natl Acad Sci U S A 1936;22:210-216.
65. Thulborn KR, Waterton JC, Matthews PM, Radda GK. Oxygenation Dependence of the Transverse Relaxation-Time of Water Protons in Whole-Blood at High-Field. Biochimica Et Biophysica Acta 1982;714:265-270.

66. Bandettini PA, Wong EC, Hinks RS, Tikofsky RS, Hyde JS. Time course EPI of human brain function during task activation. Magn Reson Med 1992;25:390-397.
67. Kwong KK, Belliveau JW, Chesler DA, et al. Dynamic Magnetic-Resonance-Imaging of Human Brain Activity during Primary Sensory Stimulation. Proceedings of the National Academy of Sciences of the United States of America 1992;89:5675-5679.
68. Biswal B, Yetkin FZ, Haughton VM, Hyde JS. Functional connectivity in the motor cortex of resting human brain using echo-planar MRI. Magn Reson Med 1995;34:537-541.
69. Baggio HC, Junque C. Functional MRI in Parkinson's Disease Cognitive Impairment. Int Rev Neurobiol 2019;144:29-58.
70. Mascali D, DiNuzzo M, Serra L, et al. Disruption of Semantic Network in Mild Alzheimer's Disease Revealed by Resting-State fMRI. Neuroscience 2018;371:38-48.
71. de Vos F, Koini M, Schouten TM, et al. A comprehensive analysis of resting state fMRI measures to classify individual patients with Alzheimer's disease. Neuroimage 2018;167:62-72.
72. Yu X, Wang S, Chen DY, Dodd S, Goloshevsky A, Koretsky AP. 3D mapping of somatotopic reorganization with small animal functional MRI. Neuroimage 2010;49:1667-1676.
73. Manoach DS, Schlaug G, Siewert B, et al. Prefrontal cortex fMRI signal changes are correlated with working memory load. Neuroreport 1997;8:545-549.
74. Pochon JB, Levy R, Fossati P, et al. The neural system that bridges reward and cognition in humans: An fMRI study. Proceedings of the National Academy of Sciences of the United States of America 2002;99:5669-5674.
75. Nakahara K, Hayashi T, Konishi S, Miyashita Y. Functional MRI of macaque monkeys performing a cognitive set-shifting task. Science 2002;295:1532-1536.
76. Raichle ME, MacLeod AM, Snyder AZ, Powers WJ, Gusnard DA, Shulman GL. A default mode of brain function. Proceedings of the National Academy of Sciences of the United States of America 2001;98:676-682.
77. Buxton RB, Frank LR. A model for the coupling between cerebral blood flow and oxygen metabolism during neural stimulation. Journal of Cerebral Blood Flow and Metabolism 1997;17:64-72.

78. Boxerman JL, Bandettini PA, Kwong KK, et al. The Intravascular Contribution to Fmri Signal Change - Monte-Carlo Modeling and Diffusion-Weighted Studies in-Vivo. Magnetic Resonance in Medicine 1995;34:4-10.
79. Ogawa S, Menon RS, Kim SG, Ugurbil K. On the characteristics of functional magnetic resonance imaging of the brain. Annual Review of Biophysics and Biomolecular Structure 1998;27:447-+.
80. An HY, Lin WL, Celik A, Lee YZ. Quantitative measurements of cerebral metabolic rate of oxygen utilization using MRI: a volunteer study. Nmr in Biomedicine 2001;14:441-447.
81. Gauthier CJ, Hoge RD. Magnetic resonance imaging of resting OEF and CMRO(2) using a generalized calibration model for hypercapnia and hyperoxia. Neuroimage 2012;60:1212-1225.
82. He X, Yablonskiy DA. Quantitative BOLD: Mapping of human cerebral deoxygenated blood volume and oxygen extraction fraction: Default state. Magnetic Resonance in Medicine 2007;57:115-126.
83. Logothetis NK. The underpinnings of the BOLD functional magnetic resonance imaging signal. J Neurosci 2003;23:3963-3971.
84. Glover GH. Deconvolution of impulse response in event-related BOLD fMRI. Neuroimage 1999;9:416-429.
85. Fox PT, Raichle ME. Focal physiological uncoupling of cerebral blood flow and oxidative metabolism during somatosensory stimulation in human subjects. Proc Natl Acad Sci U S A 1986;83:1140-1144.
86. Fox PT, Raichle ME, Mintun MA, Dence C. Nonoxidative glucose consumption during focal physiologic neural activity. Science 1988;241:462-464.
87. van Zijl PCM, Hua J, Lu HZ. The BOLD post-stimulus undershoot, one of the most debated issues in fMRI. Neuroimage 2012;62:1092-1102.
88. Solo V, Cassidy B, Long C, Rae C. Time-to-Onset Latency in Fmri: Fast Detection of Delayed Activation. 2011 Ieee International Conference on Acoustics, Speech, and Signal Processing 2011:725-728.

89. Desjardins M, Kilic K, Thunemann M, et al. Awake Mouse Imaging: From Two-Photon Microscopy to Blood Oxygen Level-Dependent Functional Magnetic Resonance Imaging. Biol Psychiatry Cogn Neurosci Neuroimaging 2019;4:533-542.
90. Lee JH, Durand R, Gradinaru V, et al. Global and local fMRI signals driven by neurons defined optogenetically by type and wiring. Nature 2010;465:788-792.
91. Calamante F, Thomas DL, Pell GS, Wiersma J, Turner R. Measuring cerebral blood flow using magnetic resonance imaging techniques. Journal of Cerebral Blood Flow and Metabolism 1999;19:701-735.
92. Lu H, van Zijl PC. A review of the development of Vascular-Space-Occupancy (VASO) fMRI. Neuroimage 2012;62:736-742.
93. Blockley NP, Griffeth VE, Simon AB, Buxton RB. A review of calibrated blood oxygenation level-dependent (BOLD) methods for the measurement of task-induced changes in brain oxygen metabolism. NMR Biomed 2013;26:987-1003.
94. Yarkoni T. Big Correlations in Little Studies: Inflated fMRI Correlations Reflect Low Statistical Power-Commentary on Vul et al. (2009). Perspect Psychol Sci 2009;4:294-298.
95. Haller S, Bartsch AJ. Pitfalls in FMRI. Eur Radiol 2009;19:2689-2706.
96. Beaulieu C. Numerical data on neocortical neurons in adult rat, with special reference to the GABA population. Brain Res 1993;609:284-292.
97. Albers F, Schmid F, Wachsmuth L, Faber C. Line scanning fMRI reveals earlier onset of optogenetically evoked BOLD response in rat somatosensory cortex as compared to sensory stimulation. Neuroimage 2018;164:144-154.
98. Kashyap S, Ivanov D, Havlicek M, Huber L, Poser BA, Uludag K. Sub-millimetre resolution laminar fMRI using Arterial Spin Labelling in humans at 7 T (vol 16, e0250504, 2021). Plos One 2021;16.
99. Moia S, Termenon M, Urunuela E, et al. ICA-based denoising strategies in breath-hold induced cerebrovascular reactivity mapping with multi echo BOLD fMRI. Neuroimage 2021;233.
100. Self MW, Roelfsema PR. Paying Attention to the Cortical Layers. Neuron 2017;93:9-11.
101. Chen BR, Bouchard MB, McCaslin AF, Burgess SA, Hillman EM. High-speed vascular dynamics of the hemodynamic response. Neuroimage 2011;54:1021-1030.

102. Duvernoy HM, Delon S, Vannson JL. Cortical Blood-Vessels of the Human-Brain. Brain Research Bulletin 1981;7:519-579.
103. Raimondo L, Knapen T, Oliveira IAF, et al. A line through the brain: implementation of human line-scanning at 7T for ultra-high spatiotemporal resolution fMRI. Journal of Cerebral Blood Flow and Metabolism 2021;41:2831-2843.
104. Chen TW, Wardill TJ, Sun Y, et al. Ultrasensitive fluorescent proteins for imaging neuronal activity. Nature 2013;499:295-+.
105. Li P, Geng X, Jiang H, Caccavano A, Vicini S, Wu JY. Measuring Sharp Waves and Oscillatory Population Activity With the Genetically Encoded Calcium Indicator GCaMP6f. Front Cell Neurosci 2019;13:274.
106. Lahti KM. Imaging brain activity in conscious animals using functional MRI. 1998.
107. Lukasik VM, Gillies RJ. Animal anaesthesia for in vivo magnetic resonance. NMR Biomed 2003;16:459-467.
108. Williams KA, Magnuson M, Majeed W, et al. Comparison of alpha-chloralose, medetomidine and isoflurane anesthesia for functional connectivity mapping in the rat. Magn Reson Imaging 2010;28:995-1003.
109. Nallasamy N, Tsao DY. Functional connectivity in the brain: effects of anesthesia. Neuroscientist 2011;17:94-106.
110. Paasonen J, Stenroos P, Salo RA, Kiviniemi V, Grohn O. Functional connectivity under six anesthesia protocols and the awake condition in rat brain. Neuroimage 2018;172:9-20.
111. Kashyap S, Ivanov D, Havlicek M, Sengupta S, Poser BA, Uludag K. Resolving laminar activation in human V1 using ultra-high spatial resolution fMRI at 7T. Sci Rep 2018;8:17063.
112. Lawrence SJD, Formisano E, Muckli L, de Lange FP. Laminar fMRI: Applications for cognitive neuroscience. Neuroimage 2019;197:785-791.
113. Goense J, Merkle H, Logothetis NK. High-resolution fMRI reveals laminar differences in neurovascular coupling between positive and negative BOLD responses. Neuron 2012;76:629-639.
114. Huber L, Uludag K, Moller HE. Non-BOLD contrast for laminar fMRI in humans: CBF, CBV, and CMRO2. Neuroimage 2019;197:742-760.

115. Goense JB, Logothetis NK. Laminar specificity in monkey V1 using high-resolution SE-fMRI. Magn Reson Imaging 2006;24:381-392.
116. Jin T, Kima SG. Improved cortical-layer specificity of vascular space occupancy fMRI with slab inversion relative to spin-echo BOLD at 9.4 T. Neuroimage 2008;40:59-67.
117. Moon CH, Fukuda M, Kim SG. Spatiotemporal characteristics and vascular sources of neural-specific and -nonspecific fMRI signals at submillimeter columnar resolution. Neuroimage 2013;64:91-103.
118. Zhao F, Wang P, Hendrich K, Ugurbil K, Kim SG. Cortical layer-dependent BOLD and CBV responses measured by spin-echo and gradient-echo fMRI: insights into hemodynamic regulation. Neuroimage 2006;30:1149-1160.
119. Alsop DC, Detre JA, Golay X, et al. Recommended Implementation of Arterial Spin-Labeled Perfusion MRI for Clinical Applications: A Consensus of the ISMRM Perfusion Study Group and the European Consortium for ASL in Dementia. Magnetic Resonance in Medicine 2015;73:102-116.
120. Lin AL, Fox PT, Yang Y, Lu H, Tan LH, Gao JH. Evaluation of MRI models in the measurement of CMRO2 and its relationship with CBF. Magn Reson Med 2008;60:380-389.
121. Albers F, Wachsmuth L, van Alst TM, Faber C. Multimodal Functional Neuroimaging by Simultaneous BOLD fMRI and Fiber-Optic Calcium Recordings and Optogenetic Control. Molecular Imaging and Biology 2018;20:171-182.
122. Tong CJ, Dai JK, Chen YY, Zhang KW, Feng YQ, Liang ZF. Differential coupling between subcortical calcium and BOLD signals during evoked and resting state through simultaneous calcium fiber photometry and fMRI. Neuroimage 2019;200:405-413.
123. Scheeringa R, Koopmans PJ, van Mourik T, Jensen O, Norris DG. The relationship between oscillatory EEG activity and the laminar-specific BOLD signal. Proc Natl Acad Sci U S A 2016;113:6761-6766.
124. Ma Y, Shaik MA, Kozberg MG, et al. Resting-state hemodynamics are spatiotemporally coupled to synchronized and symmetric neural activity in excitatory neurons. Proc Natl Acad Sci U S A 2016;113:E8463-E8471.
125. Chen TW, Wardill TJ, Sun Y, et al. Ultrasensitive fluorescent proteins for imaging neuronal activity. Nature 2013;499:295-300.

126. He Y, Wang M, Chen X, et al. Ultra-Slow Single-Vessel BOLD and CBV-Based fMRI Spatiotemporal Dynamics and Their Correlation with Neuronal Intracellular Calcium Signals. Neuron 2018;97:925-939 e925.
127. Sobczak F, He Y, Sejnowski TJ, Yu X. Predicting the fMRI Signal Fluctuation with Recurrent Neural Networks Trained on Vascular Network Dynamics. Cereb Cortex 2020.
128. Delorme A, Makeig S. EEGLAB: an open source toolbox for analysis of single-trial EEG dynamics including independent component analysis. J Neurosci Methods 2004;134:9-21.
129. Chen X, Sobczak F, Chen Y, et al. Mapping optogenetically-driven single-vessel fMRI with concurrent neuronal calcium recordings in the rat hippocampus. Nat Commun 2019;10:5239.
130. Schlegel F. Fiber-optic implant for simultaneous fluorescencebased calcium recordings and BOLD fMRI in mice. 2018.
131. Schwalm M, Schmid F, Wachsmuth L, et al. Cortex-wide BOLD fMRI activity reflects locally-recorded slow oscillation-associated calcium waves. Elife 2017;6.
132. Fox MD, Raichle ME. Spontaneous fluctuations in brain activity observed with functional magnetic resonance imaging. Nat Rev Neurosci 2007;8:700-711.
133. Pais-Roldan P, Takahashi K, Sobczak F, et al. Indexing brain state-dependent pupil dynamics with simultaneous fMRI and optical fiber calcium recording. Proc Natl Acad Sci U S A 2020.
134. Turner R. How much cortex can a vein drain? Downstream dilution of activation-related cerebral blood oxygenation changes. Neuroimage 2002;16:1062-1067.
135. Tian P, Teng IC, May LD, et al. Cortical depth-specific microvascular dilation underlies laminar differences in blood oxygenation level-dependent functional MRI signal. Proc Natl Acad Sci U S A 2010;107:15246-15251.
136. Mateo C, Knutsen PM, Tsai PS, Shih AY, Kleinfeld D. Entrainment of Arteriole Vasomotor Fluctuations by Neural Activity Is a Basis of Blood-Oxygenation-Level-Dependent "Resting-State" Connectivity. Neuron 2017;96:936-948 e933.
137. Mitra A, Kraft A, Wright P, et al. Spontaneous Infra-slow Brain Activity Has Unique Spatiotemporal Dynamics and Laminar Structure. Neuron 2018;98:297-+.

138. Winder AT, Echagarruga C, Zhang QG, Drew PJ. Weak correlations between hemodynamic signals and ongoing neural activity during the resting state. Nature Neuroscience 2017;20:1761-+.
139. Smith SM, Vidaurre D, Beckmann CF, et al. Functional connectomics from resting-state fMRI. Trends Cogn Sci 2013;17:666-682.
140. Lake EMR, Ge X, Shen X, et al. Simultaneous cortex-wide fluorescence Ca(2+) imaging and whole-brain fMRI. Nat Methods 2020;17:1262-1271.
141. Stroh A, Adelsberger H, Groh A, et al. Making Waves: Initiation and Propagation of Corticothalamic Ca2+ Waves In Vivo. Neuron 2013;77:1136-1150.
142. Ress D, Glover GH, Liu J, Wandell B. Laminar profiles of functional activity in the human brain. Neuroimage 2007;34:74-84.
143. Baek K, Shim WH, Jeong J, et al. Layer-specific interhemispheric functional connectivity in the somatosensory cortex of rats: resting state electrophysiology and fMRI studies. Brain Struct Funct 2016;221:2801-2815.
144. Larkum ME, Petro LS, Sachdev RNS, Muckli L. A Perspective on Cortical Layering and Layer-Spanning Neuronal Elements. Front Neuroanat 2018;12:56.
145. Goense JBM, Logothetis NK. Neurophysiology of the BOLD fMRI signal in awake monkeys. Current Biology 2008;18:631-640.
146. Shimaoka D, Steinmetz NA, Harris KD, Carandini M. The impact of bilateral ongoing activity on evoked responses in mouse cortex. Elife 2019;8.
147. Fox MD, Snyder AZ, Zacks JM, Raichle ME. Coherent spontaneous activity accounts for trial-to-trial variability in human evoked brain responses. Nat Neurosci 2006;9:23-25.
148. Chen Y, Sobczak F, Pais-Roldan P, Schwarz C, Koretsky AP, Yu X. Mapping the Brain-Wide Network Effects by Optogenetic Activation of the Corpus Callosum. Cereb Cortex 2020;30:5885-5898.
149. Magnuson ME, Thompson GJ, Pan WJ, Keilholz SD. Effects of severing the corpus callosum on electrical and BOLD functional connectivity and spontaneous dynamic activity in the rat brain. Brain Connect 2014;4:15-29.
150. Mohajerani MH, McVea DA, Fingas M, Murphy TH. Mirrored Bilateral Slow-Wave Cortical Activity within Local Circuits Revealed by Fast Bihemispheric Voltage-Sensitive

Dye Imaging in Anesthetized and Awake Mice. Journal of Neuroscience 2010;30:3745-3751.

151. Tyszka JM, Kennedy DP, Adolphs R, Paul LK. Intact bilateral resting-state networks in the absence of the corpus callosum. J Neurosci 2011;31:15154-15162.

152. Hoffmeyer HW, Enager P, Thomsen KJ, Lauritzen MJ. Nonlinear neurovascular coupling in rat sensory cortex by activation of transcallosal fibers. J Cereb Blood Flow Metab 2007;27:575-587.

153. Iordanova B, Vazquez A, Kozai TD, Fukuda M, Kim SG. Optogenetic investigation of the variable neurovascular coupling along the interhemispheric circuits. J Cereb Blood Flow Metab 2018;38:627-640.

154. Bloom JS, Hynd GW. The role of the corpus callosum in interhemispheric transfer of information: excitation or inhibition? Neuropsychol Rev 2005;15:59-71.

155. Cruikshank SJ, Lewis TJ, Connors BW. Synaptic basis for intense thalamocortical activation of feedforward inhibitory cells in neocortex. Nat Neurosci 2007;10:462-468.

156. Swadlow HA. Thalamocortical control of feed-forward inhibition in awake somatosensory 'barrel' cortex. Philosophical Transactions of the Royal Society B-Biological Sciences 2002;357:1717-1727.

157. Harris KD, Shepherd GM. The neocortical circuit: themes and variations. Nat Neurosci 2015;18:170-181.

158. Ferris CF, Kulkarni P, Toddes S, Yee J, Kenkel W, Nedelman M. Studies on the Q175 Knock-in Model of Huntington's Disease Using Functional Imaging in Awake Mice: Evidence of Olfactory Dysfunction. Front Neurol 2014;5:94.

159. Thrane AS, Rangroo Thrane V, Zeppenfeld D, et al. General anesthesia selectively disrupts astrocyte calcium signaling in the awake mouse cortex. Proc Natl Acad Sci U S A 2012;109:18974-18979.

160. Makaryus R, Lee H, Yu M, et al. The metabolomic profile during isoflurane anesthesia differs from propofol anesthesia in the live rodent brain. J Cereb Blood Flow Metab 2011;31:1432-1442.

161. Febo M. Technical and conceptual considerations for performing and interpreting functional MRI studies in awake rats. Front Psychiatry 2011;2:43.

162. Low LA, Bauer LC, Pitcher MH, Bushnell MC. Restraint training for awake functional brain scanning of rodents can cause long-lasting changes in pain and stress responses. Pain 2016;157:1761-1772.
163. King JA, Garelick TS, Brevard ME, et al. Procedure for minimizing stress for fMRI studies in conscious rats. J Neurosci Methods 2005;148:154-160.
164. Takata N, Sugiura Y, Yoshida K, et al. Optogenetic astrocyte activation evokes BOLD fMRI response with oxygen consumption without neuronal activity modulation. Glia 2018;66:2013-2023.
165. Bradley MM, Miccoli L, Escrig MA, Lang PJ. The pupil as a measure of emotional arousal and autonomic activation. Psychophysiology 2008;45:602-607.
166. Ebitz RB, Pearson JM, Platt ML. Pupil size and social vigilance in rhesus macaques. Front Neurosci 2014;8:100.
167. Partala T, Surakka V. Pupil size variation as an indication of affective processing. International Journal of Human-Computer Studies 2003;59:185-198.
168. Reimer J, Froudarakis E, Cadwell CR, Yatsenko D, Denfield GH, Tolias AS. Pupil fluctuations track fast switching of cortical states during quiet wakefulness. Neuron 2014;84:355-362.
169. Schneider M, Leuchs L, Czisch M, Samann PG, Spoormaker VI. Disentangling reward anticipation with simultaneous pupillometry / fMRI. Neuroimage 2018;178:11-22.
170. Schneider M, Hathway P, Leuchs L, Samann PG, Czisch M, Spoormaker VI. Spontaneous pupil dilations during the resting state are associated with activation of the salience network. Neuroimage 2016;139:189-201.
171. Murphy PR, O'Connell RG, O'Sullivan M, Robertson IH, Balsters JH. Pupil diameter covaries with BOLD activity in human locus coeruleus. Hum Brain Mapp 2014;35:4140-4154.
172. Schwarz C, Hentschke H, Butovas S, et al. The head-fixed behaving rat--procedures and pitfalls. Somatosens Mot Res 2010;27:131-148.
173. Cox RW. AFNI: software for analysis and visualization of functional magnetic resonance neuroimages. Comput Biomed Res 1996;29:162-173.
174. Dinh TNA, Jung WB, Shim HJ, Kim SG. Characteristics of fMRI responses to visual stimulation in anesthetized vs. awake mice. Neuroimage 2021;226:117542.

175. Froudarakis E, Fahey PG, Reimer J, Smirnakis SM, Tehovnik EJ, Tolias AS. The Visual Cortex in Context. Annu Rev Vis Sci 2019;5:317-339.
176. Mathis A, Mamidanna P, Cury KM, et al. DeepLabCut: markerless pose estimation of user-defined body parts with deep learning. Nat Neurosci 2018;21:1281-1289.
177. Lau C, Zhou IY, Cheung MM, Chan KC, Wu EX. BOLD temporal dynamics of rat superior colliculus and lateral geniculate nucleus following short duration visual stimulation. PLoS One 2011;6:e18914.
178. Reed MD, Pira AS, Febo M. Behavioral effects of acclimatization to restraint protocol used for awake animal imaging. J Neurosci Methods 2013;217:63-66.
179. Grandjean J, Corcoba A, Kahn MC, et al. A brain-wide functional map of the serotonergic responses to acute stress and fluoxetine. Nat Commun 2019;10:350.
180. Harris AP, Lennen RJ, Marshall I, et al. Imaging learned fear circuitry in awake mice using fMRI. Eur J Neurosci 2015;42:2125-2134.
181. Unsworth N, Robison MK. Pupillary correlates of covert shifts of attention during working memory maintenance. Atten Percept Psychophys 2017;79:782-795.
182. Alnaes D, Sneve MH, Espeseth T, Endestad T, van de Pavert SH, Laeng B. Pupil size signals mental effort deployed during multiple object tracking and predicts brain activity in the dorsal attention network and the locus coeruleus. J Vis 2014;14.
183. Marco Pedrotti MAM, Adrien Tedescho, Jean-Rémy Chardonnet, FrédéricMerienne, et al. Automatic Stress Classification With Pupil Diameter Analysis. International Journal of Human-Computer Interaction 2014.
184. Joshi S, Gold JI. Pupil Size as a Window on Neural Substrates of Cognition. Trends Cogn Sci 2020;24:466-480.
185. Schwarz M SK, Wand P. Sensory-motor processing in substantia nigra pars reticulata in conscious cats. J Physiol 1984.
186. Berenyi A, Gombkoto P, Farkas A, et al. How moving visual stimuli modulate the activity of the substantia nigra pars reticulata. Neuroscience 2009;163:1316-1326.
187. Seabrook TA, Burbridge TJ, Crair MC, Huberman AD. Architecture, Function, and Assembly of the Mouse Visual System. Annu Rev Neurosci 2017;40:499-538.

188. Peeters RR, Tindemans I, De Schutter E, Van der Linden A. Comparing BOLD fMRI signal changes in the awake and anesthetized rat during electrical forepaw stimulation. Magn Reson Imaging 2001;19:821-826.
189. Karolis VR, Corbetta M, Thiebaut de Schotten M. The architecture of functional lateralisation and its relationship to callosal connectivity in the human brain. Nat Commun 2019;10:1417.
190. Cazettes F, Reato D, Morais JP, Renart A, Mainen ZF. Phasic Activation of Dorsal Raphe Serotonergic Neurons Increases Pupil Size. Current Biology 2021;31:192-+.
191. Niell CM, Stryker MP. Modulation of visual responses by behavioral state in mouse visual cortex. Neuron 2010;65:472-479.

7. Acknowledgment

Firstly, I would like to thank my previous mentor Dr. Xin Yu for his guidance and the designs of the projects.

Secondly, I particularly thank my advisory board members: Prof. Dr. Klaus Scheffler, Prof. Dr. Cornelius Schwarz and Prof. Dr. Sandra Beer-Hammer for their guidance and comments during my thesis writing. Furthermore, I would also like to sincerely thank again Dr. Cornelius Schwarz and Dr. Sandra Beer-Hammer for their patience and encouragement, when I am feeling depressed and hopeless in my last year of PhD training.

Thirdly, I really appreciate my colleagues from MPI who provided me technical supports and animal maintenance supports. Without your supports, I can hardly continue those projects and finish my PhD training.

Finally yet importantly, I would also like to thank my family and friends who were always being there to support and encourage me to be good and do the right things that I have been aiming for.

8. Appendix.

8.1 Supplementary materials

Chapter I

Part 1: Concurrent intracellular calcium recordings with laminar fMRI mapping

Part I: Concurrent intracellular calcium recordings with laminar fMRI mapping

Fig.S1: Schematic of calcium recording and multi-slice line-scanning fMRI.

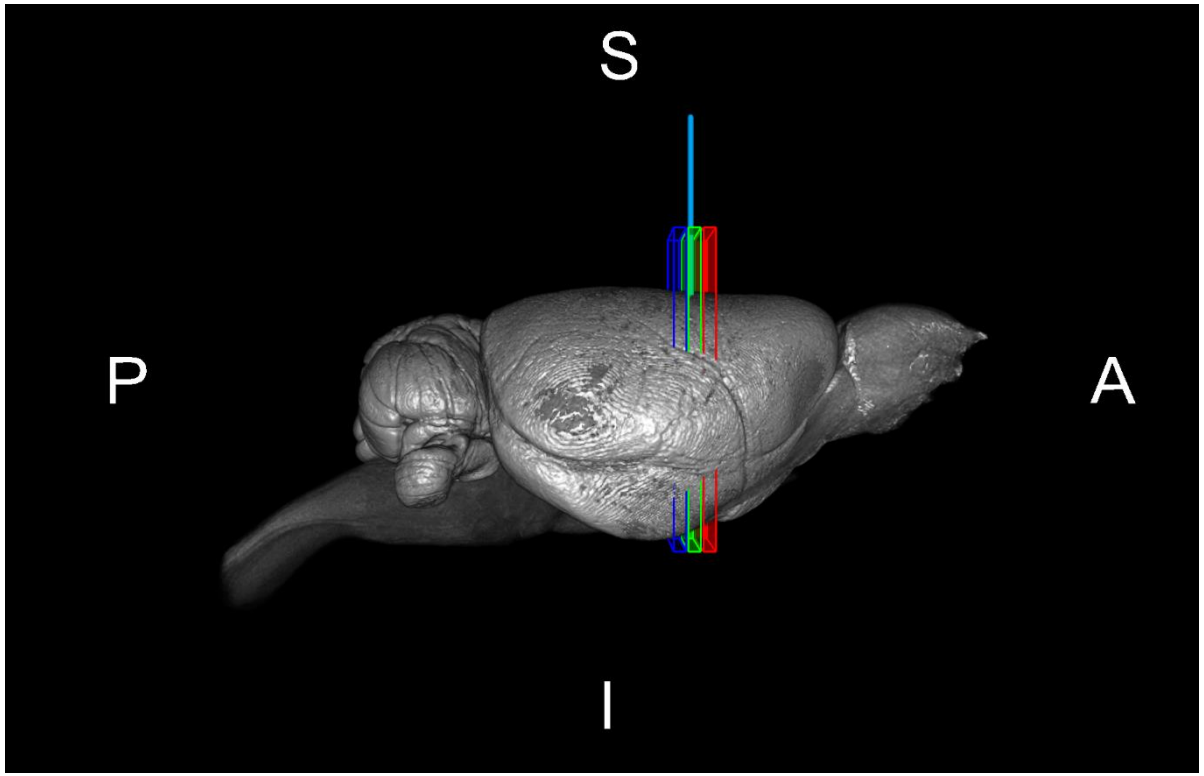

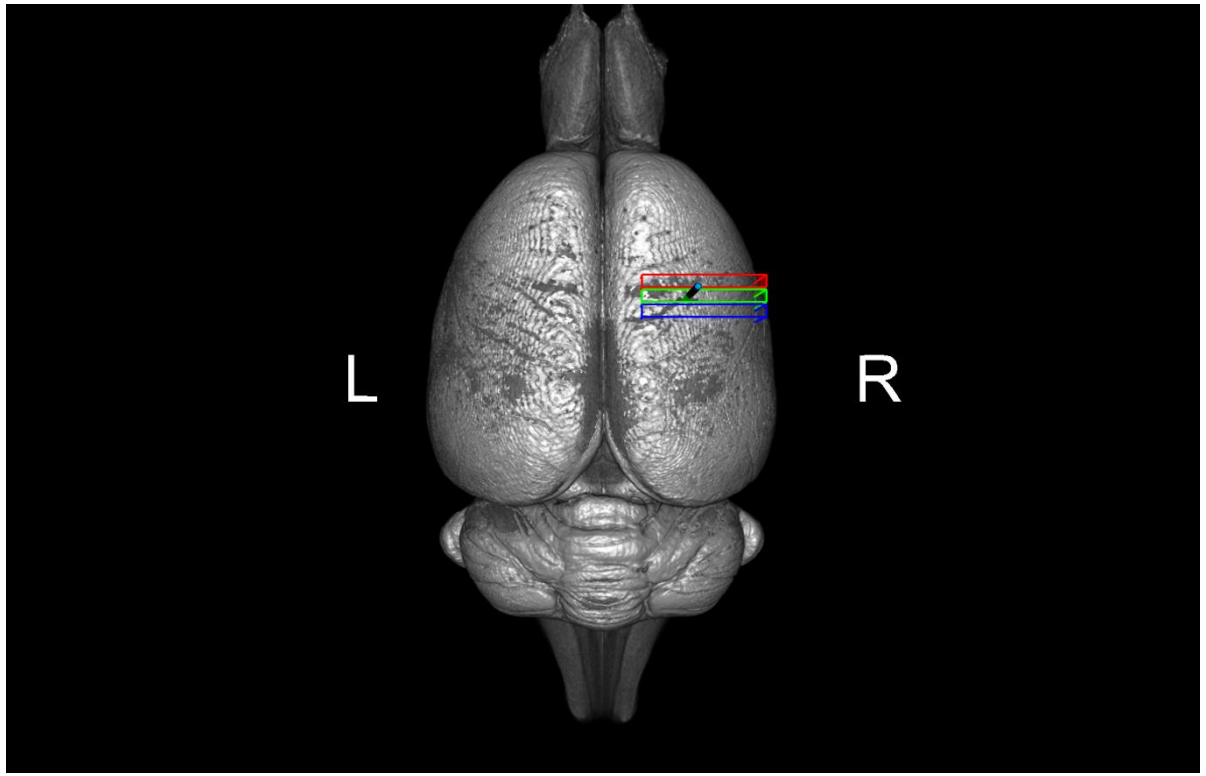

Video. S1: Schematic of calcium recording and multi-slice line-scanning fMRI.

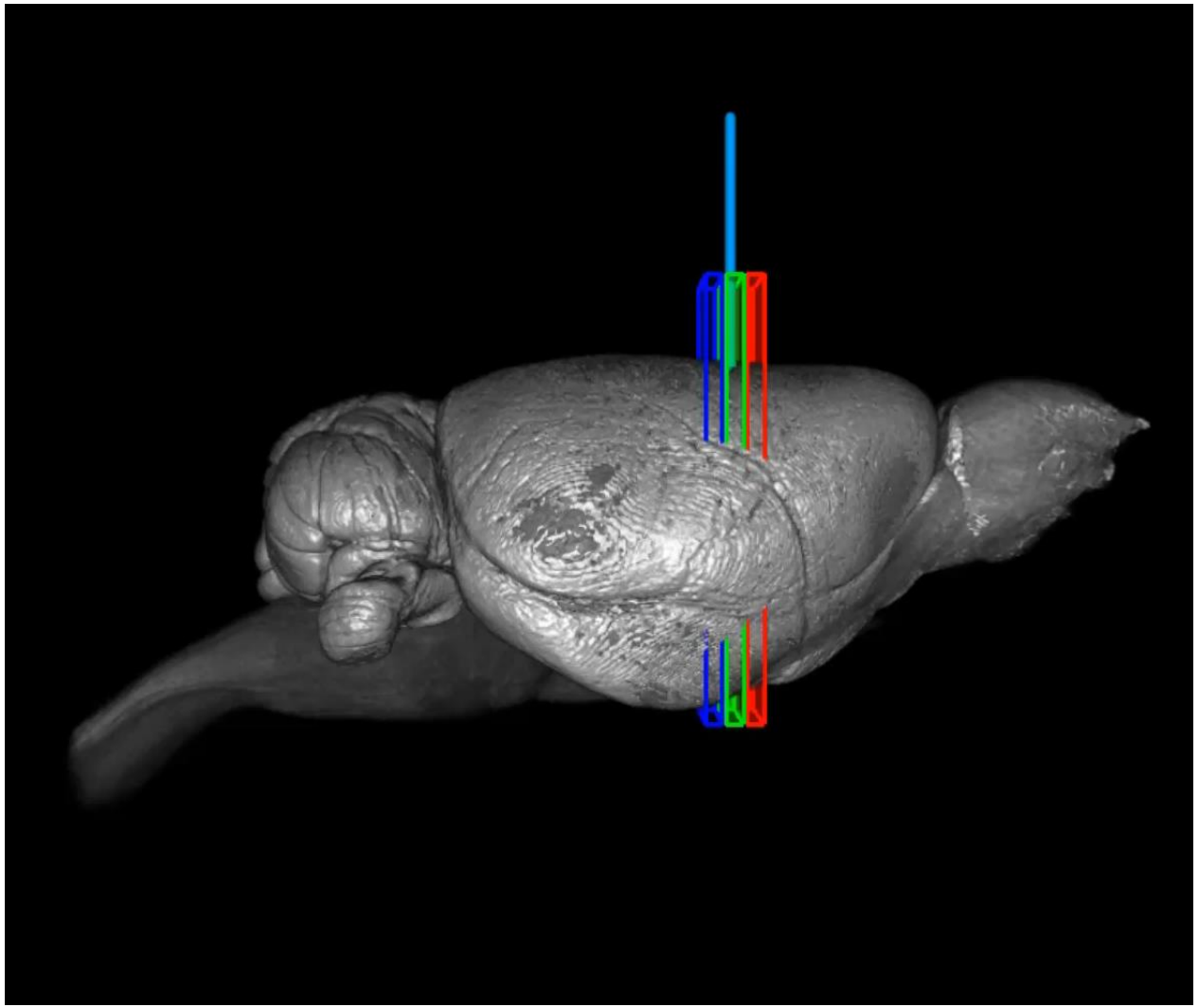

Fig.S2. The onset time of the evoked GCaMP-mediated Ca2+ signal

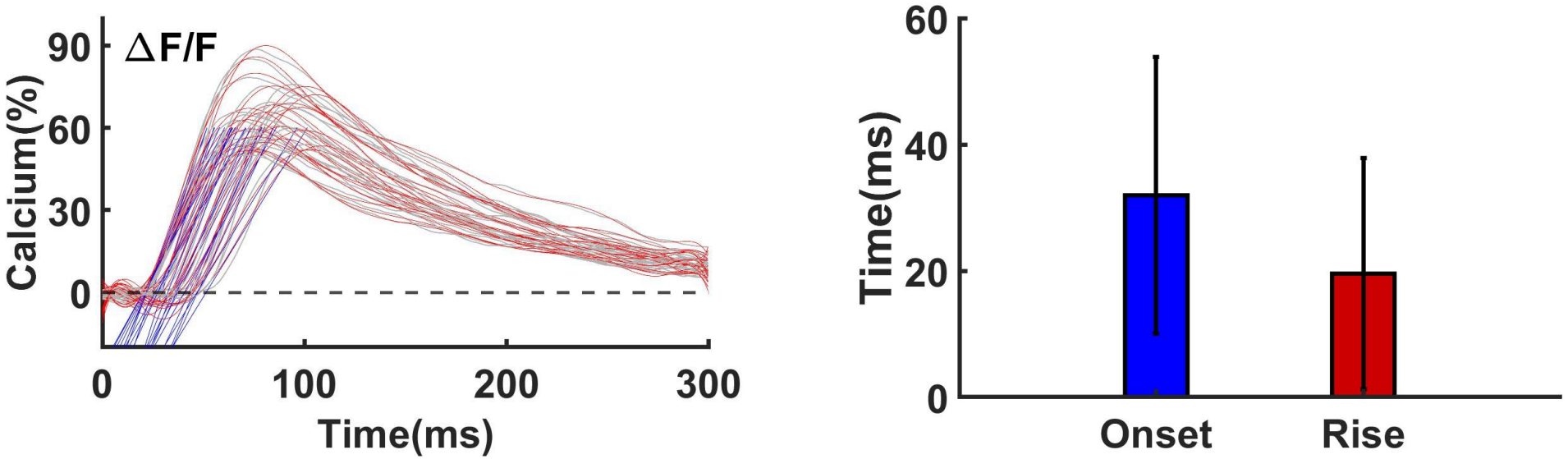

Fig.S2. The onset time of the evoked GCaMP-mediated Ca2+ signal. Grey curves are the raw traces. Red lines are the higher-order polynomial fitting (10^{th} order). Blue lines are the intercepts fittings from the 20% and 80% maximum intensity peak. The onset time was estimated by fitting the baseline to the intercepts and rise time was defined as time between onset of the transients and 50% of maximum intensity peak. Onset time: 31.9±10ms (23 traces from one animal, mean±S.D). Rise time: 19.6±1.2ms (23 traces from one animal, mean±S.D).

Video.S2. Cross correlation patterns between calcium and BOLD within the three slices.

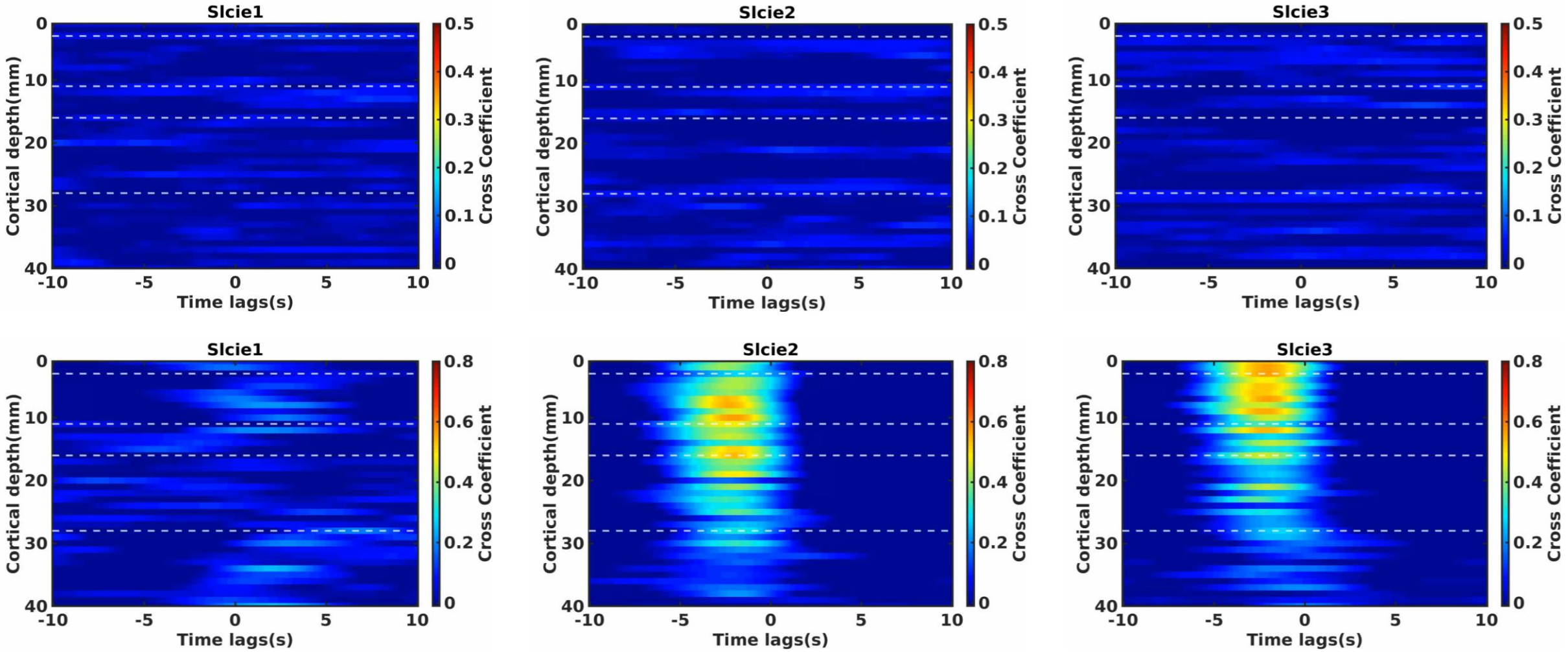

Video.S2. Cross correlation patterns between calcium and BOLD within the three slices. Individual trails of the cross correlations patterns showing diverse cross-correlation patterns in resting-state and a more synchronized state in evoked conditions, both of which showed a 1-5s earlier calcium events than fMRI across the cortical depths.

Chapter I

Part 2: Bilateral line-scanning fMRI with intracellular calcium recording

Part 2: Bilateral line-scanning fMRI with intracellular calcium recording

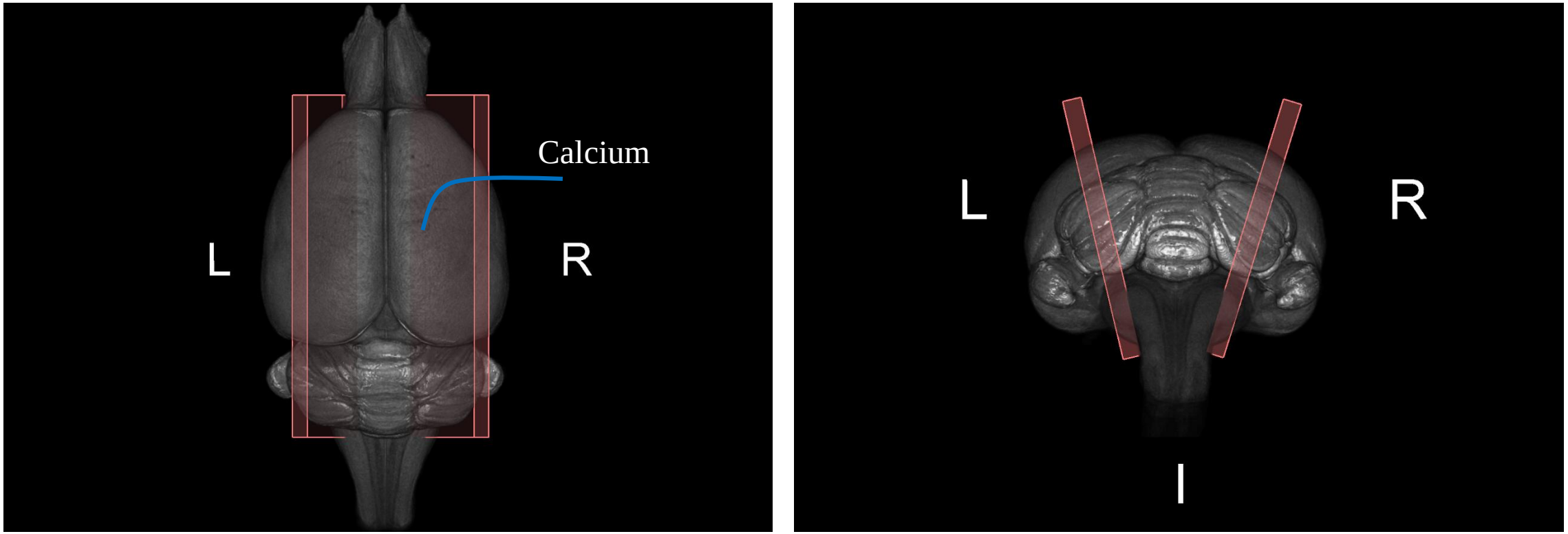

Fig.S1. Bilateral slice displacement and calcium recording in the rat FP-S1 in left and right hemisphere

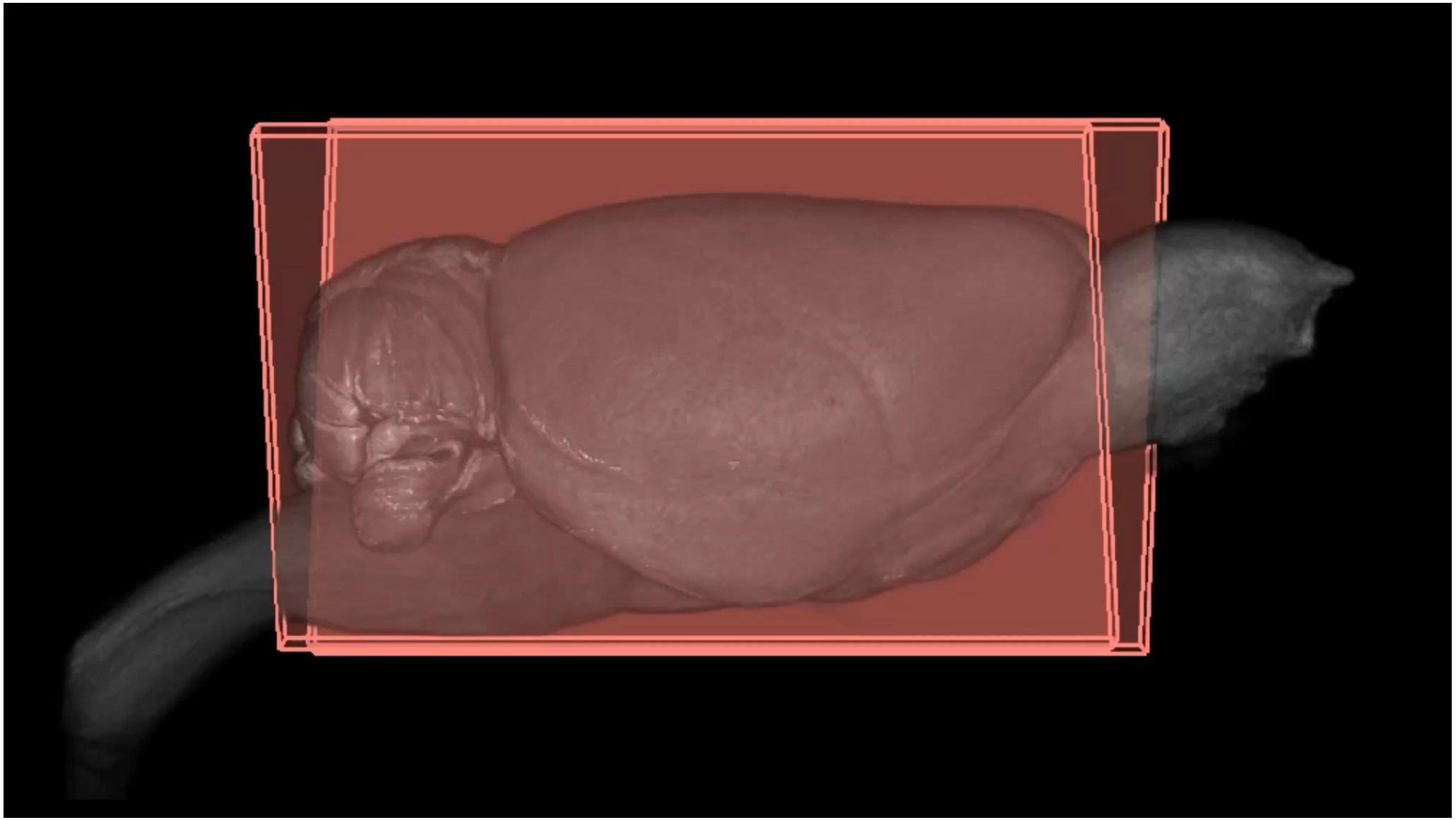

Video.S1. Bilateral line scanning fMRI with calcium recording

Chapter II

Awake mouse fMRI and pupillary recordings in ultrahigh magnetic field

Fig.S1. Customized awake restraint system.

a. Schematic setups for awake mouse

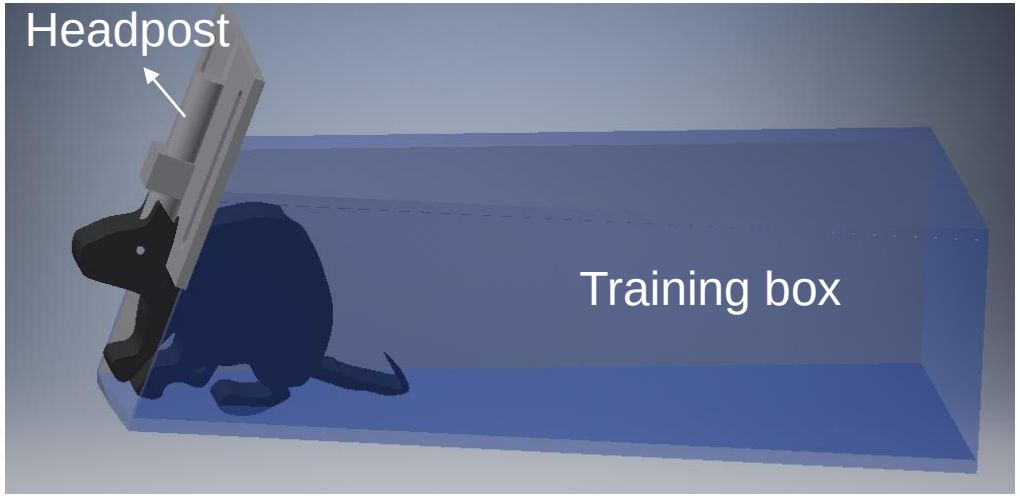

b. 3D printed headpost

c. 3D printed training box

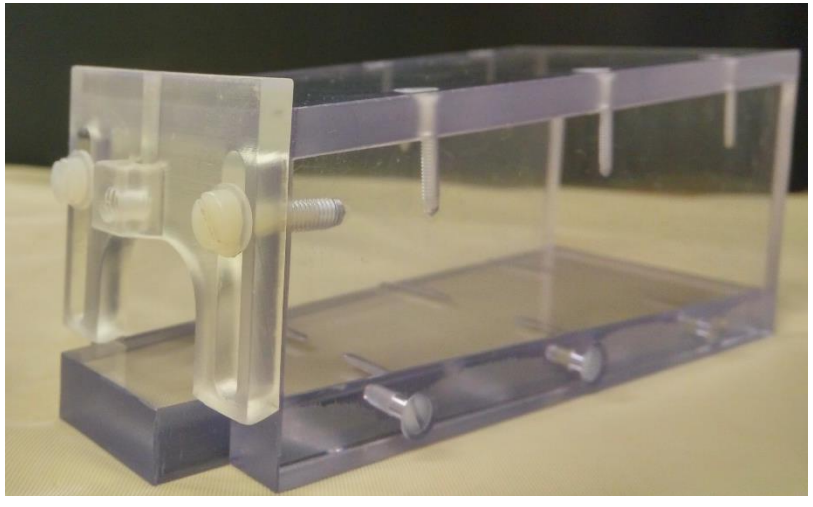

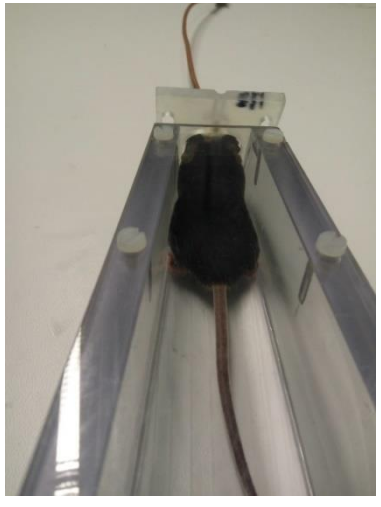

Fig.S2. Customized camera hold and LED light matrix for visual stimulation.

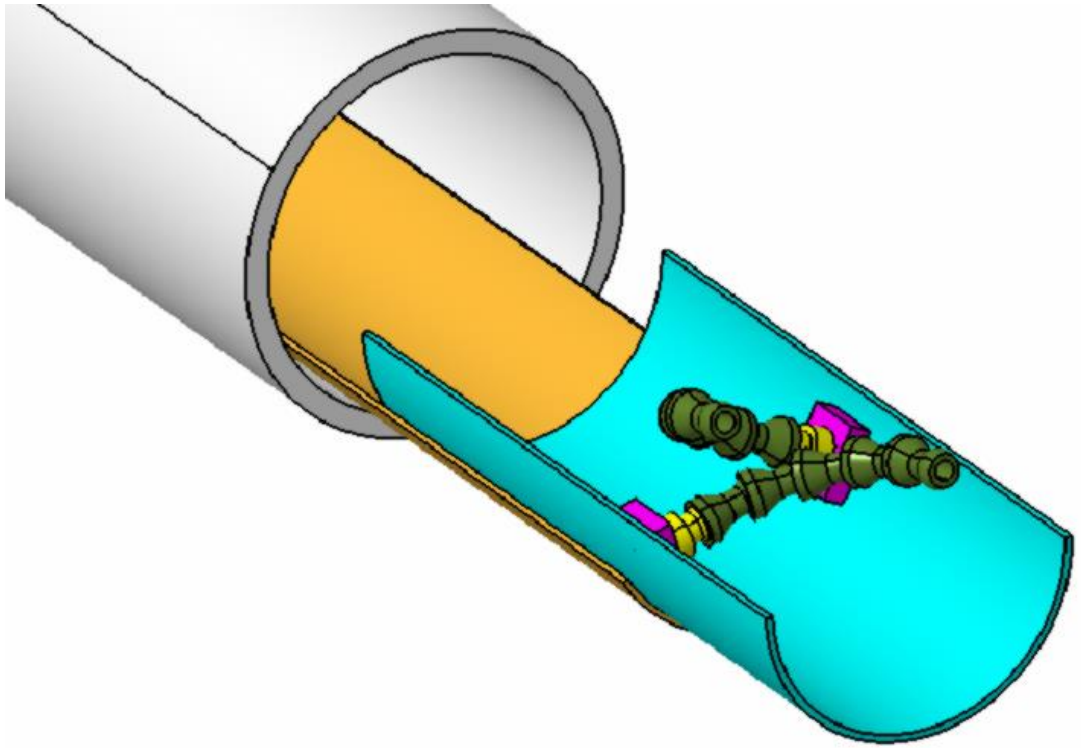

a. adjustable camera holder

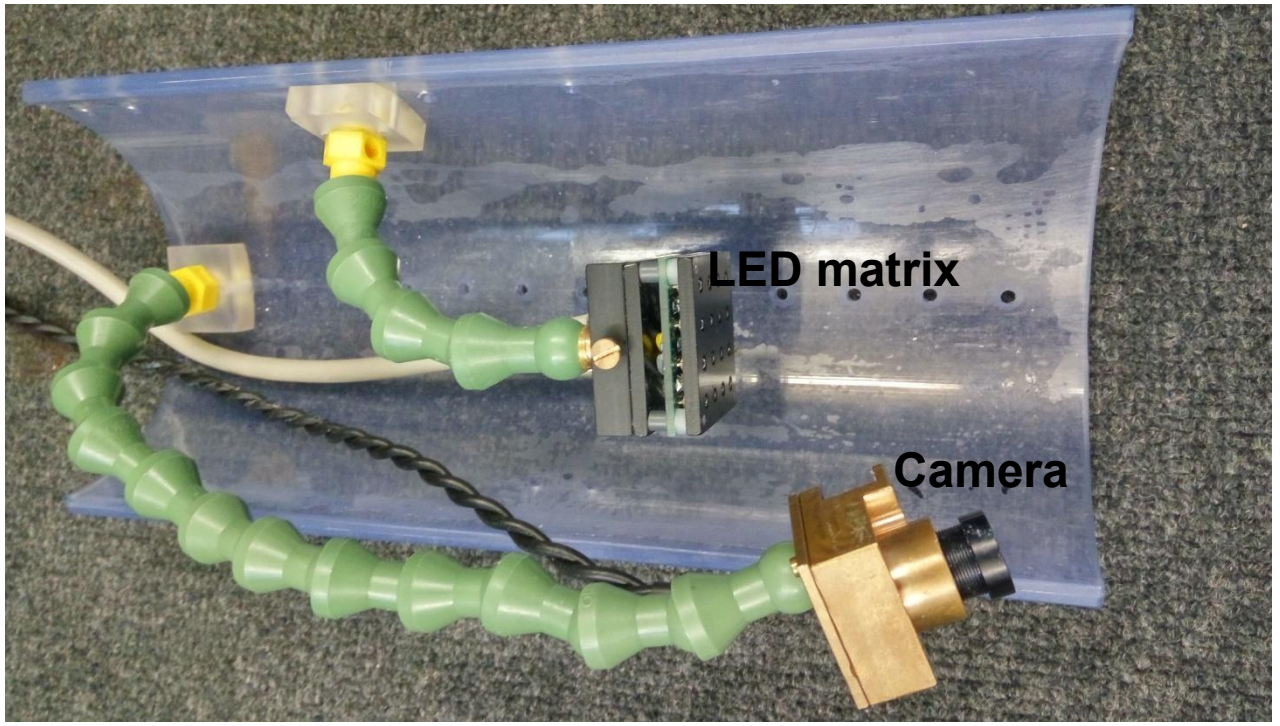

b. copper coded camera and customized LED Matrix

Fig.S3. Chest motion assessment.

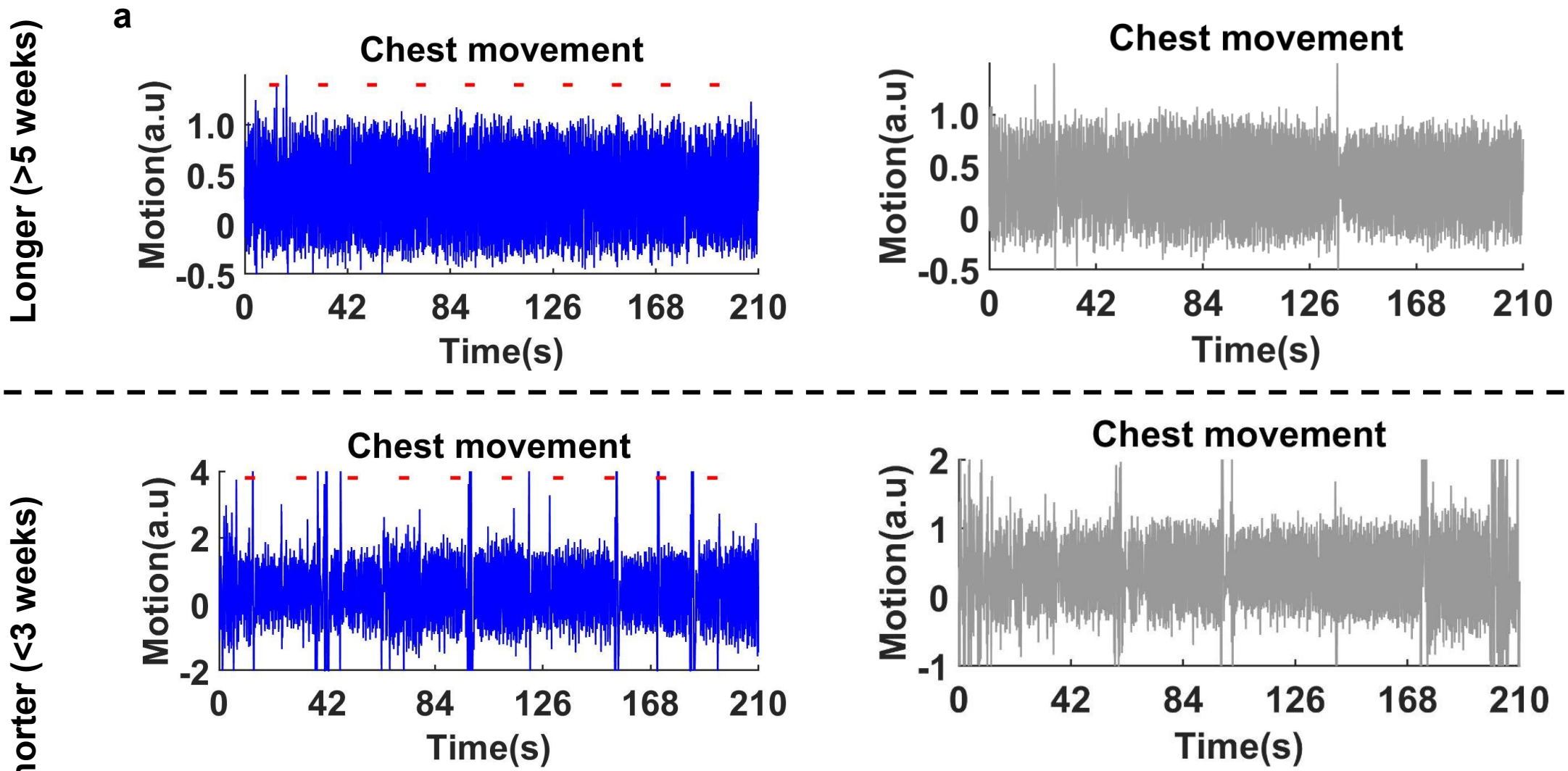

Fig.S3a. Representative trails of chest motion assessments from one mouse. Upper panel, longer training(>5weeks); lower panel, shorter training (<3weeks); blue color, light on; gray color, light off; red line, duration of light on (4s-on-16s-off).

Fig.S3. Chest motion assessment.

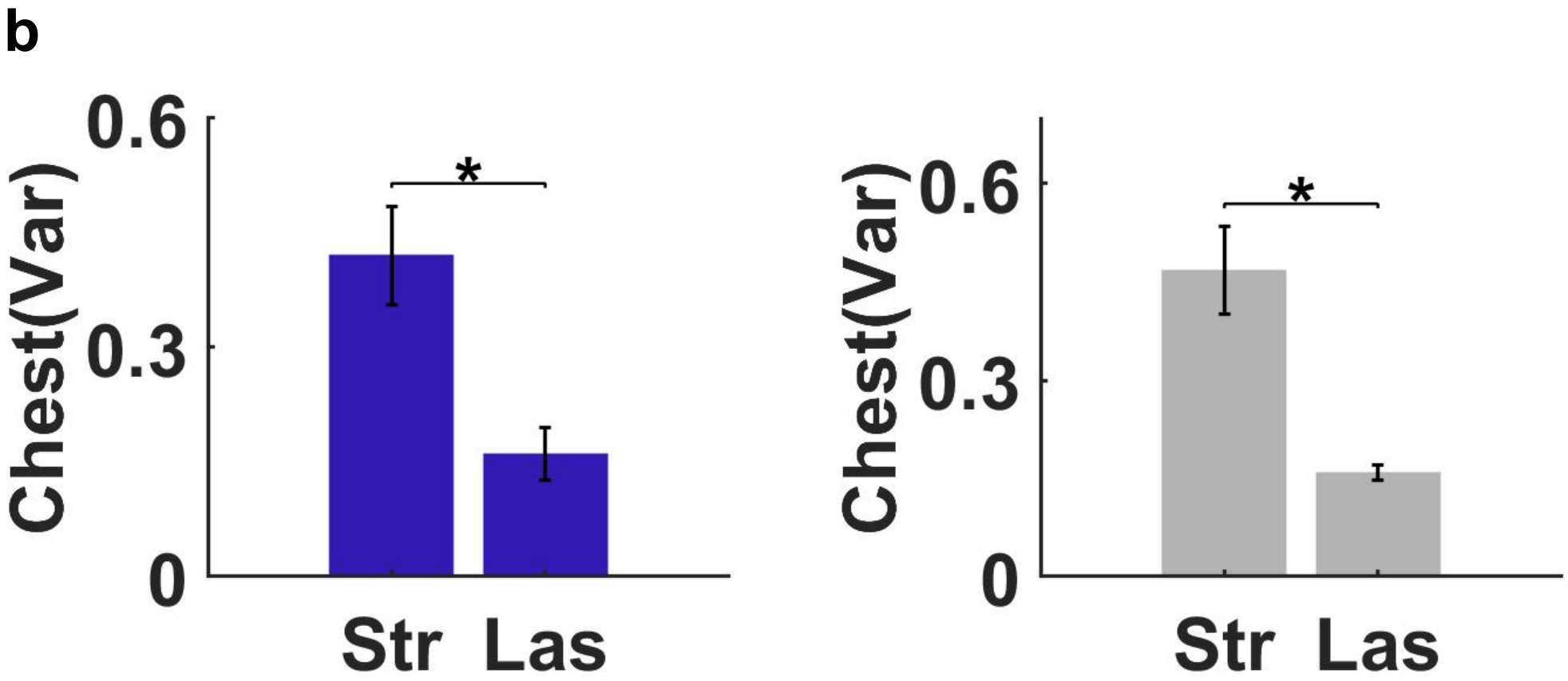

Fig.3b. Variance of chest movement. Variance of chest motion showed significance decrease after longer acclimation. 4 mice; 52 trials; left, light on; right, light off; Str, very beginning training sessions(~1week); Las, last training sessions(>5weeks); mean±S.D, *p<0.05.

Video.1-3

Video 1

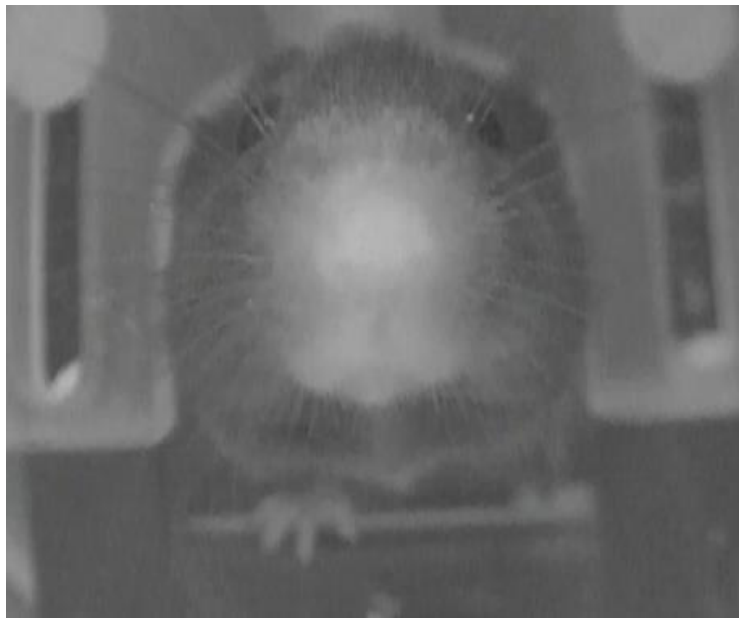

Video 2

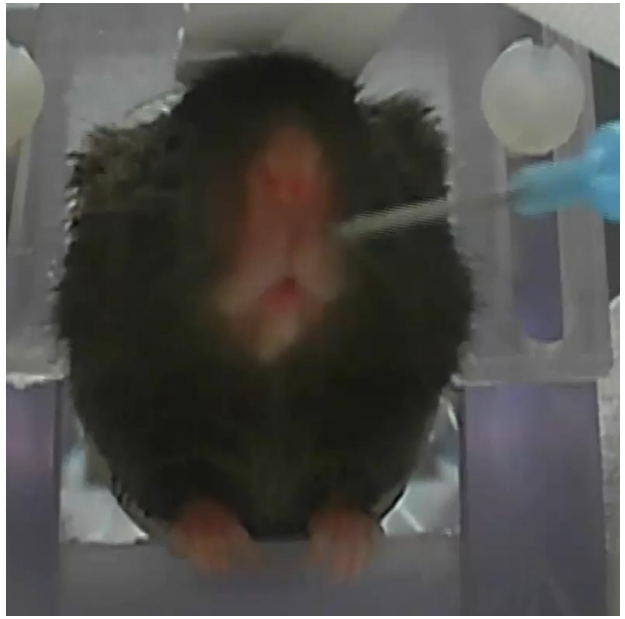

Video 3

Video.4-6

Pupil dynamic in Task Vs. Resting-state

Light ON

Light OFF

Video 4

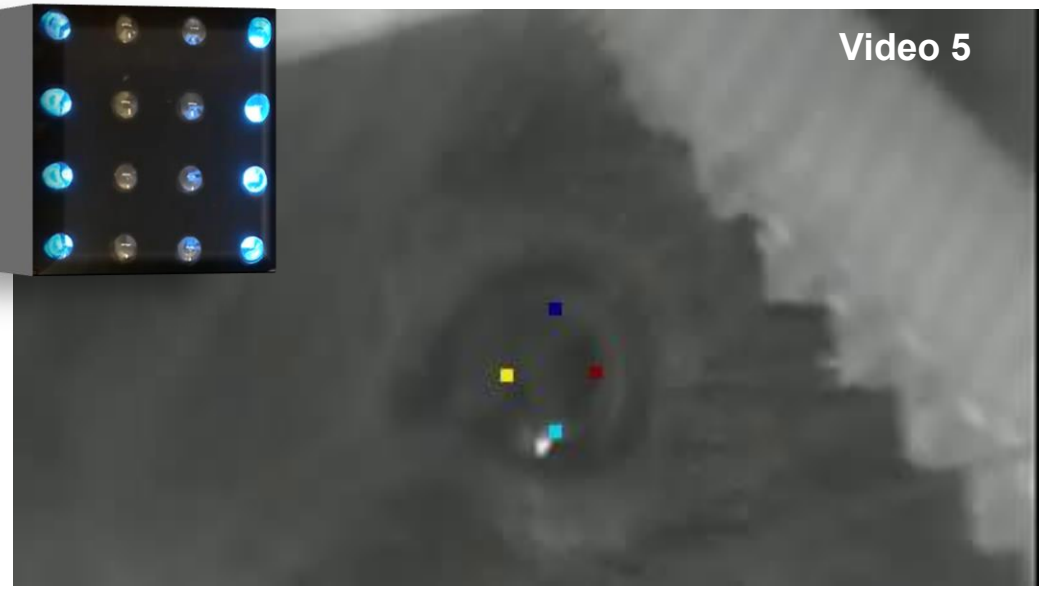

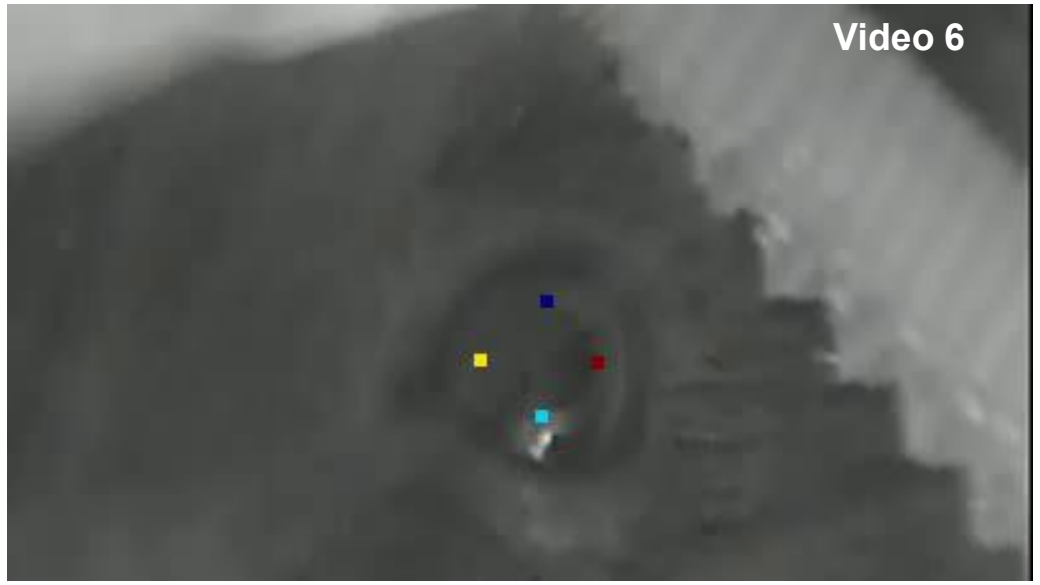

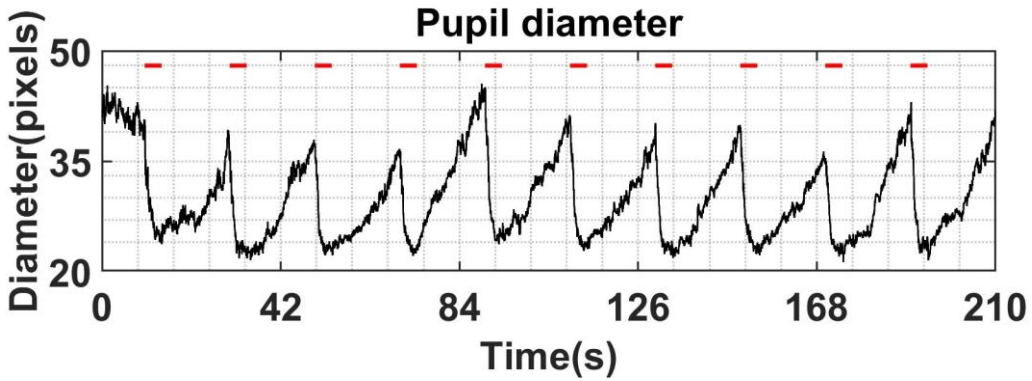

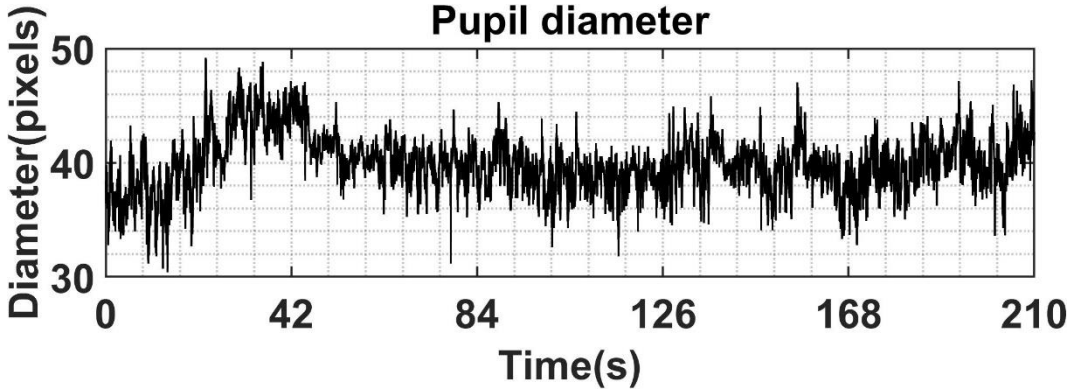

Video.7-10

Outside scanner

Video 7

Video 8

Inside scanner

Video 9

Video 10

Video.11-12

Pupil dynamics

Video 11

Video 12

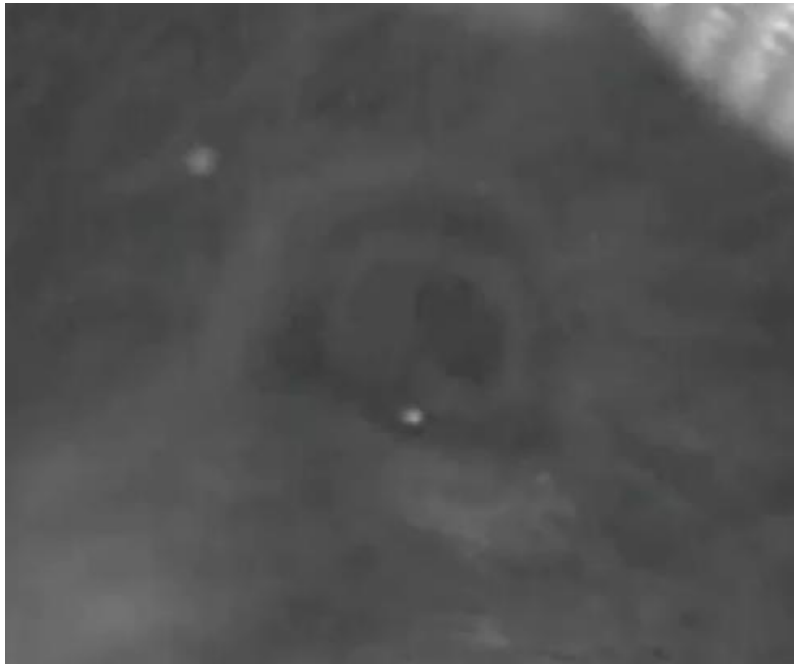

Video 1: Head-fixed mouse during acclimation inside the scanner with noise.

Video 2: Water rewards while being restrained in the system.

Video 3: Two weeks after headpost surgery.

Video 4: Blue LED light matrix for visual stimulations.

Video 5: DeepLab cut for labeling and extracting the pupil size with light on.

Video 6: DeepLab cut for labeling and extracting the pupil size with light off.

The left lower panel figure is an example of pupil dynamics extracted from the labeled videos under visual stimulation(left) and resting-state pupil dynamics(right). Red bar, duration of light on(4s-on-16s-off).

Video 7: Freely moving trained mouse (~3weeks) showing less inclination to the ‘imaging posture’ in the training box.

Video 8: Trained mouse (>5weeks) stays calm and keeps the right ‘imaging posture’ in the training box.

Video 9: Head-fixed mouse (~1weeks) inside the scanner with noise, showing obvious motions.

Video 10: Head-fixed mouse (>5weeks) inside the scanner with noise, showing less movement and staying quiet.

Video 11: Head-fixed mouse (~1 week training) inside the scanner with noise, showing fast pupil changes.

Video 12: Head-fixed mouse (>5 weeks training) inside the scanner with noise, showing slow and normal pupil changes.

8.2 Supplementary table

Table.S1. Summary of non-human(primates) awake fMRI since year 2000

Ref.	Scanner	Species	Anesthetics	Training	Setups	Ear/Bite bar	Stress monitor	Motion detection	Stimulus
(Dinh et al., 2021)	9.4T Scanner, FLASH Image: 0.059×0.059×0.5mm EPI image: 0.156×0.1456×0.5mm	C57BL/6 mice, 13 male	1% isoflurane before training and imaging	10days, 30min up to 120min, 15min/day increment, for remaining 3days, four mice trained in mock scanner, 3 mice trained in real scanner	Headpost, Body/neck restrain, nose cone	Unknown	Unknown	Respiration Temperature Chest movement were monitored frame-wise displacements(FD) for motion evaluation	Visual stim
(Tsurugizawa et al., 2020)	4.7T Scanner, Anat. Image: 0.125×0.125×1.0mm EPI Image: 0.2×0.2×1.0mm	15q dup mice, 25 mice were used for fMRI(including 10 wide type for control)	2% isoflurane before training and imaging	4days, 2 days outside scanner, 2 days inside scanner. 30min at 1st and 60min at 2nd.	Headpost nose mask ear bar	Ear bar	corticosterone	Heart rate respiration rate Six motion parameters (three translation and three rotation)	olfaction stim
(Chen et al., 2020)	9.4T Scanner, RARE Image: 0.0625×0.0625×0.4mm EPI Image: 0.15×0.15×0.4mm 0.1×0.1×0.3mm 0.2×0.2×0.3/0.4mm	C57BL/6 mice 40 male	Unknown	7days, day1-day4 head fixed with noise, Day5-day7 with sensory stimulus	Head holder Kwil-cast Earphone tube	Ear is fill with the silicone	Unknown	respiratory ate	Whisker auditory olfactory
(Behroozi et al., 2020)	7.0T Scanner, RARE Image: 0.23×0.23×0.25mm	Pigeons Twenty adult Columba livia	Unknown	3weeks, 10min up to 100 min. Water deprivation for the whole night before the imaging	plastic pedestal, head screws, piezo-electric pressure sensors measuring the dynamic pressure of jaw movements	Unknown	Corticosterone (ACTH stimulation test)	Respiration rate heart rate	color discrimination for Go/no Go task
(Desjardins et al., 2019)	7.0T Scanner, RARE Image: 0.078×0.039×1.0mm EPI Image: 0.2×0.2×1.0mm	C57BL/6J, JAX014548, JAX 005628, JAX 024109, 16 mice	Anesthetize(<60s) for head fixation	2 hours/day	Headpost	Ear plugs	Unknown	Camera surveillance	Whisker optogenetic
(Han et al., 2019)	9.4T Scanner, RARE Image: 0.0625×0.0625×0.4mm EPI Image: 0.15×0.15×0.4mm	C57BL/6J mice 8 male	Unknown	water restriction habituation, automatic lick teaching, automatic shaping, GNG task training	Head holder Kwil-cast	The drum membrane of the middle ear was punctured quickly, and the Kwik-cast was then injected	Unknown	Unknown	olfaction stim for Go/noGO licking
(Matsubayashi et al., 2018)	7.0T Scanner; RARE Image: 0.075×0.075×0.3mm, EPI Image: 0.2×0.2×0.5mm	C57BL/6J mice 9 female	Unknown	5 weeks,2 hours/day, mice underwent laminectomy at the	Head bar Body restrain	Unknown	Unknown	respiration rate	Unknown

				level of the Th9/10 vertebra					
(Takata et al., 2018)	7.0 T Scanner, RARE Image: 0.075×0.075×0.3mm, EPI Image: 0.2×0.2×0.5mm.	Double transgenic mice 22 male 29 female	Unknown	7 days, 2 hours/day	optical fiber head-holder	Unknown	Unknown	Unknown	Optogenetics in the left visual cortex
(Stenroos et al., 2018)	7.0 T Scanner, Anat. Image: 0.097×0.097×0.75mm, EPI Image: 0.39×0.39×1.5mm.	rat 8 male	1.5-2% isoflurane before training and imaging	10 days, 15min up to 45min, forepaws were attached with masking tape, hind paws were tied together with the tail with tape	Body restrain with cloth	bite bar shoulder support pad cheek support nose cone	corticosterone	heart rate respiration	None
(Paasonen et al., 2018)	7.0 T Scanner, Anat. Image: 0.097×0.097×0.75mm, EPI Image: 0.39×0.39×1.5mm.	rat 8 male	1.5-2% isoflurane before imaging	10 days, 15min up to 45min, forepaws were secured and hindpaw with tail were secured using masking tape. The body was wrapped with plastic foam sheet	Body restrain with cloth	bite bar shoulder support pad cheek support nose cone Silicone plugs were inserted into the ear	corticosterone	Unknown	None
(Matsubayashi et al., 2018)	7.0T Scanner, RARE Image: 0.075×0.075×0.3mm, EPI Image: 0.2×0.2×0.5mm.	C57BL/6J mice spinal cord injury 9 female	Unknown	1 week, 2hurs/day	head-bar	Unknown	Unknown	respiration	None
(Ma et al., 2018)	7.0T Scanner, Anat. Image: 0.125×0.125×1.0mm, EPI Image: 0.5×0.5×1.0mm.	rat 59 male	3% isoflurane before imaging	7 days	bite bar, ears secured by two adjustable ear pads, and nose secured by a nose bar, head restrainer	Bite bar Ear bar Nose bar	Unknown	translational movement	None
(Smith et al., 2017)	4.7 T Scanner, RARE Image: 0.125×0.125×1.0mm, EPI Image: 0.5×0.5×1.0mm.	Long Evan rats 42 male	2% isoflurane before training and imaging	7days	Headpost, Body restrain	Unknown	Unknown	Unknown	Nome
(Madularu et al., 2017)	7.0T Scanner, RARE Image: 0.3×0.3×1.2mm, Func. Image: 0.3×0.3×1.2mm.	C57BL/6 mice 33 male	2% isoflurane before training and imaging	5 days	No headpost, 3D printed restrain system.	Unknown	Respiration rate, Fecal boli	Volume displacement	olfactory stimulus
(Chang et al., 2017)	7.0 Scanner, Anat. Image: 0.38×0.38×0.5mm, EPI Image: 0.38×0.38×0.5mm.	rats 22 male	Unknown	2 weeks, 30mins/day	Head-Post	Unknown	no	respiratory rates	air-puff stimuli to the side surface of their hind paw
(Poirier et al., 2017)	4.7 scanner, RARE image:	adolescent spontaneously	1% isoflurane before training and imaging	8 days, 15mins up to 90min, 15 min/day increment	No headpost head restrainer body tube	Ear bar nose clamp	Unknown	Unknown	None

	0.125×0.125×1.0mm, EPI image: 0.5×0.5×1.0mm.	hypertensive rat(n=26), Wistar Kyoto(n=20) and Sprague–Dawley(n=12)							
(Van Ruijssevelt et al., 2017)	7.0T Scanner, EPI Image: 0.25×0.25×0.75mm, RARE Image: 0.07×0.07×0.07mm.	zebra finches 10 male	Unknown	25days, 10min up to120min	Head fixed, Body jacket, beak mask and fixation tape.	Unknown	Unknown	Respiration rate	Auditory Stimulus
(Berns et al., 2017)	3.0T Scanner, Anat. Image: 3.0×3.0×2.5mm, Func. Image: 3.0×3.0×2.5mm.	Dog 43 both male and female	Unknown	2 months, 10-15min/day, three days/week,	Unknown	Unknown	Unknown	Unknown	hand signals indicating
(Behroozi et al., 2017)	7.0T Scanner, EPI Image: 0.15×0.15×0.3mm, RARE Image: 0.47×0.47×1.0mm.	Pigeon 8 Valencian Figurita	Unknown	10days, 15min up to 60min	plastic pedestal	Unknown	Unknown	Respiration rate	no
(Yee et al., 2016)	7.0T Scanner, RARE Image: 0.097×0.097×0.7mm EPI Image: 0.26×0.26×0.7mm	prairie voles 14 male	Unknown	no training procedures, only restrain in the scanner	Body restrain and nose cone, bite bar, helmet	Bite bar	Unknown	Heart rate	CO2 (5%) odor
(Moore et al., 2016)	7.0T Scanner, RARE Image: 0.097×0.097×0.75mm, EPI Image: 0.26×0.26×0.75mm.	Male Oprm1+/+ and Oprm1−/− mice	2-3% isoflurane before training and imaging	4 consecutive days, 30min/day	head in a cushion, ear bars, pressure points used to immobilize the head	Ear bar	Unknown	Unknown	5% carbon dioxide
(Madularu et al., 2016)	7.0T Scanner, RARE Image: 0.11×0.11×0.75mm EPI Image: 0.3125×0.3125×0.75mm	OVX Sprague Dawley 36 rats	2-3% Isoflurane before training and imaging	5 consecutive days, 30mins/day	head in a cushion, pressure points used to immobilize the head, ear bars,	Ear bar	Unknown	Unknown	None
(Kenkel et al., 2016)	7.0T Scanner, RARE Image: 0.11×0.11×1.0mm, EPI Image: 0.3125×0.3125×1.0mm	Adult WT (12) and Fox (10) male Sprague Dawley rats	2-3% Isoflurane before training and imaging	4-5 consecutive days, 30mins/day	Head holder and body tube, no headpost, ear bars, body, paws were tighten in the scanner.	Ear bar	Unknown	Unknown	odor stimulus
(Chang et al., 2016)	7.0T Scanner, EPI Image: 0.38×0.38×0.5mm	Sprague-Dawley rats, 10 male	Unknown	8-10 days, (30min/day)	Headpost, body restrain	Unknown	corticosterone	Respiration rate	Air-puff to the forepaw
(Yoshida et al., 2016)	7.0T Scanner, EPI Image: 0.2×0.2×0.5mm	C57BL/6 mice, 8 male	Unknown	8 days, 2 hours/day	head bar EMG electrodes	Unknown	ECG EMG	Heart rate	None
(Aksenov et al., 2016)	9.4T Scanner, EPI Image: 0.375×0.375×1.0mm	Dutch-belted rabbit 6 female	Unknown	3-5day, restrained by means of a cloth sleeve	headbolts, electrodes and cannulae were implanted	Unknown	LFP MUA	Unknown	Optogenetic Whisker stimulus
(Madularu et al., 2015)	7.0T Scanner, RARE Image: 0.11×0.11×1.0mm EPI Image: 0.3125×0.3125×1.0mm	OVX Sprague Dawley rats 27 female	2-3% Isoflurane before training and imaging	5 consecutive days, 30mins/day	head in a cushion ear bars, pressure points used to immobilize the head	Ear bar	Unknown	Unknown	drug model
(Liang et al., 2015b)	7 T Scanner, RARE Image:	11 rats	2% Isoflurane	7 days , 15min up to 90min	four plastic MR compatible screws	Ear bar	Unknown	Unknown	Optogenetics

	0.125×0.125×1.0mm EPI Image: 0.5×0.5×1.0mm		before training and imaging		were fixed into the skull, optic fiber was embedded				
(Liang et al., 2015a)	4.7 T Scanner, RARE Image: 0.125×0.125×1.0mm EPI Image: 0.5×0.5×1.0mm	Long Evan (LE) rats 42 male	2% Isoflurane before training and imaging	7 days, 15min up to 90min	Plexiglas stereotaxic head holder, plastic ear bars, forepaw and hindpaw were loosely taped	Ear bar	Unknown	Unknown	None
(Harris et al., 2015)	7.0 T Scanner, RARE Image: 0.1×0.1×0.8mm EPI Image: 0.3×0.3×0.8mm	C57bl/6 mice 44 male	1–2% Isoflurane before training and imaging	5 days, 22min/day, 12-day protocol 6 min up to 22 min	No headpost, limbs were tapped, body were restrained in the body restrainer, nose cone, foam headband	Foam headband into the ear	respiration rate, heart rate, body movements e.g. leg kicks, arched back) body weight, Corticosterone	Respiration, Heart rate, Body weight, Body movements, Corticosterone,	cued fear conditioning Foot shock(0.5mA)
(Dilks et al., 2015)	3.0T Scanner, Anat. Image: 1.5×1.5×2.0mm, EPI Image: 3.0×3.0×3.0mm.	8 Dogs	None	2-3 months, presentation of images on a computer screen	Unknown	Unknown	Unknown	Unknown	Face processing
(Liang et al., 2014)	4.7 T Scanner, RARE Image: 0.125×0.125×1.0mm EPI Image: 0.5×0.5×1.0mm	Long-Evans (LE) adult rats 32 male	2% Isoflurane before training and imaging	7 days, 15min up to 90min	Plexiglas stereotaxic head holder plastic ear bars, forepaw and hindpaw were loosely taped	Ear bar Bit bar	anxiety level of rats was assessed by using the EPM test	EPM test	None
(Ferris et al., 2014)	7.0 T Scanner, RARE Image: 0.097×0.097×0.75mm, EPI Image: 0.26×0.26×0.75mm.	Wild-type mice (C57B/L6J) (n =5 male, 6 female) and knock in zQ175 HET (n =4 male, 6 female) and HOM (n =5 male, 5 female) mice	2-3% Isoflurane before training and imaging	4 consecutive days, 30min/day	Body tube, nose cone, hollow tube	Bite bar	Unknown	displacement	Odor stimulus
(Ma et al., 2013)	3.0 T Scanner, RARE Image: 0.5×1.0×0.5mm, EPI Image: 2.0×2.0×2.0mm.	4 cats	Unknown	Unknown	head-post, animal chair,	Unknown	Unknown	displacement	Visual stimulus
(Johnson et al., 2013)	7.0 T Scanner, Anat. Image: 0.11×0.11×1.0mm, Func. Image: 0.46×0.46×1.0mm.	Sprague–Dawley rats 9 male	Unknown	10 days cocaine + odor versus no cocaine + no odor training	Chamber, Electrode, intravenous catheters,	Unknown	Unknown	Unknown	cocaine-associated odor cue
(De Groof et al., 2013)	7.0 T Scanner, Anat. Image: 0.085×0.085×0.17mm, Func. Image: 0.34×0.34×1.0mm.	Pigeons 4 adult	None	three distinct procedures: a)10-30-60min for 3days, b)head fixed 10-20-40min,c) with sounds for 1 week	Cloth jacket, head pedestal; plastic tube;	Unknown	Unknown	displacement	visual stimuli
(Berns et al., 2013)	3.0 T Scanner, Anat. Image: 1.5×1.5×2.0mm, Func. Image: 3.0×3.0×3.0mm.	15 dogs	None	2-3months	chin rest, neck coil	Unknown	Unknown	Unknown	Hand signals

(Tsurugizawa et al., 2012)	4.7 T Scanner, Anat. Image: 0.54×0.54×1.3mm, Func. Image: 0.27×0.27×1.3mm.	Wistar rats 12 male	2% isoflurane	3 days, 30-90min	Body restraint, head positioner elastic bands	earplugs	Heart rate respiration rate	Unknown	light stimulation
(Desai et al., 2011)	9.4 T Scanner, Anat. Image: 0.78×0.78×0.5mm, Func. Image: 0.1×0.1×0.5mm, 0.2×0.2×0.5mm.	11 wild-type, 11 transgenic ChR2 mice	0.7% isoflurane for awake imaging	3 days, 20-40mins	Headpost, body restraint tube	Unknown	respiration rate	respiration displacement	optogenetics
(Liang et al., 2011)	4.7 T Scanner, Anat. Image: 0.125×0.125×1.0mm, Func. Image: 0.5×0.5×1.0mm.	Long–Evans rat 16 adult male	isoflurane	8days, 15-90mins	head holder using plastic ear-bars	Ear bar Bite bar	Unknown	Unknown	None
(Zhang et al., 2010)	4.7T Scanner, RARE Image: 0.125×0.125×1.0mm, EPI Image: 0.5×0.5×1.0mm.	Long-Evans (LE) rat 8 adult male	2% Isoflurane before training and imaging	8day, 15min up to 90min	Plexiglas stereotaxic head holder plastic ear bars, forepaw and hindpaw were loosely taped	Ear bar	Unknown	Unknown	None
(Chen et al., 2009)	4.7T Scanner, RARE Image: 0.117×0.117×1.0mm, EPI Image: 0.468×0.468×1.0mm.	8 female rats	2% Isoflurane	3day	Restrainer, headpiece, ear bar, head holder, bite bar, body tube	Ear bar Bite bar	None	None	water (no odor), lemon scent, and TMT odor
(Febo et al., 2008)	4.7T Scanner, RARE Image: 0.117×0.117×1.2mm, EPI Image: 0.468×0.468×1.2mm.	Virgin Sprague-Dawley rats	2-3% isoflurane	4day, 90min/session	Headpiece, head holder, Bite bar, ear bar,	Ear bar Bite bar	None	None	Pup Suckling
(Ferris et al., 2008)	4.7T Scanner, RARE Image: 0.117×0.117×1.2mm, EPI Image: 0.468×0.468×1.2mm.	Adult male and female Long-Evans rats	2–3% isoflurane	4day, 60min/session	Headpiece, head holder, Bite bar, ear bar,	Ear bar	None	displacement	Drug (SRX251 or fluoxetine)
(Duong, 2007)	4.7T Scanner, RARE Image: 0.156×0.156×1.5mm, EPI Image: 0.3125×0.3125×1.5mm.	7 Sprague–Daley rats	2% isoflurane	Unknown	restrained with ear-, nose-, tooth-, and shoulder-bars, and a body restraining tub	restrainer with ear-, nose-, tooth-, and shoulder-bars, and a body restraining tub	Respiration rate Heart rate blood pressure	Respiration rate Heart rate blood pressure	Hypoxia
(Chin et al., 2006)	4.7T Scanner, Anat. Image: 0.156×0.156×1.25mm, Func. Image: 0.156×0.156×1.25mm.	Adult male Sprague-Dawley rats	~3% isoflurane	4day, 7min up to 60min	Training holder, body tube and headpiece	Unknown	None	None	pharmacological (apomorphine and ABT-594)
(King et al., 2005)	4.7T Scanner, RARE Image: 0.1×0.1×1.5mm, EPI Image: 0.2×0.2×1.5mm.	Sprague–Dawley rats 8 male	ketamine and medetomidine being secured	8 consecutive days, 90min/session	headpiece with blunted ear, bite bar, body tube	headpiece with blunted ear, bite bar, body tube	respiratory rate and heart rate corticosterone	corticosterone	None
(Febo et al., 2004)	4.7T Scanner, Anat. Image: 0.117×0.117×1.2mm, EPI Image: 0.468×0.468×1.2mm.	Male Sprague-Dawley rats	2% isoflurane	3-4 days, 90mins/session	cylindrical head holder, body holder,headpiece, bite bar, ear bar	headpiece, bite bar, ear bar	None	None	cocaine

(Sachdev et al., 2003)	4.7T Scanner, Anat. Image: 0.23×0.23×1.2mm, EPI Image: 0.47×0.47×1.2mm.	Long Evans rats 3 male and 2female	Diazepam injection	Body trainer every day for 1 week. after headpost surgery, re-trained for 1 week	felt sleeve, wrapped in a cotton cloth, inserted to the neck into a Plexiglas tube; Velcro straps	three thread-bearing nylon posts; lightweight masking tape; plastic pipe	Unknown	displacement	Whisker stimulus
(Kenneth Sicard, 2003)	4.7T Scanner, Anat. Image: 0.097×0.097×1.5mm, EPI Image: 0.039×0.039×1.5mm.	Sprague Dawley rats 15	2% isoflurane	None	Secured in a rat restrainer with ear-, nose-, tooth-, and shoulder-bars, a body-restraint tube	Ear bar	blood pressure, heart rate, respiration rate		Hypercapnic (CO_2) challenges
(Peeters et al., 2001)	7.0T Scanner, Anat. Image: 0.078×0.156×1.0mm, EPI Image: 0.156×0.312×1.0mm.	6 Wistar rats	5% fluothane, Atropine injection, Mivacurium or α-chloralose	None	plexi stereotactic head holder, incisor bar and earplugs	earplugs	None	EEG recording	Electrical forepaw stimulation
(Wyrwicz et al., 2000)	4.7T Scanner, Anat. Image: 0.156×0.156×2.0mm, EPI Image: 0.935×0.935×2.0mm.	rabbits (New Zealand white (NZW) or Dutch Belted (DB)) 5 female	Unknown	30min/sessions 1 or 2 sessions	Tied at the neck and tail in soft cloth bag and fastened to an acrylic cradle with velcro straps with four restraining headbolts.	None	None	None	Visual stimulation

References to Table.S1.

Aksenov, D.P., Li, L., Miller, M.J., Wyrwicz, A.M., 2016. Blood oxygenation level dependent signal and neuronal adaptation to optogenetic and sensory stimulation in somatosensory cortex in awake animals. Eur J Neurosci 44, 2722-2729.

Behroozi, M., Helluy, X., Strockens, F., Gao, M., Pusch, R., Tabrik, S., Tegenthoff, M., Otto, T., Axmacher, N., Kumsta, R., Moser, D., Genc, E., Gunturkun, O., 2020. Event-related functional MRI of awake behaving pigeons at 7T. Nat Commun 11, 4715.

Behroozi, M., Strockens, F., Helluy, X., Stacho, M., Gunturkun, O., 2017. Functional Connectivity Pattern of the Internal Hippocampal Network in Awake Pigeons: A Resting-State fMRI Study. Brain Behav Evol 90, 62-72.

Berns, G.S., Brooks, A., Spivak, M., 2013. Replicability and heterogeneity of awake unrestrained canine FMRI responses. PLoS One 8, e81698.

Berns, G.S., Brooks, A.M., Spivak, M., Levy, K., 2017. Functional MRI in Awake Dogs Predicts Suitability for Assistance Work. Sci Rep 7, 43704.

Chang, P.C., Centeno, M.V., Procissi, D., Baria, A., Apkarian, A.V., 2017. Brain activity for tactile allodynia: a longitudinal awake rat functional magnetic resonance imaging study tracking emergence of neuropathic pain. Pain 158, 488-497.

Chang, P.C., Procissi, D., Bao, Q., Centeno, M.V., Baria, A., Apkarian, A.V., 2016. Novel method for functional brain imaging in awake minimally restrained rats. J Neurophysiol 116, 61-80.

Chen, W., Shields, J., Huang, W., King, J.A., 2009. Female fear: influence of estrus cycle on behavioral response and neuronal activation. Behav Brain Res 201, 8-13.

Chen, X., Tong, C., Han, Z., Zhang, K., Bo, B., Feng, Y., Liang, Z., 2020. Sensory evoked fMRI paradigms in awake mice. Neuroimage 204, 116242.

Chin, C.L., Fox, G.B., Hradil, V.P., Osinski, M.A., McGaraughty, S.P., Skoubis, P.D., Cox, B.F., Luo, Y., 2006. Pharmacological MRI in awake rats reveals neural activity in area postrema and nucleus tractus solitarius: relevance as a potential biomarker for detecting drug-induced emesis. Neuroimage 33, 1152-1160.

De Groof, G., Jonckers, E., Gunturkun, O., Denolf, P., Van Auderkerke, J., Van der Linden, A., 2013. Functional MRI and functional connectivity of the visual system of awake pigeons. Behav Brain Res 239, 43-50.

Desai, M., Kahn, I., Knoblich, U., Bernstein, J., Atallah, H., Yang, A., Kopell, N., Buckner, R.L., Graybiel, A.M., Moore, C.I., Boyden, E.S., 2011. Mapping brain networks in awake mice using combined optical neural control and fMRI. J Neurophysiol 105, 1393-1405.

Desjardins, M., Kilic, K., Thunemann, M., Mateo, C., Holland, D., Ferri, C.G.L., Cremonesi, J.A., Li, B., Cheng, Q., Weldy, K.L., Saisan, P.A., Kleinfeld, D., Komiyama, T., Liu, T.T., Bussell, R., Wong, E.C., Scadeng, M., Dunn, A.K., Boas, D.A., Sakadzic, S., Mandeville, J.B., Buxton, R.B., Dale, A.M., Devor, A., 2019. Awake Mouse Imaging: From Two-Photon Microscopy to Blood Oxygen Level-Dependent Functional Magnetic Resonance Imaging. Biol Psychiatry Cogn Neurosci Neuroimaging 4, 533-542.

Dilks, D.D., Cook, P., Weiller, S.K., Berns, H.P., Spivak, M., Berns, G.S., 2015. Awake fMRI reveals a specialized region in dog temporal cortex for face processing. PeerJ 3, e1115.

Dinh, T.N.A., Jung, W.B., Shim, H.J., Kim, S.G., 2021. Characteristics of fMRI responses to visual stimulation in anesthetized vs. awake mice. Neuroimage 226, 117542.

Duong, T.Q., 2007. Cerebral blood flow and BOLD fMRI responses to hypoxia in awake and anesthetized rats. Brain Res 1135, 186-194.

Febo, M., Segarra, A.C., Tenney, J.R., Brevard, M.E., Duong, T.Q., Ferris, C.F., 2004. Imaging cocaine-induced changes in the mesocorticolimbic dopaminergic system of conscious rats. Journal of Neuroscience Methods 139, 167-176.

Febo, M., Stolberg, T.L., Numan, M., Bridges, R.S., Kulkarni, P., Ferris, C.F., 2008. Nursing stimulation is more than tactile sensation: It is a multisensory experience. Horm Behav 54, 330-339.

Ferris, C.F., Kulkarni, P., Toddes, S., Yee, J., Kenkel, W., Nedelman, M., 2014. Studies on the Q175 Knock-in Model of Huntington's Disease Using Functional Imaging in Awake Mice: Evidence of Olfactory Dysfunction. Front Neurol 5, 94.

Ferris, C.F., Stolberg, T., Kulkarni, P., Murugavel, M., Blanchard, R., Blanchard, D.C., Febo, M., Brevard, M., Simon, N.G., 2008. Imaging the neural circuitry and chemical control of aggressive motivation. BMC Neurosci 9, 111.

Han, Z., Chen, W., Chen, X., Zhang, K., Tong, C., Zhang, X., Li, C.T., Liang, Z., 2019. Awake and behaving mouse fMRI during Go/No-Go task. Neuroimage 188, 733-742.

Harris, A.P., Lennen, R.J., Marshall, I., Jansen, M.A., Pernet, C.R., Brydges, N.M., Duguid, I.C., Holmes, M.C., 2015. Imaging learned fear circuitry in awake mice using fMRI. Eur J Neurosci 42, 2125-2134.

Johnson, T.R., Smerkers, B., Moulder, J.K., Stellar, J.R., Febo, M., 2013. Neural processing of a cocaine-associated odor cue revealed by functional MRI in awake rats. Neurosci Lett 534, 160-165.

Kenkel, W.M., Yee, J.R., Moore, K., Madularu, D., Kulkarni, P., Gamber, K., Nedelman, M., Ferris, C.F., 2016. Functional magnetic resonance imaging in awake transgenic fragile X rats: evidence of dysregulation in reward processing in the mesolimbic/habenular neural circuit. Transl Psychiatry 6, e763.

Kenneth Sicard, Q.S., Mathew E. Brevard, Ross Sullivan, Craig F. Ferris, Jean A. King, and Timothy Q. Duong, 2003. Regional Cerebral Blood Flow and BOLD Responses in Conscious and Anesthetized Rats Under Basal and Hypercapnic Conditions: Implications for Functional MRI Studies.

King, J.A., Garelick, T.S., Brevard, M.E., Chen, W., Messenger, T.L., Duong, T.Q., Ferris, C.F., 2005. Procedure for minimizing stress for fMRI studies in conscious rats. J Neurosci Methods 148, 154-160.

Liang, Z., King, J., Zhang, N., 2011. Uncovering intrinsic connectional architecture of functional networks in awake rat brain. J Neurosci 31, 3776-3783.

Liang, Z., King, J., Zhang, N., 2014. Neuroplasticity to a single-episode traumatic stress revealed by resting-state fMRI in awake rats. Neuroimage 103, 485-491.

Liang, Z., Liu, X., Zhang, N., 2015a. Dynamic resting state functional connectivity in awake and anesthetized rodents. Neuroimage 104, 89-99.

Liang, Z., Watson, G.D., Alloway, K.D., Lee, G., Neuberger, T., Zhang, N., 2015b. Mapping the functional network of medial prefrontal cortex by combining optogenetics and fMRI in awake rats. Neuroimage 117, 114-123.

Ma, M., Qian, C., Li, Y., Zuo, Z., Liu, Z., 2013. Setup and data analysis for functional magnetic resonance imaging of awake cat visual cortex. Neurosci Bull 29, 588-602.

Ma, Z., Ma, Y., Zhang, N., 2018. Development of brain-wide connectivity architecture in awake rats. Neuroimage 176, 380-389.

Madularu, D., Kulkarni, P., Yee, J.R., Kenkel, W.M., Shams, W.M., Ferris, C.F., Brake, W.G., 2016. High estrogen and chronic haloperidol lead to greater amphetamine-induced BOLD activation in awake, amphetamine-sensitized female rats. Horm Behav 82, 56-63.

Madularu, D., Mathieu, A.P., Kumaragamage, C., Reynolds, L.M., Near, J., Flores, C., Rajah, M.N., 2017. A non-invasive restraining system for awake mouse imaging. J Neurosci Methods 287, 53-57.

Madularu, D., Yee, J.R., Kenkel, W.M., Moore, K.A., Kulkarni, P., Shams, W.M., Ferris, C.F., Brake, W.G., 2015. Integration of neural networks activated by amphetamine in females with different estrogen levels: a functional imaging study in awake rats. Psychoneuroendocrinology 56, 200-212.

Matsubayashi, K., Nagoshi, N., Komaki, Y., Kojima, K., Shinozaki, M., Tsuji, O., Iwanami, A., Ishihara, R., Takata, N., Matsumoto, M., Mimura, M., Okano, H., Nakamura, M., 2018. Assessing cortical plasticity after spinal cord injury by using resting-state functional magnetic resonance imaging in awake adult mice. Sci Rep 8, 14406.

Moore, K., Madularu, D., Iriah, S., Yee, J.R., Kulkarni, P., Darcq, E., Kieffer, B.L., Ferris, C.F., 2016. BOLD Imaging in Awake Wild-Type and Mu-Opioid Receptor Knock-Out Mice Reveals On-Target Activation Maps in Response to Oxycodone. Front Neurosci 10, 471.

Paasonen, J., Stenroos, P., Salo, R.A., Kiviniemi, V., Grohn, O., 2018. Functional connectivity under six anesthesia protocols and the awake condition in rat brain. Neuroimage 172, 9-20.

Peeters, R.R., Tindemans, I., De Schutter, E., Van der Linden, A., 2001. Comparing BOLD fMRI signal changes in the awake and anesthetized rat during electrical forepaw stimulation. Magn Reson Imaging 19, 821-826.

Poirier, G.L., Huang, W., Tam, K., DiFranza, J.R., King, J.A., 2017. Awake whole-brain functional connectivity alterations in the adolescent spontaneously hypertensive rat feature visual streams and striatal networks. Brain Struct Funct 222, 1673-1683.

Sachdev, R.N., Champney, G.C., Lee, H., Price, R.R., Pickens, D.R., 3rd, Morgan, V.L., Stefansic, J.D., Melzer, P., Ebner, F.F., 2003. Experimental model for functional magnetic resonance imaging of somatic sensory cortex in the unanesthetized rat. Neuroimage 19, 742-750.

Smith, J.B., Liang, Z., Watson, G.D.R., Alloway, K.D., Zhang, N., 2017. Interhemispheric resting-state functional connectivity of the claustrum in the awake and anesthetized states. Brain Struct Funct 222, 2041-2058.

Stenroos, P., Paasonen, J., Salo, R.A., Jokivarsi, K., Shatillo, A., Tanila, H., Grohn, O., 2018. Awake Rat Brain Functional Magnetic Resonance Imaging Using Standard Radio Frequency Coils and a 3D Printed Restraint Kit. Front Neurosci 12, 548.

Takata, N., Sugiura, Y., Yoshida, K., Koizumi, M., Hiroshi, N., Honda, K., Yano, R., Komaki, Y., Matsui, K., Suematsu, M., Mimura, M., Okano, H., Tanaka, K.F., 2018. Optogenetic astrocyte activation evokes BOLD fMRI response with oxygen consumption without neuronal activity modulation. Glia 66, 2013-2023.

Tsurugizawa, T., Tamada, K., Ono, N., Karakawa, S., Kodama, Y., Debacker, C., Hata, J., Okano, H., Kitamura, A., Zalesky, A., Takumi, T., 2020. Awake functional MRI detects neural circuit dysfunction in a mouse model of autism. Sci Adv 6, eaav4520.

Tsurugizawa, T., Uematsu, A., Uneyama, H., Torii, K., 2012. Functional brain mapping of conscious rats during reward anticipation. J Neurosci Methods 206, 132-137.

Van Ruijssevelt, L., Hamaide, J., Van Gurp, M.T., Verhoye, M., Van der Linden, A., 2017. Auditory evoked BOLD responses in awake compared to lightly anaesthetized zebra finches. Sci Rep 7, 13563.

Wyrwicz, A.M., Chen, N., Li, L., Weiss, C., Disterhoft, J.F., 2000. fMRI of visual system activation in the conscious rabbit. Magn Reson Med 44, 474-478.

Yee, J.R., Kenkel, W.M., Kulkarni, P., Moore, K., Perkeybile, A.M., Toddes, S., Amacker, J.A., Carter, C.S., Ferris, C.F., 2016. BOLD fMRI in awake prairie voles: A platform for translational social and affective neuroscience. Neuroimage 138, 221-232.

Yoshida, K., Mimura, Y., Ishihara, R., Nishida, H., Komaki, Y., Minakuchi, T., Tsurugizawa, T., Mimura, M., Okano, H., Tanaka, K.F., Takata, N., 2016. Physiological effects of a habituation procedure for functional MRI in awake mice using a cryogenic radiofrequency probe. J Neurosci Methods 274, 38-48.

Zhang, N., Rane, P., Huang, W., Liang, Z., Kennedy, D., Frazier, J.A., King, J., 2010. Mapping resting-state brain networks in conscious animals. J Neurosci Methods 189, 186-196.